

Salt crystallization in porous materials: an NMR study

PROEFSCHRIFT

ter verkrijging van de graad van doctor aan de
Technische Universiteit Eindhoven, op gezag van de
Rector Magnificus, prof.dr. R.A. van Santen, voor een
commissie aangewezen door het College voor
Promoties in het openbaar te verdedigen
op donderdag 18 november 2004 om 16.00 uur

door

Lourens Albert Rijniers

geboren te Hengelo

Dit proefschrift is goedgekeurd door de promotoren:

prof.dr.ir. K. Kopinga
en
prof.dr. A. Putnis

Copromotor:
dr.ir. L. Pel

CIP-DATA LIBRARY TECHNISCHE UNIVERSITEIT EINDHOVEN

Rijniers, Lourens Albert

Salt crystallization in porous materials: an NMR study / by Lourens Albert Rijniers. -

Eindhoven : Technische Universiteit Eindhoven, 2004. -

Proefschrift. ISBN 90-386-1995-2

NUR 926

Trefwoorden: kernspinresonantie / poreuze materialen / bouwmaterialen / zoutverwering / kristallisatie / sorptie

Subject headings: nuclear magnetic resonance / porous materials / building materials / weathering / crystallization / supersaturation / sorption

Printed by: Universiteitsdrukkerij Technische Universiteit Eindhoven

Cover: Various photo's of salt crystallization in building material, rock formations, and laboratory conditions. Photo's by Rob van Hees, Andrew Putnis and Lourens Rijniers. Cover design by JWL Producties (www.jwlproducties.nl)

The work described in this thesis has been carried out in the group Transport in Permeable Media at the Eindhoven University of Technology, Department of Applied Physics. This work is supported by the Dutch Technology Foundation (STW), the Dutch materials research program (PPM) and the knowledge center for building and systems TNO-TUE.

I observed that salt exuded from the soil to such an extent as even to injure the pyramids.

- Herodotus, (484 B.C.425 B.C.), History, bk. 2

*Aan G.A.C. Bosch
&
J. Bosch-Quik*

Summary

Crystallization of salt is widely recognized as a cause of deterioration of porous building materials. However, the actual damage mechanism is unclear. One of the proposed mechanisms for salt weathering is crystallization pressure. This pressure is generated by the surface tension of the salt crystals in the pores.

A signature of this excess pressure is the enhanced solubility of a crystal inside a pore (often called supersaturation). Using a thermodynamic approach, the relation between the equilibrium supersaturation ratio and the crystallization pressure for a crystal inside a porous material is derived. In this derivation both the degree of hydration of the salt and the curvature of the liquid-vapor interface are taken into account.

By quantitative Nuclear Magnetic Resonance (NMR) measurement of the amount of both the Na and H ions in the solution inside a material, the salt concentration in that solution can be determined. An important feature of NMR is that it does not disturb the system in any way. The NMR relaxation of hydrogen nuclei of a fluid in a porous material is generally interpreted in terms of the Brownstein and Tarr model, in which the relaxation rate of the signal is inversely proportional to the pore size. We have investigated whether this model can be applied to the relaxation of Na nuclei in a NaCl solution in a porous material. The results indicate that the ion distribution over the pores can be obtained from an analysis of the Na NMR signal decay, if the pore sizes are roughly below 1 μm . When performing Na NMR, care has to be taken that the ions in the solution are in the fast modulation regime. If this is not the case, loss of Na signal may occur and a calibration is needed for quantitative measurements.

Experiments were performed on model porous materials, having a single pore size. Because of their high temperature dependent solubility Na_2CO_3 and Na_2SO_4 were used. A supersaturated state can be created easily by changing the temperature. To control the temperature of the sample, a sample holder was designed featuring a spiral through which a coolant flows. Care was taken that the sample holder and the coolant do not disturb the quantitative NMR measurements. The salt solution was saturated at 40 $^\circ\text{C}$, put into the pores of the material, and cooled to 2 $^\circ\text{C}$. Once nucleation has taken place the temperature was increased while performing NMR concentration measurements. For bulk Na_2CO_3 the solubility curve from literature was reproduced, whereas for Na_2CO_3 solution in pores of 7 and 10 nm a significant increase in the solubility was found. This results in an estimate for the surface tension of $\text{Na}_2\text{CO}_3 \cdot 10\text{H}_2\text{O}$ crystals of $\sigma = (0.09 \pm 0.02) \text{ N/m}$. For Na_2SO_4

the solubility both for bulk and inside pores matches the solubility of $\text{Na}_2\text{SO}_4 \cdot 7\text{H}_2\text{O}$, and no pore size dependence is observed. Hence no significant crystallization pressure exists for $\text{Na}_2\text{SO}_4 \cdot 7\text{H}_2\text{O}$. This $\text{Na}_2\text{SO}_4 \cdot 7\text{H}_2\text{O}$ crystal phase is known to be a meta-stable phase. In one experiment we managed to create a $\text{Na}_2\text{SO}_4 \cdot 10\text{H}_2\text{O}$ crystal inside pores of 7 nm. This measurement shows an increase in the solubility and the estimated surface tension is $\sigma = (0.10 \pm 0.04)$ N/m. Based on these estimates the maximum pore radius in which the salt can cause damage can be determined, being 12 and 20 nm for $\text{Na}_2\text{CO}_3 \cdot 10\text{H}_2\text{O}$ and $\text{Na}_2\text{SO}_4 \cdot 10\text{H}_2\text{O}$, respectively.

Besides these model porous materials, experiments were done on building materials. These measurements revealed the presence of $\text{Na}_2\text{SO}_4 \cdot 7\text{H}_2\text{O}$ in Savoniere stone, calcium silicate brick, and fired clay brick. In these materials the salt does not have a preferred pore size to crystallize in. In mortar $\text{Na}_2\text{SO}_4 \cdot 10\text{H}_2\text{O}$ was found, and the salt crystallizes in the largest pores, and hence with the lowest crystallization pressure.

In order to obtain more information on the crystallization inside porous materials also sorption measurements were performed. Compared to NMR the sorption measurement is somewhat indirect. Observation of supersaturation with the latter technique is possible for small pores (order 7 nm), but for large pores it is rather insensitive. The experiments show an increased solubility is found for NaCl ($\sigma = (0.08 \pm 0.02)$ N/m) and thenardite (anhydrous Na_2SO_4 , $\sigma = (0.24 \pm 0.05)$ N/m). This corresponds to a maximum pore size in which damage can be induced of 5 nm and 100 nm for NaCl and thenardite, respectively.

Samenvatting

Kristallisatie van zout wordt algemeen erkend als een oorzaak van achteruitgang van poreuze bouwmaterialen. Maar het exacte mechanisme waardoor de schade ontstaat is onduidelijk. Een van de voorgestelde mechanismen is kristallisatiedruk. Die druk komt tot stand door de oppervlaktespanning van de zoutkristallen in de poriën.

Een kenmerk van deze overdruk is de toegenomen oplosbaarheid van een zoutkristal in een porie (dit noemt men vaak superversadiging). Via een thermodynamische aanpak is de relatie tussen de evenwichts superversadigings verhouding en de kristallisatiedruk voor een kristal in een poreus materiaal afgeleid. In deze afleiding zijn zowel de hydratatioestand als de kromming van het oplossing-damp grensvlak meegenomen.

Door middel van kwantitatieve kernspinresonantie (NMR) metingen van de hoeveelheid Na en H ionen in de oplossing in een materiaal, kan de zout concentratie in die oplossing worden bepaald. Een belangrijke eigenschap van NMR is dat het systeem dat bestudeerd niet beïnvloed wordt. De NMR relaxatie van waterstofkernen in een vloeistof in een materiaal wordt algemeen geïnterpreteerd aan de hand van het Brownstein en Tarr model, waarin de relaxatiesnelheid van het signaal omgekeerd evenredig is met de poriegrootte. We hebben onderzocht of dit model ook kan worden toegepast op de relaxatie van Na ionen in een NaCl oplossing in een poreus materiaal. De resultaten geven aan dat de ionenverdeling over die poriën kan worden verkregen uit een analyse van het Na NMR signaal verval, mits de poriegroottes grofweg kleiner zijn dan $1\ \mu\text{m}$. Wanneer men Na NMR doet, moet men erop attent zijn dat de ionen in de oplossing in het fast modulation regime zitten. Als dat niet zo is, kan er Na signaal verlies optreden en is een calibratie nodig voor kwantitatieve metingen.

Er zijn experimenten gedaan aan model poreuze materialen, die een poriegrootte hebben. Vanwege de sterke temperatuurafhankelijkheid in de oplosbaarheid zijn Na_2CO_3 en Na_2SO_4 gebruikt in de experimenten. Een superversadigde oplossing kan dan makkelijk verkregen worden door de temperatuur te veranderen. Om de temperatuur van het sample te regelen, is een samplehouder gemaakt die voorzien is van een koelspiraal waardoor een koelmiddel loopt. Er is voor gezorgd dat het koelmiddel en de houder geen invloed hebben op het kwantitatieve karakter van de NMR metingen. De zoutoplossing is versadigd bij $40\ ^\circ\text{C}$, daarna ingebracht in het materiaal en gekoeld tot $2\ ^\circ\text{C}$. Nadat nucleatie had plaatsgevonden, is de temperatuur verhoogd terwijl NMR metingen werden gedaan. Voor bulk Na_2CO_3 is de uit de literatuur bekende oplosbaarheid gereproduceerd, terwijl voor Na_2CO_3 oplossing

in poriën van 7 en 10 nm een significante toename in de oplosbaarheid is gevonden. Dit resulteert in een schatting voor de oppervlakte spanning van $\text{Na}_2\text{CO}_3 \cdot 10\text{H}_2\text{O}$ kristallen van $\sigma = (0.09 \pm 0.02)$ N/m. Voor Na_2SO_4 valt de gemeten oplosbaarheid voor zowel de bulkoplossing als die in de poriën samen met die van $\text{Na}_2\text{SO}_4 \cdot 7\text{H}_2\text{O}$ kristallen, en er is geen porie-afhankelijkheid in de oplosbaarheid gevonden. Daarom kan er geen significante kristallisatie druk bestaan voor $\text{Na}_2\text{SO}_4 \cdot 7\text{H}_2\text{O}$. Van deze $\text{Na}_2\text{SO}_4 \cdot 7\text{H}_2\text{O}$ kristal fase is bekend dat hij metastabiel is. In één experiment is het gelukt om $\text{Na}_2\text{SO}_4 \cdot 10\text{H}_2\text{O}$ kristallen in poriën van 7 nm te vormen. Deze meting laat een toename in de oplosbaarheid zien, aan de hand waarvan een schatting voor de oppervlaktetenspanning $\sigma = (0.10 \pm 0.04)$ N/m is gemaakt. Gebaseerd op de schattingen voor de oppervlaktetenspanning kan de maximale poriestraal waarbij schade door zout kan ontstaan worden bepaald, dit is 12 nm en 20 nm voor respectievelijk $\text{Na}_2\text{CO}_3 \cdot 10\text{H}_2\text{O}$ en $\text{Na}_2\text{SO}_4 \cdot 10\text{H}_2\text{O}$.

Behalve model poreuze materialen, zijn er ook experimenten gedaan aan bouwmaterialen. Deze metingen toonden $\text{Na}_2\text{SO}_4 \cdot 7\text{H}_2\text{O}$ kristallen in Savoniere steen, kalkzandsteen en baksteen. In deze materialen was geen voorkeur voor een bepaalde poriegrootte te zien. In mortel werden $\text{Na}_2\text{SO}_4 \cdot 10\text{H}_2\text{O}$ kristallen gevormd, en deze vormden in de grootste poriën, dus met de laagst mogelijke kristallisatiedruk.

Om nog meer informatie over de kristallisatie in poreuze materialen te krijgen zijn ook sorptiemetingen gedaan. Vergeleken met NMR is sorptie wat minder direct. Met de laatst genoemde techniek is het mogelijk om superversadiging waar te nemen in poriën van ongeveer 7 nm, maar voor grotere poriën is de techniek ongevoelig. De experimenten toonden een toegenomen oplosbaarheid voor NaCl ($\sigma = (0.08 \pm 0.02)$ N/m) en thenardiet (watervrije Na_2SO_4 , $\sigma = (0.24 \pm 0.05)$ N/m). Dit komt overeen met een maximale poriegrootte waarbij schade kan ontstaan van 5 en 100 nm voor respectievelijk NaCl en thenardiet.

Contents

1	Introduction	1
1.1	Introduction	1
1.1.1	Efflorescence	2
1.1.2	Structural damage	2
1.2	Salt damage mechanisms	3
1.2.1	Hydration	3
1.2.2	Differential thermal expansion	4
1.2.3	Crystallization pressure	4
1.3	Historical review	5
1.4	Outline of this Thesis	8
2	Crystallization Theory	9
2.1	Introduction	9
2.2	Crystallization pressure	10
2.3	Anhydrous crystal in saturated material	12
2.4	Hydrous crystal in saturated material	16
2.5	Anhydrous crystal in unsaturated material	18
2.6	Hydrous crystal in unsaturated material	21
2.7	Conclusion	23
3	Nuclear Magnetic Resonance	25
3.1	Semi classical model of NMR	25
3.2	Quantum-mechanical description	27
3.3	Spin-echo technique	30
3.3.1	Hahn sequence	32
3.3.2	Carr-Purcell-Meiboom-Gill sequence	33
3.3.3	Saturation recovery	33
3.4	NMR and porous materials	34
3.4.1	Pore relaxation behavior	34
3.4.2	Pore size distribution from relaxation measurements	36
3.5	Summary	38
4	NMR Scanner	39
4.1	Introduction	39
4.2	Setup	40

4.3	Typical parameters and examples	43
5	Sodium NMR relaxation in porous materials	47
5.1	Introduction	47
5.2	Relaxation model	48
5.3	Relaxation measurements	49
5.3.1	Solution	49
5.3.2	Porous material	51
5.4	Discussion	54
5.5	Conclusions	56
6	Salt supersaturation determined by NMR	57
6.1	Introduction	57
6.2	Theory	58
6.3	Materials and Methods	61
6.4	Results	65
6.4.1	Sodium carbonate	65
6.4.2	Sodium sulfate	69
6.4.3	Salt in Building materials	72
6.5	Discussion	75
7	Sorption measurements on salt contaminated porous media	79
7.1	Introduction	79
7.2	Theory	80
7.2.1	Thermodynamic approach	81
7.2.2	Salt and porous material	84
7.3	Materials and Methods	86
7.4	Bulk salts	88
7.5	Salt in a porous material	92
7.6	Discussion	96
8	Concluding remarks	97
	Appendix A: Phase Diagrams & Salt Data	101
	Appendix B: List of symbols	104
	Bibliography	105
	Curriculum Vitae	110
	Dankwoord	111

1. Introduction

1.1 Introduction

The durability of building materials is an issue with large implications. Besides practical aspects – to know when maintenance is needed – also financial aspects – how to maintain economically – as well as cultural aspects – how to preserve for future generations – are relevant. In this chapter an overview of the processes and implications relevant to this issue will be presented and the research reported in this thesis will be defined.

The most important factor governing the durability is most likely weathering. Weathering involves various processes. The combination of the building material used and environment determines which weathering mechanism is most damaging. One of the processes is weathering by moisture. Moisture can enter building materials by for instance rain, condensation, or capillary rise. Moisture transport in building materials can result in growth of micro organisms [Sch01], ranging from bacteria, algae, and fungi [Ada94][Goo03] to moss. Micro-organisms cause damage by producing acidic secretions such as oxalic acid, whereas plants can create mechanical stresses by sending roots into crevices. Also freeze/thaw cycles of water inside the porous material can result in damage. Freeze/thaw cycles are responsible for potholes in highways and cracking and spalling of artwork.

Besides the damage caused by the presence of moisture, the moisture also brings along contaminations such as salts. These salts are also a cause of degradation of building materials. For instance, reinforced concrete is very vulnerable to attack of Cl^- ions, since these act as an accelerator to corrosion of the reinforcement steel [Gou97]. In practice, concrete structures are analyzed frequently to verify the Chloride intrusion in the construction, for example in the "Delta werken" in the south-west part of the Netherlands. Not only chloride ions are responsible for corrosion, also electro-chemical corrosion caused by sulphates takes place. Another example is the erosion of stones because of acidic rain. In this case the contaminations in the rain droplets react with the stone and form soluble complexes by which the stone rains out. Also contaminations from the rain can react with the building material to form badly soluble salts. For instance, oxides of sulfur, originating from fossil fuels and deposited by acid rain, can react with calcium-bearing stone to form gypsum.

Salts, present in building materials, can in principle change the hygroscopic properties of the material. Because of this the material can be a better substrate

for fungi, algae and moss, with damage as a consequence.

One of the most damaging effects of salt is crystallization. During the dry-out, salt crystallizes at the surface, called efflorescence, or inside the material, where it can cause structural damages.

1.1.1 Efflorescence

In many newly built structures salt efflorescence is observed during the spring, since this is the time of year in which the walls dry and wash out salts [Pel02]. The damage caused by efflorescence is mainly a visual damage on the outside. The white spots return every year for the first few years, or in some cases every year. In the summer they disappear as rain cleans the surface. A typical example of efflorescence is given in figure 1.1. Four years later this same wall during the spring, still shows efflorescence as can be seen in figure 1.2. Now the efflorescence is less pronounced, but it can be seen that the lower part of the wall is covered with moss. As can be seen in this example several damage mechanisms can be observed at the same time.



Figure 1.1: *A typical example of salt efflorescence.*

1.1.2 Structural damage

Besides efflorescence and moss growth, after four years also structural damage appears in this example. In the lower part of the wall a thin layer is chipping off (see figure 1.3). Another example of structural salt damage is given in figure 1.4, a monument dedicated to first world war soldiers in La Rochelle (France) suffers erosion. This statue is placed about 200 meter from the sea and hence sea salts are transported into the statue (sea salt spray), crystallize inside and cause fracture. Many of these examples can be found.

Salt weathering processes do not selectively occur in the built environment only, but also contributed in geology to shape the world as it is today. Such processes



Figure 1.2: *The same wall as in figure 1.1 four years later. It can be seen that the efflorescence has decreased but the lower part of the wall is covered with moss.*

have been taking place for thousands of years and have shaped many impressive features, like salt domes or tafoni (see figure 1.5). Salt weathering is therefore a general phenomenon. It is observed on all six continents of the earth in buildings or rock formations. It has even been suggested to be responsible for honeycomb structures, observed by NASA's pathfinder mission, on the surface of Mars [Rod98].

In essence, stone in both building material and rock experiences the same salt related damage processes. A fundamental understanding of what happens exactly is lacking. Many hypotheses and experiments have been published, which have kept *different* theories alive. This thesis presents both theoretical and experimental work to understand one of these hypotheses: crystallization pressure. Also the question which combination of building material and environment is vulnerable to this weathering mechanism will be answered. In section 1.2 the three most plausible hypotheses for salt weathering are discussed. In section 1.3 the scientific work reported in the literature is reviewed and the research issue for the present thesis is further defined. The outline of the remainder of the thesis is presented in section 1.4.

1.2 Salt damage mechanisms

In literature various hypotheses have been reported why salt causes mechanical damages. The three most plausible ones are hydration of salt, differential dilatation, and crystallization pressure. These three mechanisms will be briefly discussed here.

1.2.1 Hydration

A hypothesis commonly found is that hydration induces damage [Mor33]. It states that because of hydration of the salt, the crystals expand. This expansion can be



Figure 1.3: *Lower part of the wall of figure 1.1 after four years: a layer of material is chipping off.*

quite significant and hence result in a pressure. For instance, the anhydrous crystal Na_2SO_4 has a molar volume of $53 \text{ cm}^3/\text{mol}$ whereas mirabilite ($\text{Na}_2\text{SO}_4 \cdot 10\text{H}_2\text{O}$) has a molar volume of $220 \text{ cm}^3/\text{mol}$. Hydration transitions are induced by the relative humidity. In a material subjected to a regular day/night cycle, a hydration/dehydration cycle takes place and damage is induced.

However, Flatt [Fla02b] has pointed out that the pressure caused by this transition is in fact crystallization pressure (see subsection 1.2.3). It was shown experimentally [Rod99a] that the transition from one state to a more hydrated state means that it first dissolves and then precipitates. In that case, expansion of the existing anhydrous salt crystal is unlikely.

1.2.2 Differential thermal expansion

A second hypothesis commonly found in literature is the difference in thermal expansion between salts and the solid matrix of the porous building material. This can generate stress and hence damage. As an example, Halite (NaCl) expands by approximately 0.9% between 0 and 100°C whereas the volume expansion of granites and calcite is about 0.3% in this range [Gou97]. This mechanism will show up in many buildings that experience a day/night cycle, but it is not able to explain durability testing of building materials at constant temperature [Fla02a] which reveal a serious amount of damage. Hence another mechanism must exist.

1.2.3 Crystallization pressure

Crystallization pressure is the third hypothesis which explains salt damage. The principle is that the crystal size equals the pore size. Because the surface of the crystal-liquid interface is curved and a surface tension exists, the crystal is under



Figure 1.4: *A statue of a soldier in La Rochelle (France). The legs of the statue have suffered erosion caused by salts. (Photo by Rob van Hees)*

pressure. The pore wall stops the growth of the crystal, and hence the pore wall experiences the same pressure. In this thesis the mechanism of crystallization pressure will be evaluated. The existence of this mechanism will be proven experimentally, and the parameters for which it is damaging will be discussed. In the next section a review of the relevant literature is given and some basic principles of crystallization pressure are mentioned.

1.3 Historical review

The first scientific study about salt crystallization and pressure was done by Lavalley [Lav53] and was published in 1853. In that paper the first experiments indicating the ability of salts to push away a certain weight are published. His results were not generally accepted. Kopp [Kop55] in 1855 denied the possibility of salts to lift, because in his experiments it did not occur. In 1905 Becker and Day [Bec16] showed by experiments that crystals with a diameter of 1 cm are able to lift 1 kg. Their paper did not have much impact. Bruhms and Meckelenburg [Bru13] tried to reproduce the results but in their experiments salt crystals could not lift a weight. In 1916 Taber [Tab16] reviewed the work present to that time, along with a number of other experiments. He came to the following hypothesis. If a crystal is present in a saturated solution (figure 1.6) it is able to lift a certain weight. If at the same time another crystal is present which does not have any weight on it the first crystal no longer can lift the weight. In this way he explained the experiments in which salts cannot lift. The basic principle behind these observations is that a crystal under pressure is in equilibrium with a solution having an increased solubility. This is in



Figure 1.5: *An example of holes (tafoni) in rock formations. The origin of this weathering phenomenon is salt weathering. This picture was taken in Arches National Park, Moab, Utah, USA.*

building materials literature commonly referred to as supersaturation. When the same salt without pressure also resides in the same solution this will grow, thereby eliminating the supersaturation.

Correns' [Cor49] paper in 1949 is the first that reported mathematics to calculate the supersaturation ratio. However, it is the original work of Thomson [Tho62] which explains that a crystal under excess pressure p is in equilibrium with a supersaturated solution according to

$$RT \ln \left(\frac{C}{C_0} \right) = \nu p, \quad (1.1)$$

where C is the actual concentration, C_0 the saturation concentration, p the pressure, and ν the molar volume of the salt. The principle is the same as that of ice under pressure, which is in equilibrium with supercooled water.

As mentioned above in literature *supersaturation* is used to describe this phenomenon. This is a little confusing since supersaturation is also the state in which no equilibrium exists, because of, for instance, lack of nucleation. The case studied in this thesis is the equilibrium case in which the solubility of the salt is increased. It is important to notice that all results in this thesis resemble an equilibrium situation, unless stated otherwise.

Today a lot of literature is available about salt crystallization damage. Reviews about salt weathering have been written by Weber [Web85], Duttlinger and Knöfel [Diu93], Goudie and Viles [Gou97], and Scherer [Sch99].

Arnold & Zehnder [Zeh89] have investigated the structure of salt in salt efflorescence with Scanning Electron Microscopy. They also studied the structure of salt crystals inside fractures of building materials. Their results are interesting al-

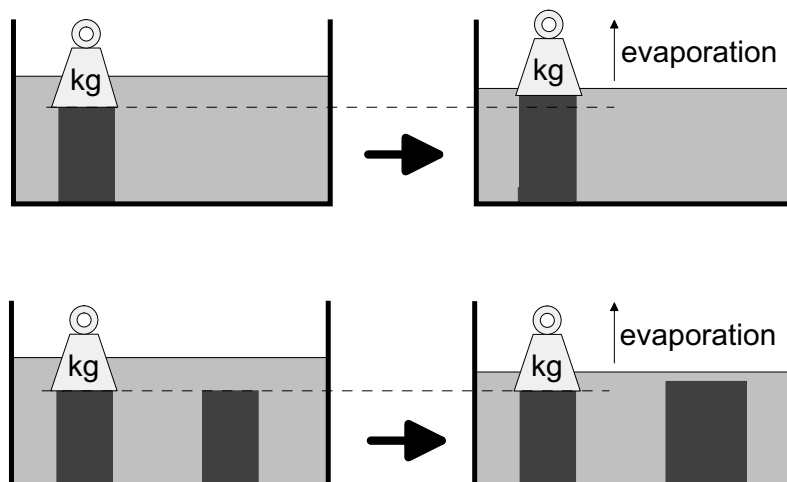


Figure 1.6: *Illustration of the crystallization experiments performed by Taber. When evaporation of the solution takes place in the upper experiment, the crystal is under pressure, the solution is supersaturated and the crystal can grow. In the lower experiment the crystal which is not under pressure determines the concentration in the solution and hence grows. The crystal under pressure does not grow.*

though they acknowledge that: "We can only see the result of the process on the dried and broken material". It is therefore difficult to make a statement about the fracture process because the measurements have been done after drying and salt crystallization.

Putnis and Mauthe [Put01] studied the crystallization process of Halite (NaCl) in layers of porous rock. They conclude that when a fluid in a porous rock is supersaturated with respect to crystallization, the threshold value of the supersaturation at which precipitation occurs depends on the pore size.

Doehne and Rodriguez-Navarro [Rod99a] identify salt weathering as a major cause of deterioration of build environment. "It is obvious that salt weathering is not only of academic interest but it is a hazard with significant cultural and economic implications", they argue. They also identify that the same physical effects are taking place in geology where they cause tafoni and honeycomb weathering. They investigate the damage caused by salts, and use NaCl and Na₂SO₄ as model salts. They conclude: "The extent of salt damage in porous stone due to crystallization pressure appears to be largely a function of solution supersaturation ratio and the location of crystallization. (...) differential damage behavior between sodium chloride and sodium sulphate appears largely to be due to differences in crystallization patterns, dynamics, and the location of the precipitates." They observe that their experiments are in agreement with the model proposed by Correns, but suggest

that more experiments need to be done for further understanding. They note that thenardite, at the same supersaturation ratio, has a higher crystallization pressure than mirabilite, and that at low relative humidities direct precipitation of thenardite takes place. Their experiments in an Environmental SEM [Rod99b], [Rod00a] cast doubt on the hypothesis of hydration pressure. This is triggered by their direct observation of the transformation from thenardite to mirabilite in which first the salt dissolves and then precipitates as the other phase. They argue that hydration is not the damage mechanism since the salt does not increase in size.

Also Flatt strongly opposes to the idea of hydration pressure. Flatt [Fla02b] theoretically motivates the idea that hydration pressure is a sub-set of crystallization pressure in which case the supersaturation is caused by the dissolution of the anhydride.

It is clear that the debate about crystallization pressure and supersaturation is ongoing for one and a half century now. Various theoretical models to describe it were made, however a complete model is lacking. For instance the influence of the saturation of the porous medium has not been theoretically described as yet. Various experiments have been reported, however the supersaturation ratio of a solution inside a material was never directly measured. In this thesis a complete thermodynamic model is presented for crystallization pressure and supersaturation, incorporating both the degree of fluid saturation of the porous material and the hydration state of the crystals. By using Nuclear Magnetic Resonance (NMR) the salt concentration of the solution inside the porous medium can be measured directly without disturbing the sample. Having used NMR experiments will be presented that directly reveal the supersaturation ratio inside a porous material.

1.4 Outline of this Thesis

Several chapters of this thesis have been written to be published in literature as well, therefore the thorough reader will find some redundant information. On the other hand this enables the quick reader to read these chapters separately. In chapter 2 the theory describing crystallization of salts inside porous media is presented. Especially the influence of hydration of the crystal and the degree of saturation of the porous medium are discussed. By means of NMR the behavior of the salts can be studied. Chapter 3 discusses the NMR technique. Because Na-NMR is more complex than H-NMR, chapter 5 describes the possibilities to obtain additional information concerning the pore size distribution from Na-NMR measurement. Measurements of the degree of supersaturation inside porous media are presented in chapter 6. Chapter 7 describes sorption experiments onto salt contaminated porous materials. Finally, chapter 8 discusses the theoretical and experimental evidence and evaluates the capacity of crystallizing salts to cause damage.

2. Crystallization Theory

abstract

Salts are widely recognized as a cause of deterioration of porous building materials. One of the proposed mechanisms for salt weathering is crystallization pressure. Salt crystals in pores are under pressure because of their own surface energy. A signature of this excess pressure is the enhanced solubility of a crystal inside a pore (called supersaturation). Using a thermodynamic approach, we derive the relation between the supersaturation ratio and the crystallization pressure for a crystal inside a porous material. We show that the saturation of the porous material influences the amount of pressure exerted on the porous material, and the supersaturation ratio. We determine for which pore sizes the mechanism can cause damage, and conclude that the crystallization pressure can not explain damage in building materials having only large pores.

2.1 Introduction

Salts are widely recognized as an important cause of damage of porous building materials, used in modern structures as well as cultural heritage [Eva69][Gou97], and damage of rock [Doe02]. Although various mechanisms have been proposed, there is an ongoing debate about the relevance of these mechanisms for salt weathering. A mechanism which has received a lot of attention is based on the so called crystallization pressure [Cor49]. In this chapter we will evaluate this mechanism, its thermodynamical backgrounds, and its importance.

Lavalle [Lav53] was the first to observe that salts are able to push weights. One of the proposed damage mechanisms is the action of this force in building materials. In 1949 Correns published his well known paper [Cor49] introducing the relation between solubility and crystallization pressure. Although the physical background of this phenomenon has been studied in detail recently [Sch99][Fla02a][Rod99a][Rod00a], there are still a number of open issues. First of all, a thermodynamic approach for a porous material partially saturated with solution is lacking. This is an essential

issue because most building materials and rocks are partially saturated¹ in practice. Secondly, the crystallization pressure has not been calculated for hydrous crystals. This is of interest because for typical damaging salts like Na_2SO_4 several hydration phases are found in practice.

In this chapter we will discuss various possible situations. In section 2.2 the equations for the crystallization pressure are derived. Section 2.3 discusses the case in which the pores of the material are fully saturated with a salt solution and an anhydrous crystal is formed. Section 2.4 describes the situation of a fully saturated material in which a hydrous crystal is formed. Next, in section 2.5 theory is treated in which the material is unsaturated and an anhydrous crystal is formed. Section 2.6 explains the case of an unsaturated material in which a hydrous crystal is formed. In section 2.7 we will draw some conclusions for the possible damage, resulting from crystallization pressure.

2.2 Crystallization pressure

In this section the crystallization pressure is calculated. This is a pressure difference between the solution and the salt crystal. Its origin is the surface tension (or interfacial tension) of the liquid-salt interface. As a matter of notation the subscript always denotes the species (w = water, s = salt) and the superscript always denotes the phase (c = crystal, l = liquid, v = vapor, s = solid i.e., the pore wall).

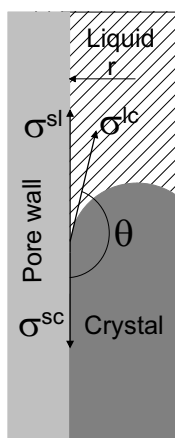


Figure 2.1: *Schematic of a crystal near the pore wall and the three surface tensions of the interfaces between liquid and crystal (σ^{lc}), liquid and solid (σ^{ls}) and solid and crystal (σ^{sc}).*

Figure 2.1 shows schematically the surface tensions that have to be taken into

¹Note that *saturation* in this chapter has two physical meanings. First, saturation of the material refers to the degree of filling of the pore system by the liquid. Second, saturation of a salt solution means that the salt concentration in the solution has reached the solubility limit.

account: σ^{sl} , σ^{sc} , and σ^{cl} which are the solid-liquid, solid-crystal, and crystal-liquid surface tensions², respectively. The crystal has a contact angle θ with the pore wall, as given in figure 2.1. We will calculate the pressure for a closed cylindrical pore with radius r . We start with the expression for the free energy (F) [Kat65]:

$$dF = -pdV - SdT + \mu dN. \quad (2.1)$$

in which p is the pressure, V the volume, S the entropy, T the temperature, μ the chemical potential and N the number of particles. For the present system, this can be written as a sum over the various phases. Doing so one writes the free energy for every phase and also accounts for the interfaces between the phases by their surface tensions:

$$dF = -p^c dV^c - p^l dV^l - S^c dT^c - S^l dT^l + \mu^c dn^c + \mu^l dn^l + \sigma^{cl} d\xi + \sigma^{sl} d\tau + \sigma^{sc} d\tau', \quad (2.2)$$

in which σ^{ij} is the surface tension of the interface ij , ξ is the surface of the crystal solution interface, τ the surface of the pore wall-liquid interface, and τ' the surface area of the pore wall-crystal interface. The total volume of the system is constant, therefore $dV^s = -dV^c$, and the temperature is constant therefore $dT = 0$. The total number of particles in the system is constant therefore $dn^c = -dn^l$. Using these conditions Eq. 2.2 reduces to:

$$dF = (p^c - p^l)dV^l + (\mu^c - \mu^l)dn^c + \sigma^{sl}d\xi + \sigma^{sl}d\tau + \sigma^{sv}d\tau'. \quad (2.3)$$

Because the system is in equilibrium, no transport between the two phases occurs, i.e., the phases are not transforming into each other, therefore $dn^c = 0$. We now define the crystallization pressure as $p = p^c - p^l$ and Eq. 2.3 reduces to

$$dF = pdV^l + \sigma^{cl}d\xi + \sigma^{sl}d\tau + \sigma^{sc}d\tau'. \quad (2.4)$$

Because the system is closed, it is clear that if the solid-liquid surface increases, the solid-crystal surface decreases by the same amount, i.e., $d\tau' = -d\tau$. This results in:

$$dF = pdV^l + \sigma^{cl}d\xi + (\sigma^{sl} - \sigma^{sc})d\tau. \quad (2.5)$$

Because of mechanical equilibrium in the vertical direction Young's equation applies:

$$\sigma^{cs} + \sigma^{cl} \cos \theta = \sigma^{sl} \quad (2.6)$$

Using this we obtain

$$dF = pdV^l + \sigma^{cl}d\xi + \sigma^{cl} \cos \theta d\tau. \quad (2.7)$$

Because our system is in equilibrium, the shape of the liquid vapor interface is stable, i.e., $d\xi = 0$. Now the cylindrical geometry is used writing the liquid volume as $V^l = h\pi r^2 + \zeta$, in which r is the radius, h the height of the liquid phase in the

²In literature surface tension (in N/m) and surface energy (in J/m²) are often used to describe the same quantity.

pore and ζ a correction term because the surface of the liquid crystal surface is a half sphere. The surface of the liquid phase is given by $\tau = h2\pi r + \eta$ in which η is a correction term for the bottom surface. We can then write down dV^l and $d\tau$:

$$dV^l = \pi r^2 dh \quad (2.8)$$

and

$$d\tau = 2\pi r dh. \quad (2.9)$$

Because the system will adopt the state in which F has a minimum value, the final result is given for $dF = 0$:

$$p = \frac{-2\sigma^{cl} \cos \theta}{r}. \quad (2.10)$$

2.3 Anhydrous crystal in saturated material

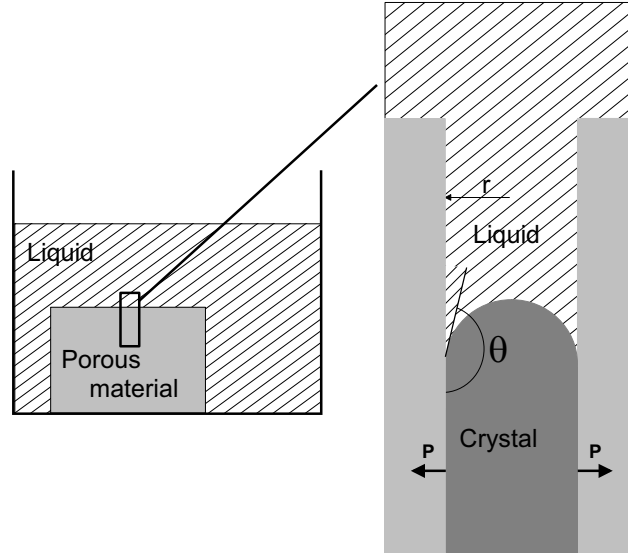


Figure 2.2: *A crystal in a pore in a saturated porous material.*

We start with an anhydrous crystal inside a porous material which is fully saturated. The pores are modelled as cylinders with a radius r . This situation is given in figure 2.2. In this figure the porous material is completely immersed in the solution. An important feature is the fact that the liquid-vapor interface can be considered as flat. Therefore the pressures in the liquid and the vapor phases are equal at equilibrium [Ada60]. This situation also applies to a porous material in which the water-vapor interface is located in large pores, and therefore the surface of the interface can be considered flat in our problem. For the isothermal situation the Gibbs-Duhem equation for the liquid phase is given by:

$$-N_w^l d\mu_w^l - N_s^l d\mu_s^l + V^l dp^l = 0, \quad (2.11)$$

for the crystal phase by:

$$-N_w^c d\mu_w^c - N_s^c d\mu_s^c + V^c dp^c = 0, \quad (2.12)$$

and for the vapor phase by:

$$-N_w^v d\mu_w^v + V^v dp^v = 0, \quad (2.13)$$

where V (in m^3) and p (in Pa) are the volume and pressure, respectively, N_a and μ_a (in J) are the number of moles and the chemical potential of species a . Note that we do not have to treat the cations and anions separately, because the solution is electrically neutral [Kat65]. Because the crystal is anhydrous $N_w^c = 0$. Due to the fact that the liquid-crystal interface is curved, it follows from the condition of mechanical equilibrium that the pressure difference between the liquid and crystal phase is given by [Ada60]:

$$p^c - p^l = -\frac{2\sigma^{cl} \cos \theta}{r}, \quad (2.14)$$

where σ^{cl} is the surface tension (in Nm^{-1}) of the surface between crystal and liquid phase. As a result a pressure difference between the crystal and the liquid exists. In the case of a contact angle $\theta > 90^\circ$ the crystal is under pressure. The contact angle θ and surface tension σ^{cl} are often assumed to be material constants [Ada60]. To simplify the equation for mechanical equilibrium we define $A \equiv -\sigma^{cl} \cos \theta$, and $J \equiv 2/r$. Then we can write:

$$dp^c - dp^l = AdJ. \quad (2.15)$$

As explained above no pressure difference exists between the vapor and liquid phase:

$$dp^v - dp^l = 0. \quad (2.16)$$

Because the system is in chemical equilibrium, $d\mu_s^c = d\mu_s^l = d\mu_s$ and $d\mu_w^l = d\mu_w^v = d\mu_w$. We introduce the molar volume³ $\nu_i^j = V^j/N_i^j$ (in $\text{m}^3 \text{mole}^{-1}$), and $\chi C = N_s^l/V^l$, in which C [molar] is the concentration and $\chi = 10^3 \text{ l/m}^3$ gets in because the concentration is commonly given in molar instead of mole/ m^3 . Solving Eq. 2.11 to 2.16 results in

$$\left(\frac{1}{\nu_s^c} - \frac{\chi C \nu_w^l}{\nu_w^l - \nu_w^v} \right) d\mu_s = AdJ. \quad (2.17)$$

Because the molar volume of the water in the gas phase is much larger than the molar volume of the water in the liquid phase, ν_w^l can be neglected compared to ν_w^v . Considering that $C\nu_w^l = N_s^l/N_w^l \ll 1$ and $1/\nu_w^v < 1/\nu_s^c$ we can neglect $C\nu_w^l/(\nu_w^l - \nu_w^v)$ compared to $1/\nu_s^c$. The result is:

$$\frac{1}{\nu_s^c} d\mu_s = AdJ \quad (2.18)$$

³Note that the molar volume is defined here as $\nu_i^j = V^j/N_i^j$, and is a reversed density of the species. It should not be confused with the partial molar volume \tilde{v}_i^j .

Now we substitute [Kat65]

$$d\mu_s = \tilde{v}_s^l dp^l + nRT d \ln a, \quad (2.19)$$

in which a is the activity, \tilde{v}_s^l is the partial molar volume, n the number of ions per neutral unit salt (2 for NaCl and 3 for Na₂SO₄). We consider the pressure of the vapor phase to be constant, and because no pressure difference exists (eq. 2.16) $dp^l = 0$. Eq. 2.18 transforms in:

$$\int_{a_0}^a \frac{nRT}{\nu_s^c} d \ln a = \int_0^{2/r} AdJ, \quad (2.20)$$

and after integration:

$$\frac{nRT}{\nu_s^c} \ln \left(\frac{a}{a_0} \right) = \frac{2A}{r}. \quad (2.21)$$

The activity can be written as [Kat65] $a \equiv \gamma^\pm C$, where γ^\pm and C are the mean activity coefficient and the concentration of the ion pair, respectively. Values of these parameters can be found in literature, e.g. [Lid98], [Rod01], [Mei63], [Lob89]. Now Eq. 2.21 can be written as:

$$\frac{nRT}{\nu_s^c} \ln \left(\frac{C}{C_0} \right) + \frac{nRT}{\nu_s^c} \ln \left(\frac{\gamma^\pm}{\gamma_0^\pm} \right) = \frac{2A}{r}, \quad (2.22)$$

in which C_0 and γ_0^\pm are the solubility and mean activity coefficient at $C = C_0$, respectively. In order to estimate the influence of the activity coefficients we can expand the term γ^\pm in a Taylor series around $C = C_0$:

$$\gamma^\pm = \gamma_0^\pm + \left(\frac{d\gamma^\pm}{dC} \right)_{C_0} (C - C_0) + \quad (2.23)$$

It follows from Eq. 2.23 that ($\gamma^\pm \simeq \gamma_0^\pm$) when the following criterion is satisfied:

$$\left| \frac{1}{\gamma_0^\pm} \left(\frac{d\gamma^\pm}{dC} \right)_{C_0} (C - C_0) \right| \ll 1. \quad (2.24)$$

As an example we will consider Na₂SO₄. Typical values of interest for the concentration C are close to the solubility of the salt, therefore we use $C_0 = 3\text{M}$. The mean activity is $\gamma = 0.139$ at 3M, see figure 2.3. The derivative is given in the inset of figure 2.3, from which a value $(1/\gamma_0^\pm)(d\gamma^\pm/dC) = -0.053 \text{ M}^{-1}$ at 3 M can be obtained. With these numbers expression 2.24 transforms into $0.053(C - 3) \ll 1$. As example, for a concentration of 5 molal, the left hand side equals 0.1. Therefore variations in the activity coefficients can be neglected. From this it follows that Eq. 2.22 can be written as

$$\frac{nRT}{\nu_s^c} \ln \left(\frac{C}{C_0} \right) = \frac{2A}{r}, \quad (2.25)$$

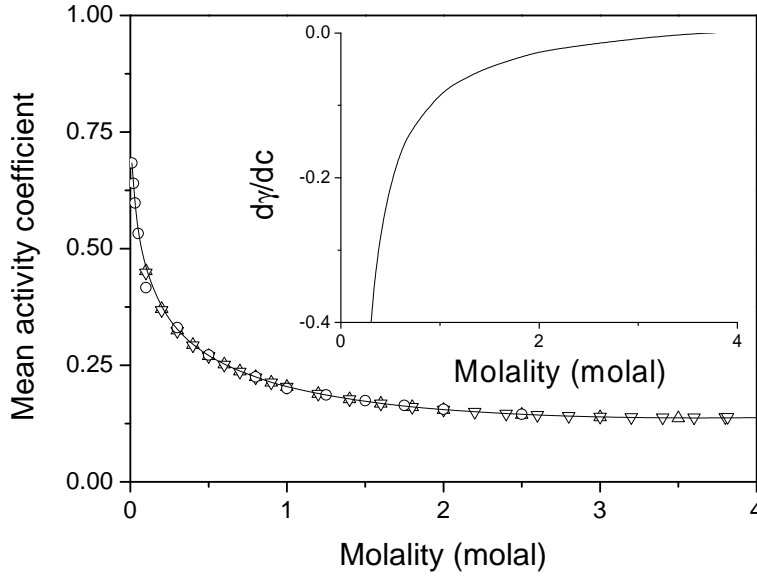


Figure 2.3: Mean activity of Na_2SO_4 . Data: \triangle [Mei63]; ∇ [Lob89]; \circ [Rod01]. All data sets are in near perfect agreement. The inset shows the first derivative of the mean activity.

where C/C_0 is defined as the supersaturation ratio. For the case $\theta > 90^\circ$ the crystal is under pressure because of its surface energy, and the crystal is in equilibrium with a supersaturated solution. For the case $\theta < 90^\circ$ the crystal is in equilibrium with a subsaturated solution. In other words the solubility of the crystal is changed by the compressive stress on the crystal. Inside porous material $\theta > 90^\circ$ is usually expected [Sch99]. Eq. 2.25 is the equation commonly cited in literature [Cor49][Sch99]. We will now estimate the pressure of a Na_2SO_4 crystal. Assuming that $A = 0.1 \text{ J/m}^2$ (which is the case if $\sigma^{cl} = 0.1 \text{ N/m}$ and $\theta = 180^\circ$ [Sch99]) and that this crystal is formed in a cylindrical pore with a radius of 5 nm, we end up with a pressure of $p^c = 40 \text{ MPa}$. This pressure of 40 MPa corresponds with a supersaturation ratio of 1.3 for Na_2SO_4 . For NaCl and the same values of the parameters, this ratio would be 1.2.

Scherer [Sch99] has derived that the change in pressure on the pore wall because of the presence of the crystal is given by:

$$\Delta p = \frac{A}{r}. \quad (2.26)$$

If we compare this to the tensile strength S of the material damage is expected if $p > S$. One can determine a criterion for the pore radius below which this mechanism is damaging:

$$r < \frac{A}{S}, \quad (2.27)$$

For instance, using the typical numbers given above and a tensile strength of 3 MPa which is the typical order of magnitude for building materials, damage can be induced in pores having a pore radius smaller than about 35 nm.

2.4 Hydrous crystal in saturated material

In this section we consider a crystal containing hydration water. In this case, the chemical potential of water is influenced by the fact that water is incorporated in the crystal. We start with the Gibbs-Duhem equations 2.11, 2.12, and 2.13. Note that the amount of water inside the crystal $N_w^c \neq 0$ for a hydrous crystal. Using chemical equilibrium we can rewrite the Gibbs-Duhem equations as follows:

$$\frac{1}{\nu_w^v} d\mu_w = dp^v, \quad (2.28)$$

$$\frac{1}{\nu_w^l} d\mu_w + \chi C d\mu_s = dp^l, \quad (2.29)$$

and⁴

$$\frac{1}{\nu_w^c} d\mu_w + \frac{1}{\nu_s^c} d\mu_s = dp^c. \quad (2.30)$$

By using the condition of mechanical equilibrium at the crystal surface (eq. 2.15) we can combine equations 2.29 and 2.30 to:

$$d\mu_w + \frac{1/\nu_s^c - \chi C}{1/\nu_w^c - 1/\nu_w^l} d\mu_s = \frac{A}{1/\nu_w^c - 1/\nu_w^l} dJ. \quad (2.31)$$

In the same way the condition for mechanical equilibrium at the liquid-vapor interface (eq. 2.16) can be rewritten using eq. 2.28 and 2.29:

$$d\mu_w - \frac{\chi C}{1/\nu_w^v - 1/\nu_w^l} d\mu_s = 0. \quad (2.32)$$

To eliminate μ_w we subtract Eq. 2.32 from Eq. 2.31 and use the fact that the molar volume of the gas ν_w^v is much larger than the molar volume of the liquid ν_w^l ($1/\nu_w^v \ll 1/\nu_w^l$):

$$\left(\frac{1/\nu_s^c - \chi C}{1/\nu_w^c - 1/\nu_w^l} - \nu_w^l \chi C \right) d\mu_s = \left(\frac{A}{1/\nu_w^c - 1/\nu_w^l} \right) dJ. \quad (2.33)$$

Since we showed in section 2.3 that the concentration dependence of the activity coefficient can be neglected, we can directly write the concentration while substituting

⁴It appears as if ν_w^c is a variable here since the amount of water in the crystal can vary, but this is not the case. The salt crystals discussed here always have a constant salt water ratio like for instance $\text{Na}_2\text{SO}_4 \cdot 10\text{H}_2\text{O}$ or $\text{Na}_2\text{CO}_3 \cdot 7\text{H}_2\text{O}$.

Eq. 2.19. Because the system is saturated $dp^l=0$. Then after integration Eq. 2.33 has transformed in:

$$nRT \left[\frac{1}{\nu_s^c} \ln \left(\frac{C}{C_0} \right) - \frac{\chi \nu_w^l}{\nu_w^c} (C - C_0) \right] = \frac{2A}{r}. \quad (2.34)$$

The first term at the left hand side accounts for the influence of the excess pressure in the crystal on the chemical potential of the salt, whereas the second term for its influence on the chemical potential of the water caused by an increase of the osmotic pressure. It is clear that the anhydrous case (eq. 2.25), as discussed in section 2.3, is a limiting case. In an anhydrous crystal the molar volume of the water in the crystal $\nu_w^c \rightarrow \infty$ and Eq. 2.34 transforms into Eq. 2.25.

Table 2.1: *Data of Na_2SO_4 . Except from \tilde{v}_s^l the data are obtained from [Lid98], We have determined \tilde{v}_s^l experimentally.*

ν_s^c (Na_2SO_4)	$5.2 \cdot 10^{-5} \text{ m}^3/\text{mol}$
ν_s^c ($\text{Na}_2\text{SO}_4 \cdot 10\text{H}_2\text{O}$)	$2.2 \cdot 10^{-4} \text{ m}^3/\text{mol}$
ν_w^c ($\text{Na}_2\text{SO}_4 \cdot 10\text{H}_2\text{O}$)	$2.2 \cdot 10^{-5} \text{ m}^3/\text{mol}$
ν_w^l	$1.8 \cdot 10^{-5} \text{ m}^3/\text{mol}$
\tilde{v}_s^l	$3.48 \cdot 10^{-5} \text{ m}^3/\text{mol}$

Figure 2.4 shows the calculated supersaturation ratios for the two phases of Na_2SO_4 , using the data of table 2.1. Note that in this figure it is implicitly assumed that $A = 0.1 \text{ N/m}$ [Sch99] for both phases. The first phase is thenardite, which is the anhydrous Na_2SO_4 phase. The second phase is mirabilite, which is a decahydrated phase, $\text{Na}_2\text{SO}_4 \cdot 10\text{H}_2\text{O}$. This figure shows that at the same $1/r$, corresponding to the same pressure, the supersaturation ratio is different for the two crystal phases.

In order to evaluate which term in Eq. 2.34 is dominant we use the fact that $\ln(1+x)$ in first order equals x for small values of x , and use $C/C_0 - 1$ for x . Equation 2.34 then transforms into

$$nRT \left(\frac{C}{C_0} - 1 \right) \left(\frac{1}{\nu_s^c} - \frac{\chi C_0 \nu_w^l}{\nu_w^c} \right) = \frac{2A}{r}. \quad (2.35)$$

As can be seen both contributions are of the same order of magnitude. This proves that hydrous and non-hydrous crystals behave significantly different under confinement. For the anhydrous crystal, as discussed in section 2.3, the pressure equals $nRT/\nu_s^c \ln(C/C_0)$. In that case the supersaturation ratio C/C_0 is a direct measure for the pressure, as is often assumed [Gou97]. For a hydrous crystal, however, the supersaturation ratio is not a direct measure for the pressure. This is illustrated by figure 2.5 in which the pressure and $nRT/\nu_s^c \ln(C/C_0)$ are plotted for $\text{Na}_2\text{SO}_4 \cdot 10\text{H}_2\text{O}$ as a function of $1/r$. Again it is assumed that $A = 0.1 \text{ N/m}$ [Sch99].

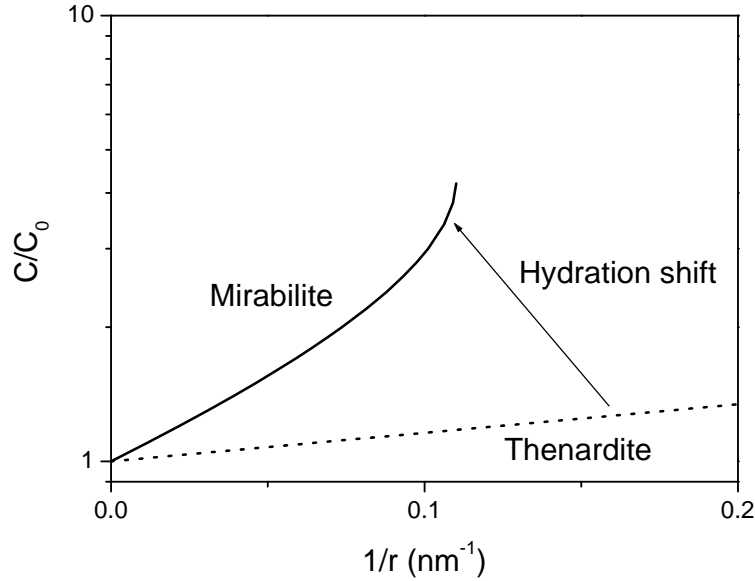


Figure 2.4: Illustration of the difference in supersaturation ratio between Na_2SO_4 (thenardite) and $\text{Na}_2\text{SO}_4 \cdot 10\text{H}_2\text{O}$ (mirabilite) as function of $1/r$. The lines were calculated with the parameters listed in table 2.1 and $A = 0.1 \text{ N/m}$ for both phases.

2.5 Anhydrous crystal in unsaturated material

During the drying of a porous material the concentration of the dissolved salt increases, which causes, at a certain moment, precipitation of salt. During a drying process the total pore space is no longer filled with liquid, which means that the vapor phase enters the porous material and the pressure difference caused by the curvature of the liquid-vapor interface should be taken into account. One of our aims is to investigate the influence of the curvature of this interface on the solubility and the pressure. In this section we discuss an anhydrous crystal. The system is schematically drawn in figure 2.6. A crystal is confined in a pore with radius r . The crystal has a contact angle θ with the pore wall. The solution above the crystal has a contact angle ϕ with the pore wall at the liquid-vapor interface. We start with the Gibbs-Duhem relations, equations 2.11, 2.12, and 2.13. Across the liquid-vapor interface a pressure difference exists, which is given by:

$$p^v - p^l = \frac{2\sigma^{lv} \cos \phi}{r}, \quad (2.36)$$

where σ^{lv} is the surface tension of the liquid-vapor interface. For convenience we define $B \equiv \sigma^{lv} \cos \phi$. The pressure difference between the crystal and the liquid is still given by Eq. 2.15. Following the same approach as in section 2.3, implying

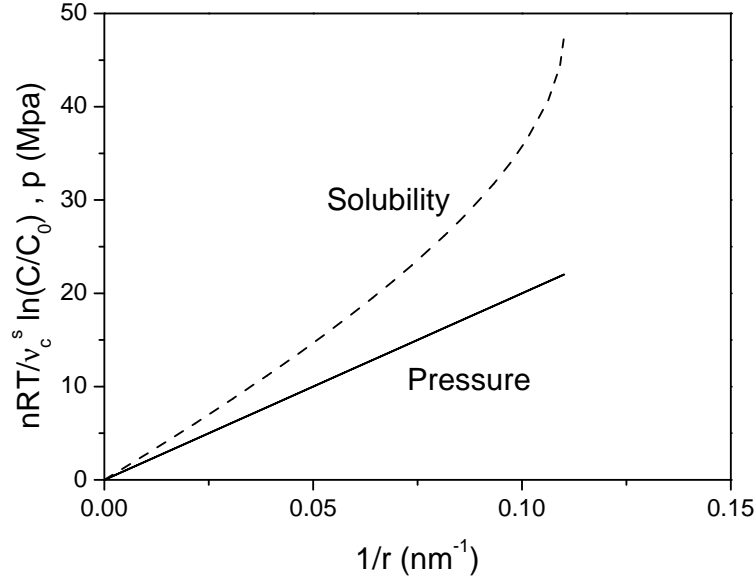


Figure 2.5: Illustration of the difference between $(nRT/\nu_c^s) \ln(C/C_0)$ (dashed curve) and the excess pressure (solid line) in a crystal inside a pore with radius r for $\text{Na}_2\text{SO}_4 \cdot 10\text{H}_2\text{O}$ (mirabilite). The data of table 2.1 and $A = 0.1 \text{ N/m}$ were used for calculation of this figure.

chemical equilibrium, the Gibbs-Duhem equations can be rewritten as:

$$dp^c = \frac{1}{\nu_s^c} d\mu_s, \quad (2.37)$$

$$dp^l = \frac{1}{\nu_w^l} d\mu_w + \chi C d\mu_s, \quad (2.38)$$

and

$$dp^v = \frac{1}{\nu_w^v} d\mu_w. \quad (2.39)$$

Now we combine Eq. 2.37 and 2.39 using Eq. 2.15 to:

$$-d\mu_w + \frac{(1/\nu_s^c - \chi C)}{1/\nu_w^l} d\mu_s = \frac{A}{1/\nu_w^l} dJ. \quad (2.40)$$

We also combine Eq. 2.39 and Eq. 2.38 using Eq. 2.36 and write:

$$d\mu_w - \frac{\chi C}{1/\nu_w^v - 1/\nu_w^l} d\mu_s = \frac{B}{1/\nu_w^v - 1/\nu_w^l} dJ, \quad (2.41)$$

Then we sum the equations 2.41 and 2.40 giving:

$$\left[\frac{\chi C}{1/\nu_w^v - 1/\nu_w^l} + \nu_w^l \left(\frac{1}{\nu_s^c} - \chi C \right) \right] d\mu_s = \left(\frac{A}{1/\nu_w^l} + \frac{B}{1/\nu_w^v - 1/\nu_w^l} \right) dJ \quad (2.42)$$

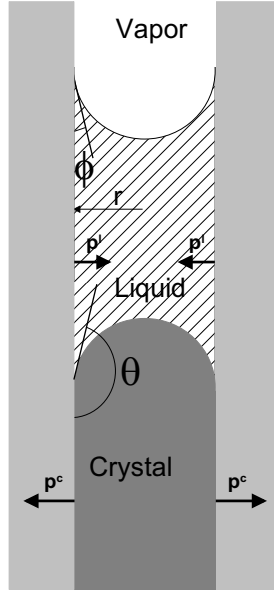


Figure 2.6: A crystal in a pore in an unsaturated porous material. Because of the curvature of the crystal the crystal causes a pressure to the pore wall. On the other hand the liquid is under a lower pressure because of its curvature and hence

Because the molar volume of the vapor is much larger than the molar volume of the liquid ($\nu_w^v \gg \nu_w^l$), the terms $1/\nu_w^v$ can be neglected. This results in

$$\frac{1}{\nu_s^c} d\mu_s = (A - B) dJ \quad (2.43)$$

We use Eq. 2.19 to substitute $d\mu_s$ in Eq. 2.43, and because we assumed p^v constant, end up with

$$\frac{nRT}{\nu_s^c} d \ln C = \left[A - \left(1 - \frac{\tilde{\nu}_s^l}{\nu_s^c} \right) B \right] dJ, \quad (2.44)$$

which can be easily integrated to:

$$\frac{nRT}{\nu_s^c} \ln \left(\frac{C}{C_0} \right) = \left[A - \left(1 - \frac{\tilde{\nu}_s^l}{\nu_s^c} \right) B \right] \frac{2}{r}. \quad (2.45)$$

Figure 2.7 illustrates the situation described in this section indicating the resulting pressure. Using a typical value of $\phi = 0^\circ$ and $\sigma^{lv} = 0.07$ N/m [Lid98] for the surface tension of the solution it appears that A and B are of the same order of magnitude (using a typical value $A = 0.1$ N/m). As an example we calculate for which pore size the pressure now is damaging. Using the typical numbers given above and a tensile strength of 3 MPa, damage can be induced in pores having a pore radius smaller than about 10 nm. If $B > A$ the material is not damaged but compressed.

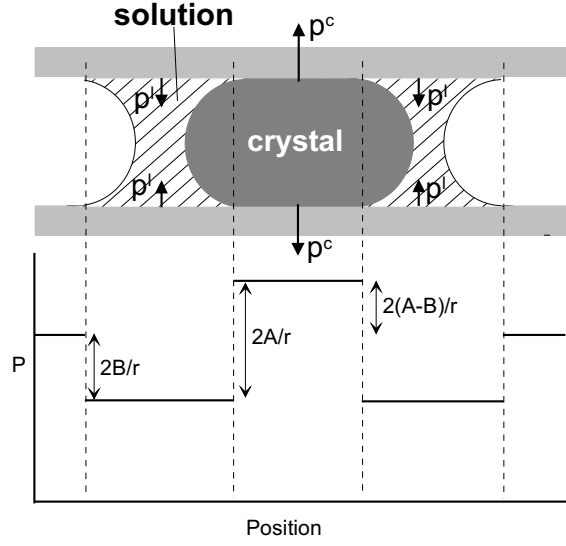


Figure 2.7: *Illustration of the pressures inside an unsaturated porous system containing a crystal. If $A > B$ the pressure caused at the liquid-vapor interface partially compensates the pressure caused at the liquid-crystal interface.*

2.6 Hydrous crystal in unsaturated material

The derivation for an unsaturated porous material containing a hydrous crystal is in fact a combination of the derivation presented in sections 2.4 and 2.5. We use the Gibbs-Duhem equations 2.11, 2.12 and 2.13, and the conditions for mechanical equilibrium at the crystal-liquid (eq. 2.15), liquid-vapor (eq. 2.36) interface and chemical equilibrium. This results in:

$$\left(\frac{1}{\nu_s^c} - \frac{\nu_w^l}{\nu_w^c} \chi C \right) d\mu_s = \left[A - \left(1 - \frac{\nu_w^l}{\nu_w^c} \right) B \right] dJ. \quad (2.46)$$

We use Eq. 2.19 to substitute $d\mu_s$, and end up with the integral:

$$\int_{C_0}^C \frac{nRT/\nu_s^c - \chi nRT C \nu_w^l/\nu_w^c}{(A - B[1 - \nu_w^l/\nu_w^c(1 - \chi C \tilde{\nu}_s^l) - \tilde{\nu}_s^l/\nu_s^c])C} dC = \int_0^{2/r} dJ \quad (2.47)$$

which can be integrated analytically, resulting in:

$$\begin{aligned} \frac{2}{r} = \frac{-nRT/\nu_s^c}{F} & \left[\ln \left(\frac{F + B\tilde{\nu}_s^l \chi C \nu_w^l/\nu_w^c}{F + B\tilde{\nu}_s^l \chi C_0 \nu_w^l/\nu_w^c} \right) - \ln \left(\frac{C}{C_0} \right) \right] \\ & - \frac{nRT}{\tilde{\nu}_s^l B} \ln \left(\frac{F + B\tilde{\nu}_s^l \chi C \nu_w^l/\nu_w^c}{F + B\tilde{\nu}_s^l \chi C_0 \nu_w^l/\nu_w^c} \right). \end{aligned} \quad (2.48)$$

In this equation $F \equiv A - B(1 - \nu_w^l/\nu_w^c - \tilde{\nu}_s^l/\nu_s^c)$. Just as is the case of a saturated hydrous crystal the supersaturation ratio C/C_0 is not a direct measure for the pressure caused by the crystal anymore. Figure 2.8 illustrates the difference between a saturated and an unsaturated material. The supersaturation ratio C/C_0 differs significantly whether the material is fully saturated or not.

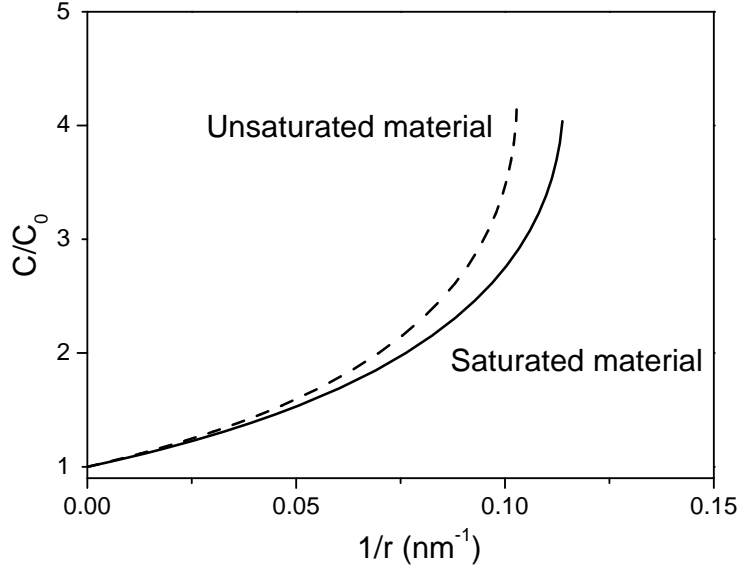


Figure 2.8: *The difference in supersaturation ratio for mirabilite ($\text{Na}_2\text{SO}_4 \cdot 10\text{H}_2\text{O}$) as a function of $1/r$ for a saturated material and an unsaturated material. The values of table 2.1, $A = 0.1 \text{ N/m}$, and $B = 0.07 \text{ N/m}$ were used.*

Finally we want to remark that all previous solubility equations (2.25, 2.34, and 2.45) are limits of Eq. 2.48. Eq. 2.25 and 2.45 can be obtained if $\nu_w^c \rightarrow \infty$. For Eq. 2.34 the limit is less obvious. for $B \rightarrow 0$ the first term at the left hand side becomes

$$\frac{nRT \ln C/C_0}{\nu_s^c A}. \quad (2.49)$$

The second term we evaluate by using the fact that $\ln(1+x)$ for $|x| < 1$ in first order equals x , and use $x = (B/A)(\nu_w^l/\nu_w^c - 1 + \tilde{\nu}_s^l/\nu_s^c + \tilde{\nu}_s^l \chi C \nu_w^l/\nu_w^c)$. Then the second term at the right hand side becomes:

$$\frac{nRT}{A} \frac{\nu_w^l}{\nu_w^c} \chi (C - C_0), \quad (2.50)$$

from which it is clear that Eq. 2.34 is a limit of Eq. 2.48.

2.7 Conclusion

In this chapter we have derived for both anhydrous and hydrous salts the relations between the solubility and the damaging pressure in saturated as well as unsaturated porous material.

When a porous medium dries the liquid-vapor interface enters the material, which to a certain extent compensates the pressure caused by the crystals formed inside. Assuming a tensile strength of 3 MPa for a typical building material, pore radii smaller than about 35 nm are needed to create a pressure large enough to cause damage if the system is fully saturated. If the system is not fully saturated, pore radii smaller than about 10 nm are needed.

For an anhydrous crystal, the supersaturation ratio C/C_0 is a direct measure for the pressure caused by the crystal. This is not the case if the crystal is hydrated. In that case the supersaturation ratio is higher than expected on basis of the pressure.

It follows from our estimations that the crystallization pressure can only explain damage of materials having small pores. However, most building materials have besides small pores also large pores. Because of diffusion, the salt concentration inside the porous material is the same inside pores with various pore radii. In equilibrium the supersaturation ratio will be determined by the largest pores. Unless the material dries, and thereby salts are moved into the small pores, we expect damage in materials only having small pores ($r < 35$ nm). For materials that dry and thereby move crystals towards the small pores, these small pores must be of this size. As long as salts have the possibility to crystallize in pores larger than that, salts will crystallize in these pores without causing damage to the material. For materials not having small enough pores the equilibrium crystallization pressure cannot explain salt induced damage. An example of these kind of materials is fired clay brick.

Experimental work has been performed on series of model porous materials in order to test the derived solubility relations experimentally and will be presented in chapter 6.

3. Nuclear Magnetic Resonance

In this chapter the Nuclear Magnetic Resonance technique is discussed briefly. For a more extensive treatment of NMR various excellent textbooks are available [Abr61], [Sli90], [Vla96].

First, the semi-classical model for NMR is presented in section 3.1. Next, in section 3.2, the quantum mechanical model is used to estimate the consequences of measuring nuclei with a quadrupole moment. The spin-echo technique is explained in section 3.3. Section 3.4 discusses the typical aspects of NMR experiments on fluids in porous materials. Finally, in section 4 the NMR apparatus is discussed.

3.1 Semi classical model of NMR

Most atoms have, besides an angular momentum, also a magnetic moment. If a static magnetic field \vec{B}_0 is applied in the z direction, an isolated magnetic moment will experience a torque, and because the magnetic moment and the angular momentum are coupled, it will precess around \vec{B}_0 with the Larmor frequency (see figure 3.1).

$$\omega_L = \gamma B_0. \quad (3.1)$$

The magnetic moment of one nucleus is called the spin. NMR experiments can only be performed by probing many nuclei together, therefore an ensemble of spins must be discussed. The various spins in an ensemble in a homogeneous magnetic field \vec{B}_0 all precess with the same Larmor frequency, but all with a different phase. The net result of all these spins is a net magnetization \vec{M} in the \vec{B}_0 (z -axis) direction, because all x and y components cancel out.

When a radio frequency (RF) field with the Larmor frequency is applied the motion of the spins will be changed, as will be explained below. A RF field \vec{B}_1 is often applied to the sample by a coil, that is part of a resonant LC circuit. The coil can be used to send the RF signal but is also used to measure the NMR signals generated by the sample. For NMR \vec{B}_1 is applied perpendicular to \vec{B}_0 . What happens when \vec{B}_1 is applied is best described when using a frame rotating with a frequency ω_L around the z -axis. To distinguish between the rotating and normal frame, the rotating frame is denoted by (x',y',z) whereas the normal frame is (x,y,z) . For the normal frame we use d/dt , and for the rotating frame $\partial/\partial t$. For

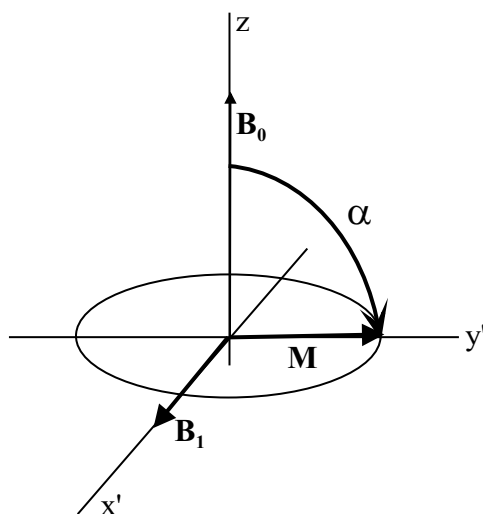


Figure 3.1: When an extra field (B_1) is added along the x' axis in a rotating axes frame, a precession occurs in the $y'z$ plane. The pulse length is chosen such that the flip angle α is 90° .

the magnetization this results in

$$\frac{\partial \vec{M}}{\partial t} = \gamma \vec{M} \times (\vec{B}_0 + \frac{\vec{\omega}}{\gamma}). \quad (3.2)$$

When the system is in equilibrium the magnetization is equal to M_0 and points into the \vec{B}_0 direction. When the RF field with $\omega = \omega_L$ is applied \vec{M} will precess in the rotating frame with a frequency $\vec{\omega}_1 = \gamma \vec{B}_1$. This precession is illustrated in figure 3.1. In the laboratory frame this precession will be a spiral movement of the magnetization along the surface of a sphere.

When starting in the equilibrium situation $\vec{M} = (0,0,M_0)$ and applying the RF field until $\vec{M} = (0,M_0,0)$ at time $t = 0$, the magnetization has been put into the $x'y'$ plane. The system will now return towards the equilibrium situation $(0,0,M_0)$. M_z will grow towards M_0 with a characteristic time T_1 . This process is called spin-lattice relaxation. The value T_1 is called the longitudinal- or spin-lattice relaxation time. During this relaxation process the potential energy of the spins is transferred to the local environment. The components $M_{x'}$ and $M_{y'}$ will disappear with a characteristic time T_2 , the transverse relaxation or spin-spin relaxation time. In this process the spin system will not exchange energy with the environment. The solution of the equation of motion of the spin system outlined above, is given by the so-called Bloch equations:

$$M_x = M_0 e^{-\frac{t}{T_2}} \cos(\omega_L t) \quad (3.3)$$

$$M_y = M_0 e^{-\frac{t}{T_2}} \sin(\omega_L t) \quad (3.4)$$

$$M_z = M_0 [1 - e^{-\frac{t}{T_1}}] \quad (3.5)$$

In NMR experiments $\omega_1 \gg 1/T_{1,2}$ must be satisfied, otherwise the ensemble of spins cannot be considered as one magnetization vector during excitation

3.2 Quantum-mechanical description

The semi-classical model of NMR, in the previous section, is appropriate for many NMR experiments in which nuclei with $I = 1/2$, (e.g. protons) are measured. However, for nuclei which have $I > 1/2$ (e.g., deuterium $I = 1$, sodium $I = 3/2$, chlorine $I = 3/2$) the semi-classical description is insufficient and a quantum-mechanical description is needed.

For nuclei with $I > 1/2$ two interactions are present. First, the Zeeman interaction, which is the interaction between the magnetic dipole moment of the nucleus and the applied magnetic field \vec{B}_0 . Secondly, the interaction between the electric quadrupole moment of the nucleus and the electric field gradient $\nabla \vec{E}$, originating in the non-spherical charge distribution in the nucleus.

The Hamiltonian describing the interaction of a magnetic dipole moment $\vec{\mu}$ with a magnetic field \vec{B} is given by

$$\mathcal{H}_Z = -\vec{\mu} \cdot \vec{B}. \quad (3.6)$$

The magnetic field is applied in the z direction, therefore

$$\mathcal{H}_Z = -\gamma \hbar B_0 I_z. \quad (3.7)$$

For a nucleus with $I = 1/2$, for instance H, the resulting energy levels are:

$$E = -g \mu_N m_I B_0 \quad (3.8)$$

with $m_I = -1/2, 1/2$ the magnetic quantum numbers and g the Landé factor. NMR is associated with transitions between the energy levels of a nucleus, resulting in a transition frequency ($\Delta m_I = \pm 1$)

$$\omega = \omega_L = g \mu_N B_0 / \hbar = g \frac{|e| \hbar}{2m_N} B_0 = \gamma B_0. \quad (3.9)$$

In the absence of electric field gradients, Eq. 3.8 can also be used in the case of $I = 3/2$, for instance ^{23}Na , but now $m_I = -3/2, -1/2, 1/2$ or $3/2$. The resulting energy splitting is the same as in Eq. 3.9. For the case that electric field gradients are present the Hamiltonian describing the interaction of a nucleus with $I > 1/2$ with its environment is given by [Sli90]

$$\mathcal{H} = \mathcal{H}_Z + \mathcal{H}_Q = -\gamma_n \hbar H_0 I_z + \frac{e^2 q Q}{4I(2I-1)} [3I_z^2 - I^2 + \frac{\eta}{2}(I^{+2} + I^{-2})], \quad (3.10)$$

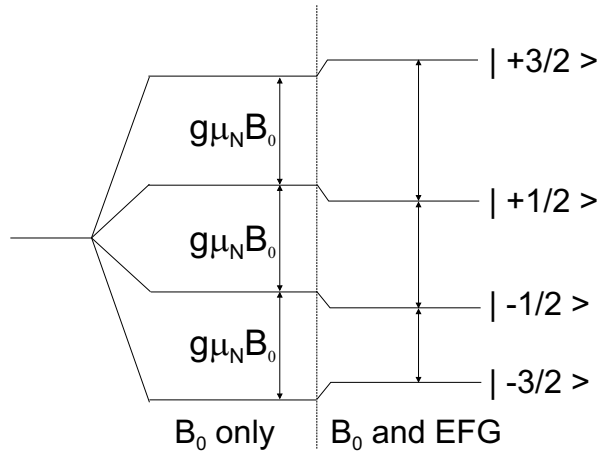


Figure 3.2: *The energy levels of a nucleus with $I = 3/2$ which has a Zeeman and a quadrupole interaction. The NMR frequency is determined by the distance between the energy levels. It can be seen that if no electric field gradient (EFG) is the case one single frequency exists whereas three frequencies exist if an EFG exists.*

with e is the electron charge, q the charge of the nucleus, Q the quadrupole moment of the nucleus, and $\eta = V_{xx} - V_{yy}/V_{zz}$ an asymmetry parameter of the electric field gradient [Sli90]. For Na ions in solution with a magnetic field $B \approx 1$ T, reflecting the experiments described in this thesis, the quadrupole interaction is small compared to the Zeeman interaction (strong field case [Sli90], [Sli90]). In that case the quadrupole interaction can be considered as a perturbation on the Zeeman interaction. The resulting energy levels are given in figure 3.2. Note that the shift caused by the quadrupole perturbation is the same for $|+3/2\rangle$ and $|-3/2\rangle$ and for $|+1/2\rangle$ and $|-1/2\rangle$. Three transition frequencies are possible satisfying the selection rule $\Delta m \pm 1$. If all nuclei would experience the *same* electric field gradient (EFG) the NMR spectrum would therefore consist of three different transition frequencies: the Larmor frequency and two sidebands [Sli90].

Up till now we neglected the fact that during the NMR experiments the ions in the solution are not static but move randomly because of Brownian motion. Loss of magnetization can occur because of motion. Movement of ions can average out the EFG experienced by the ion. Generally two distinct regimes of quadrupolar ions in solution can be distinguished: The *slow* modulation regime and the *fast* modulation regime [Por01]. In the slow modulation regime the ions experience a net EFG which results in an energy level splitting as described above. The magnetization decay cannot be described anymore by a single T_i value. Forty percent of the magnetization decays with a characteristic time constant $T_{i,slow}$ and 60 % with a time constant $T_{i,fast}$. The time $T_{i,slow}$ is caused by the central transition ($m_I = 1/2 \Leftrightarrow -1/2$) whereas $T_{i,fast}$ is caused by the satellite transitions ($m_I = 3/2 \Leftrightarrow 1/2$,

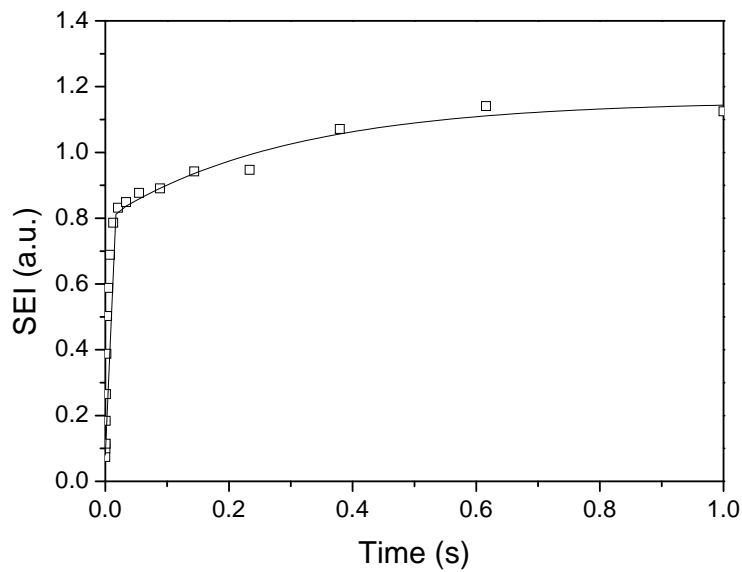


Figure 3.3: An example of a T_1 measurement of Na ions in solution between laponite clay particles, measured at 0.78 T (\square). The laponite clay particles have their counterions in the solution, hence a significant amount of electric field gradients exist which causes the Na ions to be in the slow modulation regime. In this regime the relaxation is bi-exponential. The solid curve represents a fit to the data using $T_{1,f} = 3.6$ ms and $T_{1,s} = 0.3$ s.

and $m_I = -3/2 \leftrightarrow -1/2$). An example of a system in this slow modulation regime is laponite clay as studied by Delville et al. [Por01]. The clay is negatively charged and the counter ions are in the solution between the clay plates. This results in a large electric field gradient, which is not averaged out by the movement of the ions in the case that the clay particles are ordered. An example of a NMR relaxation measurement performed on Na ions inside an ordered laponite clay system is given in figure 3.3.

In the fast modulation regime a quite different behavior is observed. In this regime the movement and the tumbling of the ions is fast compared to the timescale of the NMR experiment and therefore the ions do not feel a net EFG. Therefore no splitting occurs and a mono-exponential relaxation behavior is observed. In chapter 5 various experiments on Na solutions in model pore systems are discussed. When the Na ions are in the fast modulation regime the semi-classical model suffices to describe the experiments.

3.3 Spin-echo technique

We consider an ensemble of spins together creating a macroscopic nuclear magnetization. When starting in the equilibrium situation $\vec{M} = (0,0,M_0)$ and applying the RF field during a certain time, the magnetization can be put in the xy plane ($t = 0$). The RF pulse which moved the magnetization from the z direction over 90° into the xy plane is called a $\pi/2$ pulse or 90° pulse. The magnetization will now precess in the xy plane with the Larmor frequency. In the rotating coordinate frame the orientation of the magnetization is fixed within the xy plane. Due to relaxation the magnetization in the xy plane will vanish. Because often the magnetic field B_0 is not perfectly homogeneous, a distribution of Larmor frequencies exists. The effect is a dephasing of the magnetization components in the xy plane, often faster than the longitudinal and transverse relaxation. The dephasing of the spins has a characteristic time constant T_2^* . The precessing magnetization induces a signal in the RF coil of the tuned LC circuit. The signal that is received just after the 90° pulse is called the *free induction decay* (FID). The FID is often not suitable for measurements because of ringing of the tuned LC circuit and the recovery time of the receiver. After some time the magnetization components have dephased and the magnetization in the xy plane is cancelled out. Then after a time $t = \tau$ a second RF pulse is given, during which all spins are rotated over 180° around \vec{B}_1 . This pulse is called the π or 180° pulse. Now the accumulated phase in the xy plane is reversed. The result is a rephasing of the magnetization components until $t = 2\tau$ immediately followed by a dephasing after $t = 2\tau$. The signal obtained from this rephasing and dephasing is called the *spin echo* and is maximal at $t = 2\tau$, called the echo time (TE).

During all experiments described in this thesis a static magnetic field gradient is applied:

$$B_x = 0, B_y = 0, B_z = B_0 + G_z \cdot z \quad (3.11)$$

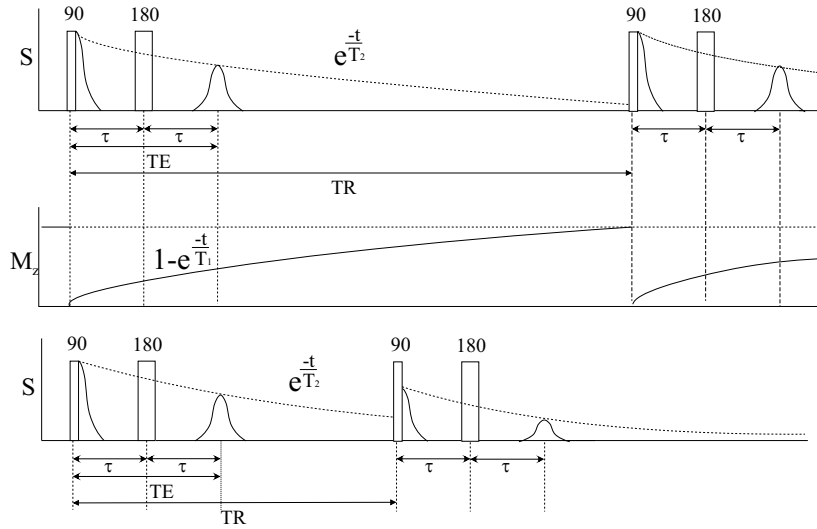


Figure 3.4: The Hahn pulse sequence: A 90° pulse followed by a 180° pulse and a spin echo. The lower graph shows the loss of signal if the criterion $TR \gg T_1$ is not satisfied. For reason of clarity T_1 is chosen almost equal to T_2 .

This static gradient has an important effect: *slice selection*. Because the RF field has a narrow frequency distribution and the Larmor frequency in the sample depends on z (due to the field gradient) only a slice of the sample perpendicular to the z direction is excited by the 90° pulse.

Usually spin-echo signals are very weak and therefore the signals from subsequent spin-echo experiments are averaged to obtain an acceptable signal to noise ratio. If $T_2 \ll T_1$ the signal intensity of the spin echo is given by:

$$S_{echo} \propto \rho [1 - e^{-\frac{TR}{T_1}}] e^{-\frac{TE}{T_2}} \quad (3.12)$$

in which TR is the repetition time of the measurement and ρ the density of the nuclear spins. Figure 3.4 illustrates eq. 3.12. The upper part shows the signal intensity during a $\pi/2 - \pi$ pulse sequence. Just after the $\pi/2$ pulse the magnetization is in the xy plane and the FID is generated. Due to T_2 relaxation the maximum magnetization that can be obtained by rephasing of the spins decreases, as is shown by the decay curve in the upper part of the figure. One should realize that the magnetization loss due to dephasing of the spins is reversible by the rephasing, but the loss of magnetization due to relaxation is not reversible. Meanwhile the magnetization in the z direction is increasing because of the longitudinal relaxation, as is shown in the middle part of the figure. What happens when the repetition time is chosen too short is shown in the lower part of the figure: Not all magnetization has returned to the z direction and therefore the $\pi/2$ pulse will not put the total equilibrium magnetization in the xy plane but only a fraction of it. The result is a

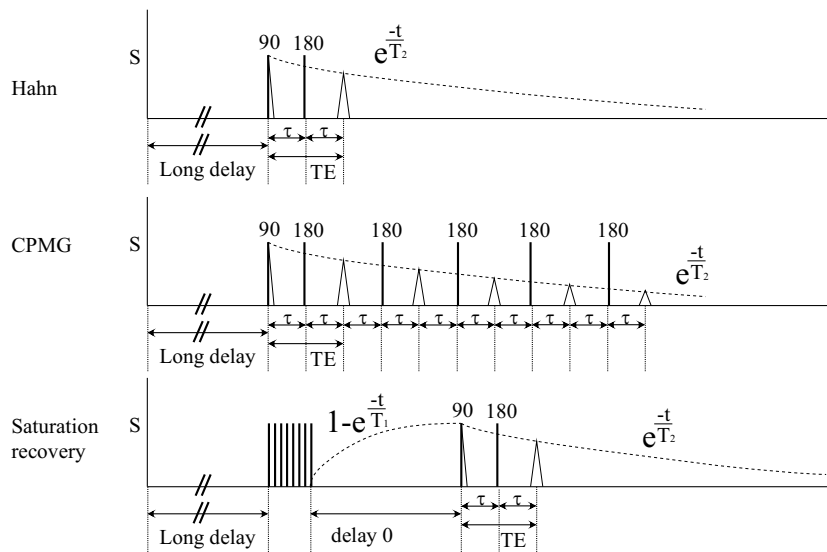


Figure 3.5: *The Hahn sequence, CPMG sequence and saturation recovery sequence. For reason of clarity the value of T_1 is smaller than T_2 in this drawing, which in reality does not occur.*

smaller spin-echo signal than for the first echo. Waiting four times the value of T_1 before starting the next measurement is generally acceptable. This waiting period is called the *long delay*.

3.3.1 Hahn sequence

There exist many pulse sequences leading to spin echoes. The ones used for our measurements are explained here. The most basic sequence is the *Hahn sequence* that has been explained above. It consists of a $\pi/2$ pulse followed by a π pulse and a spin echo signal (see figure 3.5). The Hahn sequence can be used to measure the amount of moisture or sodium in a slice of material. By changing the frequency (*frequency scan*) of the RF field all slices of the sample can be measured and, for instance, a profile is obtained. By moving the sample one can also obtain a moisture or salt profile (*height scan*).

Because the Hahn sequence can determine the amount of H or Na, the salt concentration can be obtained by dividing these signals. If in addition also a sample with a known concentration is measured, the measurement is calibrated and a quantitative concentration is obtained. In the next chapter typical numbers for these measurements will be shown.

3.3.2 Carr-Purcell-Meiboom-Gill sequence

The *Carr-Purcell-Meiboom-Gill sequence* (CPMG) consists of a $\pi/2$ pulse placing the magnetization in the xy plane, followed by many π pulses, each reversing the direction of the spins in the xy plane. After the first spin echo the magnetization components are again dephasing; a subsequent π pulse reverses the accumulated phase and therefore a second spin echo can be obtained. This is repeated several times (N_{CPMG}). The time between the π pulses is called the echo time. As can be seen in figure 3.5, the CPMG sequence will probe the transverse relaxation behavior and is therefore a possible pulse sequence to measure T_2 .

As was mentioned in section 3.2 the nuclei in a liquid move randomly because of Brownian motion. By moving through a static magnetic field gradient phase is accumulated. In a CPMG sequence the phase, accumulated by motion, can be largely be compensated. This is necessary to measure the exact T_2 instead of a mixture of relaxation and dephasing. A CPMG sequence is free of dephasing when the measured T_2 stays the same while changing the echo time or the static gradient. In that case the signal decay is given by:

$$S(t) = S(0)e^{-t/T_2}. \quad (3.13)$$

The magnetization decay can also be measured with a series of Hahn sequences with varying echo time. In this case the decay contains the relaxation and the dephasing caused by movement, described by [Hah50]:

$$S(t) = S(0)e^{-t/T_2}e^{-\left(\frac{1}{12}D_0\gamma^2G^2t^3\right)} \quad (3.14)$$

where γ is the gyromagnetic ratio, G the magnetic field gradient and D_0 the diffusion coefficient. Eq. 3.14 only holds for free diffusion, in the next section restricted diffusion will be discussed.

3.3.3 Saturation recovery

Another pulse sequence is the saturation recovery sequence, which starts with a so called "comb" of random RF pulses. The result of these random pulses is that the net magnetization of the sample is completely destroyed. After the comb the magnetization will return to equilibrium with time constant T_1 because of the longitudinal relaxation. After a certain time (delay Δ in figure 3.5) a Hahn sequence is given. By varying the value of the time interval delay Δ the longitudinal relaxation behavior can be measured, from which T_1 can be obtained. An alternative sequence to measure T_1 is the inversion recovery sequence, in which the comb of random pulses is replaced by a single π pulse. An advantage of using saturation recovery instead of inversion recovery is that the first is significantly less sensitive to errors in the π pulse length.

3.4 NMR and porous materials

When performing NMR measurements on a fluid in a porous material some interesting phenomena occur. For instance, the relaxation time of the nuclei probed by NMR can depend upon the size of the pore in which the fluid is present. This *pore relaxation* can be used as a method for obtaining the pore size distribution of a sample. In the remainder of this chapter the discussion focusses on ^1H NMR. In the next chapter it will be discussed whether or not a similar behavior holds for Na ions.

3.4.1 Pore relaxation behavior

Brownstein and Tarr [Bro79] created a model describing the time evolution of the magnetization of the nuclear spins of a fluid in the pores of a porous material. Experimentally one measures a signal proportional to the total nuclear magnetization of the fluid. This total magnetization is modelled as the sum of all local magnetizations in the sample volume:

$$M(t) = \int_V m(\vec{r}, t) d\tau \quad (3.15)$$

in which m is the local magnetization per unit volume. This magnetization (for instance the magnetization in the xy plane) can decay due to *volume-like sinks* (γ) or *surface-like sinks* (μ). The physical nature of the bulk sink is not discussed by Brownstein and Tarr, but they hypothesize bound water and magnetic impurities such as macromolecules. Two factors are assumed to govern the properties of the system, namely paramagnetic impurities in the pore wall acting as relaxation centers and classical self-diffusion of the water molecules. The equations for the system described above are:

$$\vec{\nabla} \cdot (\vec{D} \cdot \vec{\nabla} m) - \gamma m = \frac{\partial m}{\partial t} \quad (3.16)$$

$$(\vec{n} \cdot \vec{D} \cdot \vec{\nabla} m + \mu m) |_{s=0} = 0 \quad (3.17)$$

$$m(\vec{r}, 0) = \frac{M(0)}{V} \quad (3.18)$$

where \vec{D} is the diffusivity tensor. Equation 3.16 is a diffusion equation containing a volume-like sink, Eq. 3.17 is the boundary condition containing a surface-like sink, and Eq. 3.18 is the initial condition assuming a uniform magnetization of the sample. The solution of this diffusion problem can be expressed as a sum of normal modes $F_n(\vec{r})$ with weight A_n :

$$m(\vec{r}, t) = \sum_{n=0}^{\infty} A_n F_n(\vec{r}) e^{-t/T'_n} \quad (3.19)$$

This solution results in a number of eigenvalues T'_n ($T'_0 > T'_1 \geq T'_2 \dots$) in which n refers to the mode number. The normal mode corresponding to T'_0 is always non

degenerate. Brownstein and Tarr show that this equation can be solved for several geometries under some assumptions. They assume that there are no volume-like sinks, that the diffusivity is isotropic, $\vec{D} = D\vec{I}$, and that the surface-like sink is constant ($\mu = \text{const}$), characterized by a surface relaxivity ρ_i [m/s] (ρ_2 for transverse surface relaxivity) over an active surface S.

Certain conclusions can be drawn concerning the general behavior of this system. For the discussion we focus on the transverse relaxation time T_2 , but the same also applies for the longitudinal relaxation time T_1 . The decay time T'_n is determined by a dimensionless eigenvalue, which depends upon the dimensionless parameter $\rho_2 a/D$, in which a is the characteristic pore size. Three regions can be distinguished:

- $\rho_2 a/D \ll 1$: the fast diffusion region. In this region the lowest mode in the eigenvalue problem dominates the behavior. The decay times for the higher modes are an order of magnitude smaller.
- $1 \ll \rho_2 a/D \ll 10$: the intermediate diffusion region, in which the lowest mode dominates but the higher modes contribute a few percent.
- $10 \ll \rho_2 a/D$: the slow diffusion region. The higher modes contribute a few tens of percents.

The fast diffusion region will very likely be the region of interest in the context of this work, at least for H [Val01b]. The validity of the Brownstein and Tarr relaxation model for Na is not clear; this point will be discussed in the next chapter. Brownstein and Tarr show that in the fast diffusion region under the assumptions mentioned above, the eigenvalue of the lowest mode T'_0 is dominant and given by $T'_0 = V/\rho_i S$, where V is the pore volume and S is the active surface area.

An extension of the model was reported by Halperin et al. [Hal89]. They consider the case in which the volume-like sinks cannot be neglected. The overall relaxation is now a weighted sum of the surface relaxation and the bulk relaxation. The surface relaxation rate T_{surf}^{-1} is a characteristic of molecules in a layer of thickness λ near the solid surface (figure 3.6), and a surface interaction parameter is defined as:

$$\rho \equiv \frac{\lambda}{T_{surf}} \quad (3.20)$$

which is in fact the surface relaxivity defined above. The molecules in the inner part of the pore will behave like bulk until they reach the layer near the pore wall by diffusion. At that time both bulk and surface relaxation occur. These two effects influence the overall relaxation of the system: the bulk relaxation (characterized by $1/T_{bulk}$) in the entire pore volume and the surface relaxation (characterized by ρ) in a volume λS . In the fast diffusion region the measured relaxation rate is given by the weighted sum:

$$\frac{1}{T_{meas}} = \frac{1}{T_{bulk}} + \frac{\lambda S}{V} \frac{1}{T_{surf}} = \frac{1}{T_{bulk}} + \frac{S}{V} \rho_i \quad (3.21)$$

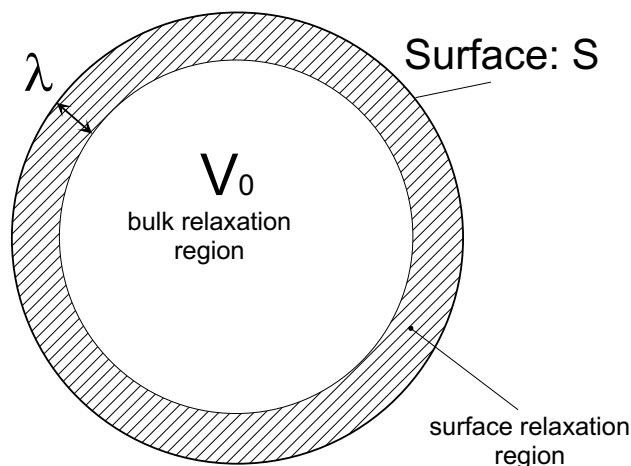


Figure 3.6: *Schematic of a spherical pore filled with water. A layer of thickness λ of molecules will behave according to the surface relaxation. All other molecules will behave according to the bulk relaxation.*

For water the bulk relaxation time is often very long compared to the pore relaxation time. Therefore usually the first term at the right hand side of Eq. 3.21 is neglected. In that case the relaxation time (either transverse or longitudinal) is described by:

$$T_i = V/\rho_i S \quad (3.22)$$

in which $\rho_{i,H}$ is the transverse ($i = 2$) or longitudinal ($i = 1$) surface relaxivity. These relaxivities depend on the fluid and the porous material. The relaxation time depends upon the volume to surface ratio, which is different for each pore size. Assuming spherical pores $V/S = r/3$, in which r is the pore radius. For cylindrical pores this V/S value is $r/2$. Important to notice is that the value of V/S reflects the pore geometry and scales linearly with the pore size. The transverse relaxation time of H as a function of the pore size (neglecting the bulk term and assuming spherical pores) is given by:

$$T_2 = \frac{V}{S\rho_{2,H}} = \frac{r}{3\rho_{2,H}}. \quad (3.23)$$

3.4.2 Pore size distribution from relaxation measurements

In general a porous material will have a certain pore-size distribution. Each pore size contributes to the total signal intensity with its own (transverse) relaxation time:

$$M(t) = \sum_i M_i \cdot e^{-t/T_{2,i}} \quad (3.24)$$

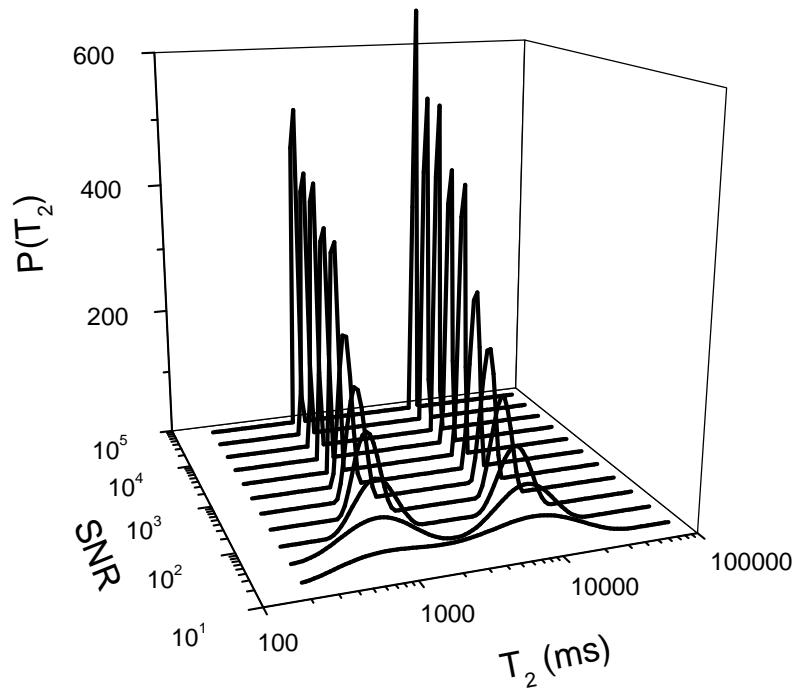


Figure 3.7: Plot of the T_2 distribution determined by CONTIN as a function of the signal to noise ratio (SNR) for the first echo, in a bi-exponential decay curve with relaxation times 1000 and 10000 ms. At infinite SNR the distribution shows two delta peaks, whereas at lower SNR the peaks become wider. Therefore, in the presence of noise, a pore size distribution based on a CONTIN analysis might be broader than it actually is.

in which $T_{2,i}$ is the transverse relaxation time of the i -th pore size and M_i the intensity of the signal corresponding to the i -th pore size (the volume of the pores with this pore size).

If a continuous pore size distribution is assumed, the summation over all pores changes into an integral:

$$M(t) = M_0 \int P(T_2) e^{-t/T_2} d(T_2). \quad (3.25)$$

This equation is related to the Laplace transform of the probability distribution $P(T_2)$ of the relaxation times. Therefore the distribution of T_2 can be calculated from the inverse Laplace transform of $M(t)/M_0$. Because the relation between the pore size and the relaxation time is known (eq. 3.23), the pore size distribution can be obtained. The inverse Laplace transformation is often done numerically with the CONTIN [Pro82] program. Although this program is very commonly used, the results are very sensitive to noise in the measurement. This is illustrated by figure 3.7, in which the same double exponential decay curve is analyzed for various signal to noise ratios of the first spin echo in the decay curve. It can be seen that an increase of the noise results in a wider pore size distribution. This is a consequence of the regularization procedure used in the program [Pro82]. This behavior must be kept in mind when interpreting experimental data.

3.5 Summary

NMR can be used to obtain the moisture and salt content inside a porous material non destructively. By acquiring a H and a Na Hahn sequence and dividing the signal intensities a quantitative concentration measurement can be made. Typical numbers for these measurements are given in the next chapter. Besides this NMR also provides, by means of NMR relaxation (relaxometry), the pore size distribution of the sample.

4. NMR Scanner

4.1 Introduction



Figure 4.1: *The NMR apparatus used in most of the experiments described in this thesis.*

The NMR scanner used for the experiments described in this thesis has to meet certain requirements. In section 4.2 these are discussed, together with solutions chosen to meet them. In section 4.3 typical experiments and parameter values are given to illustrate the application of NMR for studies on porous materials.

4.2 Setup

The NMR scanner used in our experiments is a home built 0.78 T scanner. A photo of this scanner is given in figure 4.1. The field of 0.78 T was chosen as a compromise between the signal-to-noise ratio, which increases with increasing field, and the line broadening due to the presence of magnetic impurities, which lead to a decrease in resolution at higher magnetic fields. The magnet is a conventional water-cooled electro magnet. The pole tips of this magnet have a diameter of 20 cm and are 5 cm apart. The magnetic field has a stability better than 5×10^{-5} T/week and a homogeneity of 4×10^{-5} T over 1 cm diameter spherical volume.

A magnetic field gradient is generated in the vertical direction by a set of conventional Anderson coils [And61]. The coils provide a field gradient which is constant within 1 % over 30 mm in the vertical direction. Gradient strengths of 0.3 T/m can be applied.

Quantitative measurements

In our experiments cylindrical samples are used which can be inserted in a cylindrical coil with an inner diameter of 35 mm, made of 7 turns of 1 mm Cu wire. The coil is part of a tuned LC circuit and is placed within a shielded box. Because we want to perform quantitative measurements of the moisture and sodium content, the LC circuit is carefully matched to the characteristic impedance of the equipment (50 Ω), whereas changes in the tuning of the circuit should be as small as possible. To reduce the effect of variations of the dielectric permittivity of the sample, which will change the tuning, a cylindrical Faraday shield has been placed between the coil and the sample. This shield consists of 0.5 mm insulated Cu wires running parallel to the axial direction of the coil. The wires are electrically interconnected and grounded at the lower side of the shield. A small slit in this part of the shield prevents the generation of eddy currents and corresponding RF power losses.

The coil is part of a series tuned circuit, shown in figure 4.2. The same circuit is used for both sending the pulses and receiving the spin echoes. The scanner is operated at a frequency of 33 MHz for H and 8 MHz for Na. The tuning is changed by adding or removing a capacitor by means of a switch, that is actuated by a stepper motor. This can be done automatically during an experiment, which facilitates quasi-simultaneous measurements of H and Na.

Because the measurements are quantitative the amount of signal is proportional to the amount of nuclei probed, hence dividing the sodium signal by the water signal gives a direct measure for the concentration. If also a reference sample is measured the measurement is calibrated and the actual concentrations can be determined.

Temperature control

Because for many experiments described in this thesis temperature is an essential parameter, the temperature of the sample holder must be controlled accurately.

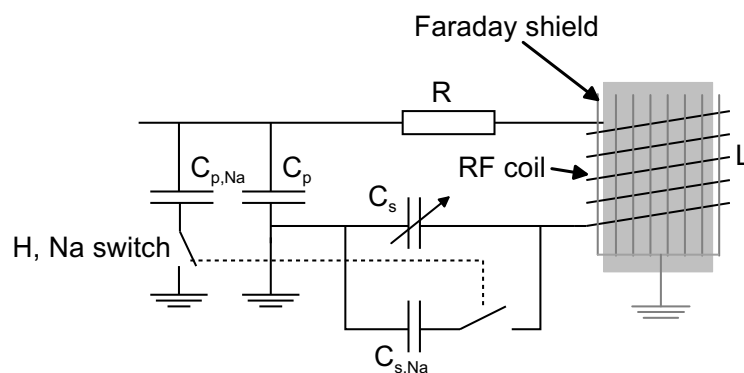


Figure 4.2: *Schematic of the radio frequency circuit used for quasi-simultaneous H-NMR and Na-NMR measurements. To obtain quantitative results, a Faraday shield is used. This circuit is used for both the sending of the pulses and the receiving of the spin echoes.*

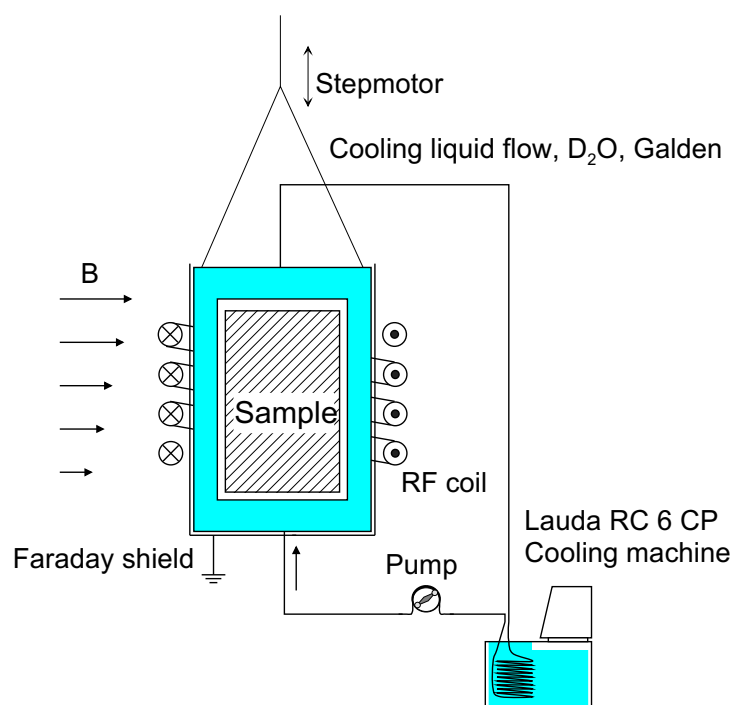


Figure 4.3: *Schematic overview of the central part of the NMR scanner. For a detailed explanation see the text.*

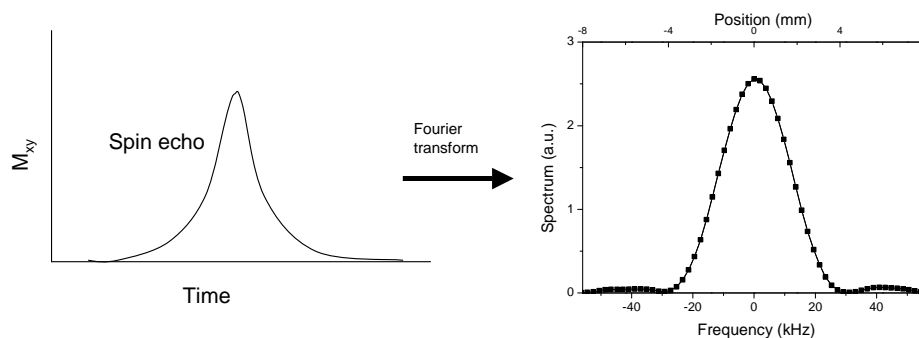


Figure 4.4: *Once the spin echo is Fourier transformed a profile of water in the sample is obtained. The profile given is of a water sample measured by a Hahn spin echo sequence in a static magnetic field gradient of 0.16 T/m. The envelope the profile has its origin in the hard RF pulses. The spatial resolution is the distance between two adjacent Fourier components.*

This is achieved by flowing a cooling liquid through the wall of the sample holder. Because quantitative NMR measurements have to be performed, the cooling liquid has to meet various requirements. First of all, it should not produce any signal in our NMR experiments, which means that it cannot contain H or Na to a very high degree of purity ($< 0.1\%$). Second, it should not have a high electrical conductivity, since in that case it would shield the alternating RF magnetic fields. Finally, the cooling liquid should not chemically react with the PVC sample holder or the tubes used. Two cooling liquids have been found suitable: D_2O , which can be used above $4\text{ }^\circ\text{C}$, and Galden¹, which can be used above $-30\text{ }^\circ\text{C}$. In most of the experiments Galden HT70 was used. Galden is a fluorinated fluid containing carbon, oxygen, and fluor. It is especially designed as a cooling liquid, and therefore very suitable for this application. Because this cooling liquid easily evaporates and is rather expensive a separate closed cooling circuit is used for the sample cooling. The cooling liquid is pumped by a peristaltic pump to prevent pollution of the coolant. A Lauda RC6CP temperature bath is used to control the temperature of a copper spiral through which the coolant flows. A schematic overview of the central part of the scanner is given in figure 4.3.

Data acquisition and control

The NMR scanner is controlled by a PhyDAS system, which is a home built data acquisition system based on a VME MPS030 processor. The system contains two buses, the VME bus and the PhyBUS. The latter contains all the interfaces needed

¹Galden PFPE is a registered trademark of Solvay Solexis, <http://www.solvaysolexis.com>

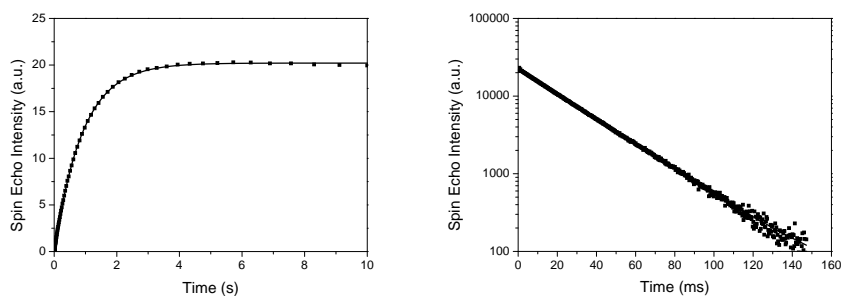


Figure 4.5: *Typical examples of a hydrogen T_1 measurement (left) by a saturation recovery sequence and a hydrogen T_2 measurement (right) by means of a CPMG sequence.*

for the experiment. The MPS030 computer can be programmed using the EPEP real-time interpreter. Communication with the scanner is done by a PC via a RS232 line. The PC is also used to save the data. Apart from the NMR hardware itself also the temperature, the tuning of the LC circuit to H or Na, and the position of the sample are controlled by the computer. Because of this, the scanner can be operational 24 hours a day, which enables us to perform experiments continuously.

4.3 Typical parameters and examples

Typical values for parameters used in the NMR experiments are given in table 4.1. The RF pulses are created by switching the RF carrier frequency on and off within 100 ns. The resulting RF pulses are called hard pulses. The frequency content of such pulses is a sinc function. After the pulses have been sent, the RF circuit is used to sample the spin echo. After the spin echo has been Fourier transformed a profile as shown in figure 4.4 is obtained. In this figure the lower x-axis shows the frequency, whereas the upper x-axis shows the corresponding position. It is important to notice that the data obtained from sampling one spin echo contain spatial information. The best sensitivity is obtained around the central frequency component (frequency 0 in figure 4.4). This is because the pulses do not exactly match the flip-angle condition over the entire slice. For this reason we used a saturation recovery sequence to determine the relaxation rate T_1 instead of an inversion recovery sequence. The latter sequence would not flip the magnetization correctly over the entire slice and hence not the correct relaxation time would be measured. It also explains our choice to use CPMG for T_2 measurements, since this sequence can correct for errors in the π pulse width using a suitable RF phase cycling scheme [Hur01]. Two typical examples of relaxation time measurements are given in figure 4.5.

One-dimensional profiles of the H and Na contents within a slice of the sample are obtained by a Hahn sequence and sampling the spin echo. Each H spin echo

	Hydrogen	Sodium
isotope	^1H	^{23}Na
$\pi/2$ pulse	15 μs	20 μs
π pulse	30 μs	40 μs
t_e	285 μs	800 μs
averages	2×50	2×2048
long delay	10 s	0.2 s
f	33.8 MHz	8.9 MHz
gradient	0.16 T/m (7000 Hz/mm)	0.18 T/m (2116 Hz/mm)
window width	256 μs	512 μs
spatial resolution	0.55 mm	0.92 mm
sensitivity	1	0.09

Table 4.1: *Typical numbers for the NMR experiments presented in this thesis.*

is Fourier transformed and the seven central components of the discrete Fourier transform are taken used to create a profile of the H within the selected slice. The distance between two adjacent Fourier components is determined by the sampling window. For H this window is 265 μs , which results in a frequency resolution of 3.9 kHz. Before performing the Fourier transform the window is enlarged to 512 μs by zero padding. This is done because the fast Fourier transform routine expects an array of 512 values. After this padding the distance between two adjacent Fourier components is 1.9 kHz. Combining this with the gradient strength (7000 Hz/mm) this results in a spatial distance of 0.27 mm; 7 components therefore cover 1.9 mm of the sample. For Na the spatial distance between two Fourier components is 0.92 mm. The central three components are used, which cover 2.8 mm. The sequences are averaged to improve the signal to noise ratio, and between them the spin system has to return to equilibrium therefore a time, called the long delay, is waited before repeating the sequence. Measurement of one H and one Na slice takes approximately half an hour. Once these profiles are measured the sample is moved towards a new position and a H and Na profile of the next slice are measured. This procedure is repeated until the end of the sample is reached, after which the profiles of the individual slices are combined to overall H and Na profiles.

A typical example of a profile obtained this way is given in figure 4.6, in which a stack of samples can be seen. For this profile 30 slices were measured which results in a total measurement time of 15 hours. Typical measurement times for such profiles are between 8 and 16 hours depending on the size of the sample. In all experiments a sample containing 3 molal NaCl solution is measured as a reference, which is used to correct for slow variations of the sensitivity of the NMR equipment. The integrals of the H and Na profiles are determined for each sample. From the ratio of Na/H of the 3 molal sample the concentration in the other samples can be determined. Summarizing, the NMR scanner is able to measure the Na concentration inside porous material quantitatively and under temperature controlled conditions.

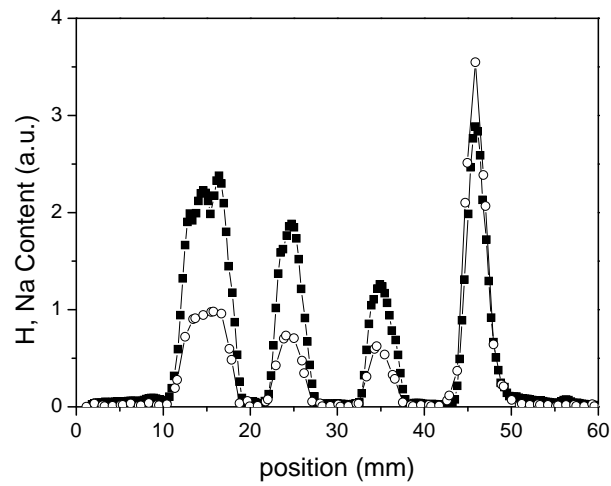


Figure 4.6: *Typical example of a stack of samples in which the H (■) and Na (○) content is measured. The profile is constructed from 30 H and Na spin echoes, which results in 30×7 data points for H and 30×3 data points for Na.*

5. Sodium NMR relaxation in porous materials

abstract¹

The NMR relaxation of hydrogen nuclei of a fluid in a porous material is generally interpreted in terms of the Brownstein and Tarr model, in which the relaxation rate of the signal is inversely proportional to the pore size. We have investigated whether this model can be applied to the relaxation of Na nuclei in a NaCl solution in a porous material. The results indicate that the ion distribution over the pores can be obtained from an analysis of the Na NMR signal decay, if the pore sizes are roughly below 1 μm . This information is very useful for studies of combined moisture and ion transport in porous building materials.

5.1 Introduction

Dissolved salts in porous building materials crystallize while drying. Generally this occurs at the surface, causing defacing, or just beneath the surface, where it may cause structural damage. In addition, salts promote corrosion of the reinforcement in concrete. A detailed knowledge of the moisture and salt transport is essential for understanding these deterioration processes. Some of the issues, which still have to be studied experimentally and theoretically, are the chemical and physical interactions of ions with the material, the possible supersaturation of ions in a pore system, and the growth of crystals in pores [Sch99], [Fla02a], [Pel02]. Knowledge of the location of the ions, either in large pores or in small pores, might be essential. Nuclear Magnetic Resonance (NMR) could be a useful tool for obtaining this information.

It is known that the NMR relaxation of hydrogen nuclei can be used to determine the distribution of water over the various pore sizes. According to the Brownstein and Tarr model [Bro79], the relaxation time of water depends upon the size of the pore in which it is present. The relaxation time is inversely proportional to the surface to volume ratio S/V and therefore directly proportional to the pore radius [Bro79], [Val01c], [Bar03].

¹This chapter has been published in Journ. Magn. Res. **167** 25-30 (2004).

The relaxation behavior of sodium is more complex, because it has a quadrupole moment ($I = 3/2$) This can result in quadrupolar splitting. An example of this effect is studied by Delville et al. [Por01]. When a clay suspension is isotropic, no quadrupolar splitting is observed, whereas splitting is observed when the clay particles are ordered.

The central question of this chapter is whether or not the Brownstein and Tarr model can be applied to dissolved sodium ions in salt solutions confined in porous media. First, the Brownstein and Tarr model is discussed. Special attention is given to the extra demands needed for the model to be applicable to sodium relaxation. Secondly, we discuss relaxation measurements in bulk solutions and in model porous materials. The dependencies of the relaxation time on the sodium concentration and the pore radius are investigated. Furthermore, the applicability of the model to porous building materials is discussed. Results for typical building materials, like mortar and calcium silicate brick, are presented. We end this chapter with some conclusions.

5.2 Relaxation model

Because of the Brownian motion of water molecules, the relaxation of a ^1H -NMR signal contains information on the size of the pore, which was proposed by Brownstein and Tarr [Bro79]. Three relaxation regimes can be distinguished. For our purpose the so-called *fast diffusion regime* is of interest. In this regime the rate limiting step in the magnetization decay is the relaxation at the pore surface. The relaxation rate is then given by:

$$\frac{1}{T_i} = \frac{1}{T_{i,b}} + \frac{S}{V}\rho_i, \quad (5.1)$$

where $i = 1$ or 2 , $T_{i,b}$ is the bulk relaxation time, S and V are the surface area and volume of a pore, respectively, and ρ is the surface relaxivity. Brownstein and Tarr did not consider the physical nature of the relaxation sources, they considered them as sinks of nuclear magnetization. A possible source of relaxation is the presence of magnetic impurities along the pore wall, which is often the case in building materials [Val02a], [Bar03]. This model has proven to be widely applicable [Val01c], [Hal89], [Yeh95].

In principle one might also apply the model to dissolved ions, as these also move by Brownian motion and therefore probe the pore space in a similar fashion as the water molecules. The Na ion diffusivity in a NaCl solution equals $1.3 \times 10^{-9} \text{ m}^2/\text{s}$ for a diluted solution [Lid98] at 25°C , which is comparable to the self-diffusion of H_2O ($2.3 \times 10^{-9} \text{ m}^2/\text{s}$). So even the time scales for diffusion are of the same order of magnitude.

A complication could be that the Na ions have two regimes of relaxation: the fast modulation regime and the slow modulation regime. In the latter, the magnetization decay is bi-exponential because the central transition and the satellite transitions have different relaxation rates (common notation $1/T_{2,s}$ and $1/T_{2,f}$). The magnetization sink assumption is then inadequate. In order to be able to apply the Brownstein

and Tarr model to sodium, the system must be in the fast modulation regime, i.e., the Electric Field Gradients (EFG) experienced by the ion should be uncorrelated while it is probing the pore on its diffusion path.

In the case of water the bulk relaxation is commonly neglected, since it is slow (of the order of 3 s) compared to the surface relaxation. For Na ions, however, this assumption does not hold. It is argued by, among others, Woessner [Woe01] and Eisenstadt et al. [Eis66], that the fast relaxation of Na ions in the bulk is caused by quadrupolar interactions, whereas for water dipolar interactions are mainly responsible for the relaxation process. In essence, the bulk relaxation of Na ions is driven by electric field gradients (EFG). Woessner concludes that the relevant EFG for the bulk Na ions is the EFG caused by the surrounding hydration water molecules. Therefore, the relaxation rate might vary with concentration change, which alters the number of surrounding water molecules, or temperature variations, which change the overall density of the solution. Here only the concentration dependence is discussed.

In applying equation (1) to Na, one should bear in mind that $T_{i,b}$ has a concentration dependence, which is likely to show up in the relaxation time for solution in pores. The surface relaxivity $\rho(C)$ may also vary with the concentration. The following equation describes the sodium relaxation:

$$\frac{1}{T_i(C)} = \frac{1}{T_{i,b}(C)} + \frac{S}{V}\rho(C), \quad (5.2)$$

where C is the concentration of the NaCl solution. By applying this relation to sodium, two basic assumptions are made. First of all, it is assumed that the ions are in the fast modulation regime, which means that the EFG felt by the ions is uncorrelated. This assumption also assures that there is no quadrupole splitting since the nuclei do not experience a net EFG. The criterion for this regime is $\omega_0 a^2/D \ll 1$ in which D is the diffusion coefficient and a the typical distance the ion has to travel to uncorrelate the EFG. Note that this is not necessarily the pore diameter; it also depends on the morphology of the pore surface. Second, the observed relaxation decays are assumed to be mono-exponential, which means that in the pore fast exchange occurs between the surface layer and the bulk. This is only the case when the time needed to probe the pore is much smaller than the time of the experiment ($\sim T_{i,b}$). The time needed to probe the pore is given by $t_D \approx r^2/6D$, where r is the pore radius and D the diffusion coefficient. For a pore of 100 nm, $t_D = 1.3 \mu\text{s}$, which is much smaller than the usual values of the relaxation time (order of 40 ms). We will discuss the validity of these assumptions in the next section.

5.3 Relaxation measurements

5.3.1 Solution

To verify the validity of Eq. 5.2, first information on the bulk relaxation is needed. Both longitudinal (T_1) and transverse (T_2) relaxation times have been determined

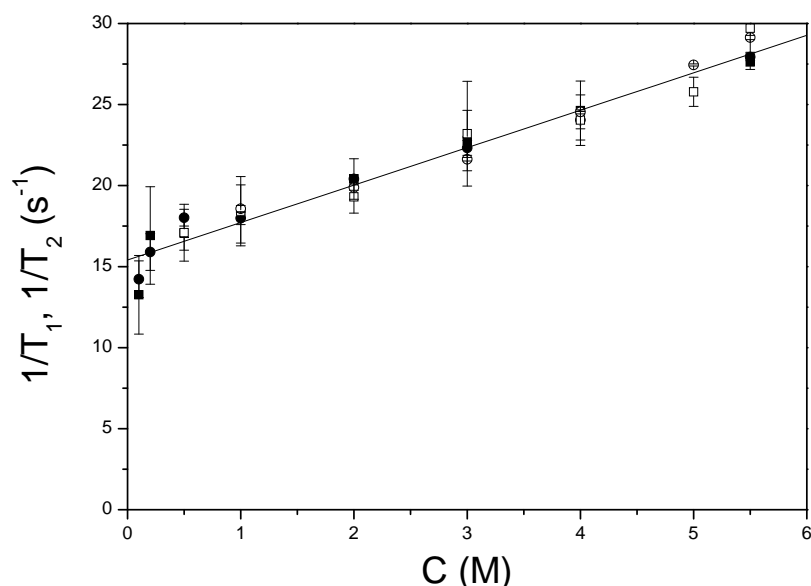


Figure 5.1: *The transverse and longitudinal relaxation rates of sodium in NaCl solutions at 4.7 T (T_1 ■, T_2 ●) and 0.78 T (T_1 □, T_2 ○) as a function of the concentration. The line represents a least squares fit to the data.*

for several NaCl concentrations at two magnetic fields: 0.78 T and 4.7 T. The T_1 measurements are performed by a saturation recovery sequence, which starts with a train of random pulses, of average flip angle 75° , thereby completely destroying the magnetization. This pulse train is followed by a $[\frac{\pi}{2} - \pi - \text{acquisition}]$ Hahn sequence. By increasing the delay between the pulse train and the Hahn sequence the longitudinal relaxation can be probed. Fifteen logarithmically spaced delays are used. The saturation recovery sequence is used because it is insensitive to inhomogeneities in the B_1 field. Because our samples are large compared to the selected slice this sequence yields more accurate results than of the more frequently used inversion recovery sequence. The T_2 was obtained from a Carr-Purcell-Meiboom-Gill (CPMG) sequence, being $(\pi/2)_x[-\pi_y - \text{acquisition}]^n$. Both sequences are applied using a constant magnetic field gradient. In the case of the CPMG sequence, care was taken that the measured signal decay was not affected by diffusion in the applied field gradient. This was checked by varying the inter pulse spacing and the gradient strength. The 4.7 T apparatus is home made with a superconducting magnet (20 cm vertical bore) from Oxford Instruments and equipped with a gradient coil from Doty Scientific (10 cm bore). The Na resonance occurs at 52 MHz. The 0.78 T apparatus consists of an iron-cored electromagnet and is equipped with an Anderson gradient coil set. This scanner is described in detail in [Kop94]. The Na resonance occurs at 9 MHz. The sample temperature during these measurements was $(22 \pm 2)^\circ\text{C}$. Both the T_1 and the T_2 measurements of the NaCl solution show single exponential relaxation and $T_1 \approx T_2$. This is in agreement with the measurements and the theory

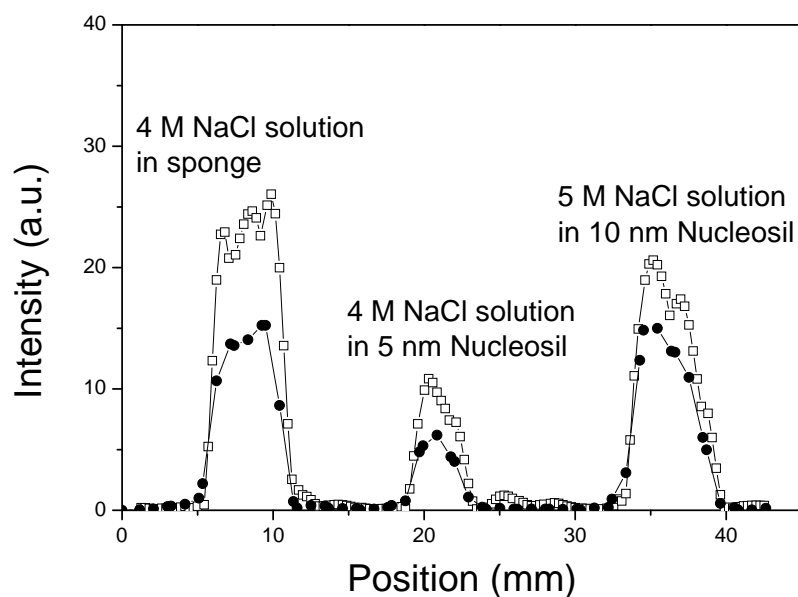


Figure 5.2: *The measured profiles of H (\square) and Na (\bullet) of three different samples.*

of Woessner [Woe01], corresponding to the extreme narrowing limit. The obtained relaxation rates $1/T_i$ are presented in figure 5.1. The observed relaxation rate is independent of the magnetic field strength but reveals a pronounced concentration dependence:

$$1/T_i = (15.4 \pm 0.9)[s^{-1}] + (2.3 \pm 0.3)[s^{-1}M^{-1}] * C. \quad (5.3)$$

The results are in agreement with those found by Woessner [Woe01] and Eisenstadt [Eis66] within experimental accuracy.

5.3.2 Porous material

Knowing the bulk relaxation times, and their dependence on the concentration, the relaxation times in porous materials can be studied. A dried silica gel was used as model porous material. The silica gel used was Nucleosil in six pore sizes: 5, 10, 12, 30, 50, and 100 nm. These pore sizes are the nominal values given by the manufacturer. The actual pore size can differ [Val02], which will be discussed later. A dry sample of Nucleosil was analyzed by NMR MAS spectroscopy at 11.7 T (Bruker AVANCE DMX-500) and revealed no sodium.

As mentioned above, sodium ions have a quadrupole moment ($I = 3/2$). Therefore the energy levels can be shifted due to the presence of electric field gradients [Sli90], resulting in a characteristic pattern in, for instance, a powder spectrum [Ken97]. If such a powder spectrum covers a wide range of frequencies, not all ions are excited simultaneously. In order to be sure that all ions are excited in the NMR

relaxation experiments, pulses should be used that excite the entire spectrum. To obtain information on this spectrum a series of samples, saturated with a NaCl solution, were analyzed in the 11.7 T Bruker spectrometer. For bulk solution, a single peak was observed, because the ions can tumble freely and by doing so any EFG is averaged out. The linewidth is 0.27 ppm. Also the spectrum of the NaCl solution in a Nucleosil sample revealed one peak with a linewidth of 0.86 ppm. This either means that the signal of the satellite transitions coincides with that of the central transition, because the net EFG is averaged out by ion motion, or that the satellite transitions in the spectrum may be broadened beyond detection. In the latter case, a loss of integrated signal intensity would occur. This hypothesis has been tested by measuring a NMR profile of both H and Na of a set of known samples. The profiles are presented in figure 5.2. Three samples are stacked in the 0.78 T apparatus, which has a tuned LC circuit with a Faraday shield to enable quantitative measurements [Kop94]. The first sample consists of 1.136 g 4.0 M NaCl solution in sponge. The sponge is used to suppress eddy currents which are likely to be induced in a conducting sample. The second sample is 0.316 g 4.0 M NaCl solution in Nucleosil with a pore size of 5 nm. The third sample is 0.9958 g 5.0 M NaCl solution in Nucleosil with a pore size of 10 nm. The areas under the profiles were compared with each other. The calculated ratio of the areas Na/H is 0.587, 0.607, and 0.761 for the three samples, respectively. The first two should be the same, which they are within 3 %. If we take the bulk sample as a reference, the 5 M NaCl sample Na/H area ratio should be 0.734, which it is within 4 %. If the satellite peaks in the spectrum would not contribute to the observed Na profiles, a signal loss of about 60 % would occur in the Nucleosil samples [Woe01]. We conclude that the ions in the solution, confined within the pores, have no quadrupole splitting and no signal loss occurs. Hence absolute concentration measurements are possible. We wish to note again that all relaxation measurements presented here reveal mono-exponential behavior. At this point both assumptions underlying Eq. 5.2, fast modulation and mono-exponential relaxation, have been verified.

Next, we focus on the actual relaxation behavior of Na in pores. Samples with a nominal pore size of 10 nm were saturated with a 1, 2, 3, 4, and 5 M NaCl solution, respectively, and both T_1 and T_2 were determined at 0.78 T. During the experiments the temperature is kept constant at (20.0 ± 0.1) °C. To detect possible deviations from mono-exponential behavior, 100 logarithmically spaced delays were used in the T_1 measurement. No deviations are observed. The resulting relaxation rates ($R_i = 1/T_i$) are plotted in figure [5.3]. The solid line represents the bulk relaxation rate (both transverse and longitudinal). The other two lines serve as guide to the eye. From figure 5.3 it is clear that T_1 and T_2 are different. As already outlined above, the magnetization decay is mono-exponential, which implies that the Na ions are in the fast modulation regime. Hence, in our opinion, the difference between T_1 and T_2 is caused by dipolar effects. These effects, caused by magnetic field variations near the pore wall, are known to decrease T_2 much more than T_1 (note that for H in 5 nm Nucleosil samples $T_1 = 0.5$ s; $T_2 = 17$ ms). These field variations are caused by magnetic impurities [Val02a], [God01], or susceptibility mismatches [Blo48]. The

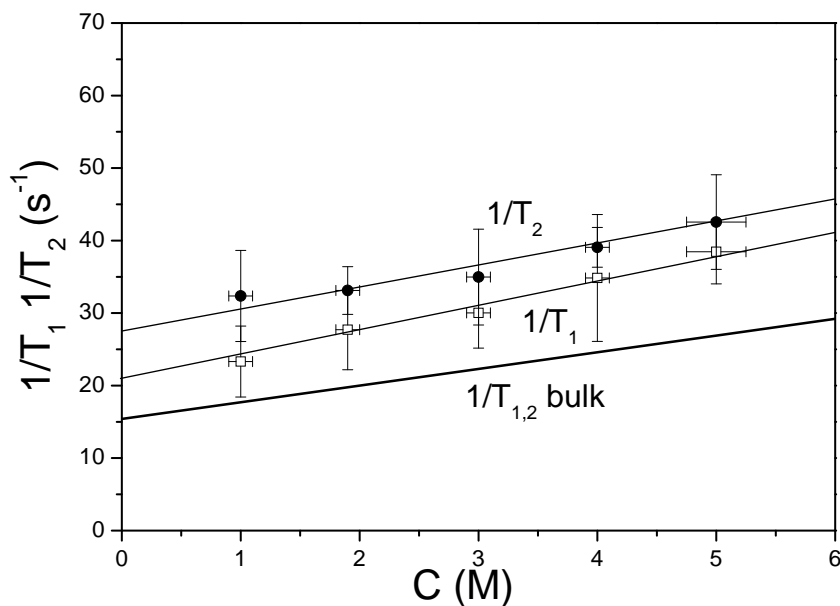


Figure 5.3: The longitudinal ($1/T_1$, \square) and transverse ($1/T_2$, \bullet) relaxation rate of Na in 10 nm pores as a function of the NaCl concentration (C).

different slopes of the lines plotted in figure 3 might suggest a small concentration dependence of the surface relaxation term in eq. 5.2. However, such a definite conclusion is not justified, given the limited accuracy of our experiments.

To study the relation between the relaxation rate and the pore size, the ultimate goal of our study, Nucleosils with 6 different pore sizes were saturated with a 4 M NaCl solution and T_1 and T_2 were determined. The sample temperature was controlled at (20.0 ± 0.1) °C. Again 100 logarithmically spaced delays were used in the T_1 measurements so that multiple exponential decays, if present, would show up in the results. In all cases, mono-exponential relaxation behavior is observed.

In figure 5.4 the sodium relaxation rates, both longitudinal and transverse, have been plotted against the inverse pore size. The pore size is determined by averaging the values obtained with different techniques, among which cryoporometry [Val02], BET, and mercury intrusion. This was done because earlier studies using these Nucleosils indicated that some of the actual pore sizes differ significantly from the nominal values [Val02]. As can be seen in figure 5.4 a clear correlation is found between the measured relaxation rates and the pore size. The difference between T_1 and T_2 increases with decreasing pore size. This can be caused by the larger probability of dipolar interaction with a smaller pore since S/V increases as the pore size decreases. The value of $1/T_2$ obtained in the 100 nm pores seems rather high, but the deviation from e.g., the bulk value is still within experimental inaccuracy. Because also the relaxation times of water were measured for the Nucleosils the ratio between the surface relaxivities of H and Na can be determined: $\rho_{2,H} = 2.4\rho_{2,Na}$. From figure 5.4 we can conclude that the Brownstein and Tarr model applies for Na

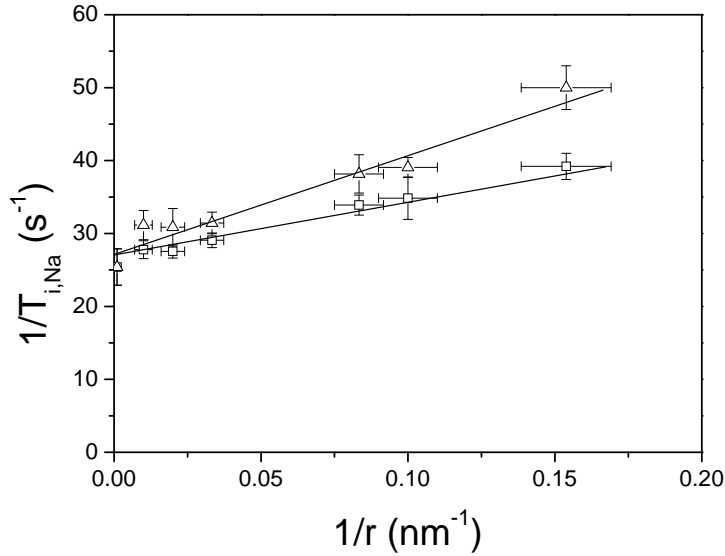


Figure 5.4: *The longitudinal (Δ) and transverse (\square) relaxation rate for Na ions as a function of $1/(\text{pore size})$ in a 4 M NaCl solution.*

ions in solution.

5.4 Discussion

The results presented in this chapter show that the Brownstein and Tarr model for relaxation in porous materials can be applied to Na ions in solution in porous materials. As already discussed in section 2, the system has to meet certain requirements to allow for interpretation within this model. First of all, the time needed by the ion to probe the pore space $t_D \approx r^2/6D$ must be smaller than the time scale of the experiment. This is the fast diffusion regime as defined by Brownstein and Tarr [Bro79].

Secondly, the system should have a fast modulation of the EFG. This criterion is met when $\omega_0 a^2/D \ll 1$ in which a is a typical distance the ion has to travel to uncorrelate the EFG. In isotropic or electrically neutral porous material, such as Nucleosil, this condition is fulfilled. In such a material a nucleus only needs to travel a small distance over the surface to loose the net EFG. An example of a system in which this conditions are not fulfilled is laponite clay [Por01], where the Na ions are the counter ion for the clay particles. Therefore a large, non-local EFG exists and the slow modulation regime is observed by a bi-exponential relaxation.

The third criterion states that the surface relaxation must be fast enough to influence the relaxation behavior. It follows from eq. 5.2 that $V/S < \rho/T_{2,b}$. When spherical pores are assumed and typical numbers are used, $T_{2,b} = 40$ ms, $\rho_{2,H} =$

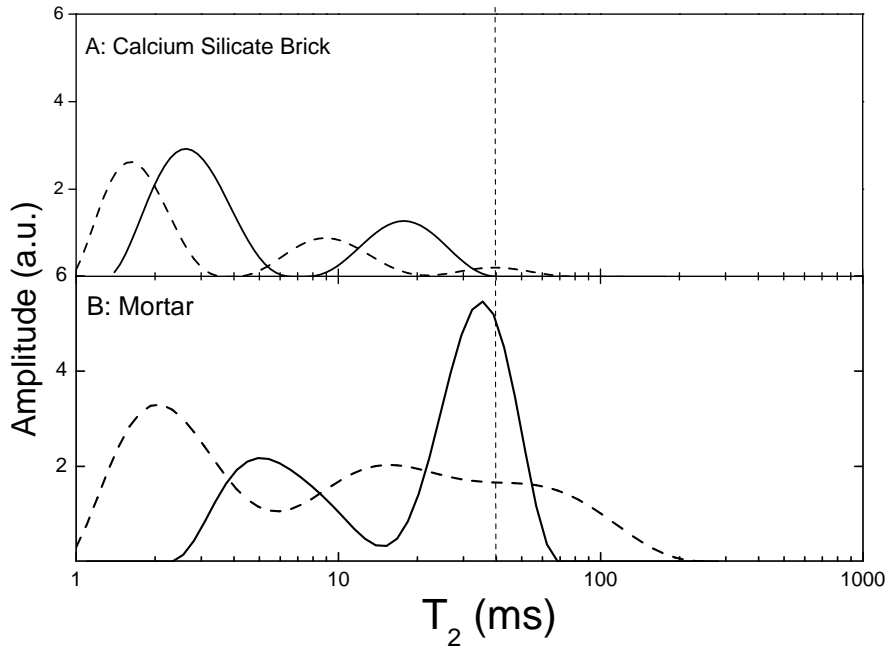


Figure 5.5: The T_2 distributions of H (dashed line) and Na (solid line) in two building materials. The dashed line is the bulk T_2 for Na.

$2.4\rho_{2,Na}$, and $\rho_{2,h} = (1.1 \pm 0.1) \times 10^{-7}$ m/s [Val01b], we arrive at a pore radius of $3.4 \mu\text{m}$ as an upper limit for the pore radius for Nucleosil.

Until now we have only discussed measurements on a model porous material. We have performed T_2 measurements with two typical building materials to show how the model can be applied to less well defined porous media with a broad pore size distribution. According to Eq. 5.2, a broad range of T_2 relaxation times is expected for such materials. From the magnetization decay, a T_2 distribution was calculated with the CONTIN program [Pro82]. The resulting distributions are presented in figure 5.5. Figure 5.5A shows the distributions for H and Na in calcium silicate brick. Clearly three peaks are present in the distribution for H. These peaks correspond to the three pore sizes in calcium silicate brick, (of the order of 10, 1 and $0.01 \mu\text{m}$ [Pel95]). Only two peaks can be seen in the Na distribution, which can be understood as follows. In the larger pores the bulk relaxation $T_{2,b}$ dominates the surface relaxation (Na: $T_{2,b} = 40$ ms, H: $T_{2,b} > 3$ s). As a consequence the method cannot discriminate between the two sets of larger pores (of the order of 10 and $1 \mu\text{m}$). Figure 5.5B shows the T_2 distribution for H and Na in a NaCl solution saturated mortar sample. Similar behavior is observed as for the calcium silicate brick. In the Na distribution, the smallest pores can be identified. The other pores cannot be discriminated. Again the criteria, mentioned above, are met for the small pores (order $0.1 \mu\text{m}$) but not for the larger pores (between roughly 1 and $100 \mu\text{m}$ [Pel95]). In order to be sure that the observed bi-exponential behavior

is not a consequence of the slow modulation of the quadrupolar interaction, the mortar sample was partially dried after the measurement. When the sample was measured again only the small T_2 peak survived. This is a signature of the drying process. It is well known that in a partially dried medium only the big pores are empty [Val01c]. This proves that the observed bi-exponential behavior has to be attributed to the pore size distribution and is not a slow modulation effect. To analyze the data quantitatively the relaxation curves have been fitted with bi- or tri-exponential functions. For the calcium silicate brick three exponents for water and two exponents for Na have to be used for an accurate fit. The fraction of nuclei in the small pores is 0.70 for H and 0.63 for Na. For mortar these fractions are 0.42 and 0.38 for H and Na, respectively. The fractions for H and Na are in good agreement with each other, which proves that the method enables us to measure Na concentrations in different parts of the pore system of a material.

5.5 Conclusions

We are able to determine pore size distributions of isotropic porous media by measuring the sodium relaxation and using the Brownstein and Tarr model. We have shown that this method is useful for pore systems with sizes smaller than 1 μm , due to the fast relaxation of sodium in bulk solution.

6. Salt supersaturation determined by NMR

abstract

Salts are considered as an important cause of weathering of building materials and natural rock. One of the proposed mechanisms of this weathering is crystallization pressure, which is a pressure on the crystal caused by its surface tension. Because of this a pressure of the same order of magnitude is exerted to the pore wall, and hence can cause damage. The pressure on the crystal causes the solubility of the salt inside the porous material to be different from the bulk solubility. With NMR we measured the solubility of Na_2CO_3 and Na_2SO_4 in a series of model porous materials. Using these data the surface energies were determined as $\sigma^{\text{cl}} = (0.09 \pm 0.02) \text{ N/m}$ and $\sigma^{\text{cl}} = (0.10 \pm 0.04) \text{ N/m}$ for Na_2CO_3 and Na_2SO_4 , respectively. The maximum pore size in which damage can be caused by this mechanism is calculated. This limit is not reached in common building materials in our experiments. To explain the actually observed damage, we discuss other mechanisms that may play a role.

6.1 Introduction

The presence of salts is widely recognized as an important cause of damage in building materials, e.g., both modern built structures as well as cultural heritage [Gou97]. An example of salt damage is given in figure 6.1, which shows a statue of a soldier, positioned close to the sea in France. The legs of the statue are eroded by salt weathering and a kind of honeycomb structure is created. This is just a typical example and many more can be found.

However, not only built structures are damaged by salt weathering, this process is also responsible for weathering of rock formations. An example is given in figure 6.2, which shows tafoni in Arches National Park in Utah, USA. Tafoni are holes in a rock formation which are formed because of salt weathering.

Little is known of the physical mechanisms responsible for the occurrence of damage. Various mechanisms have been proposed but none has been generally



Figure 6.1: *A statue of a soldier in La Rochelle (France). The legs of the statue have suffered erosion caused by salts. (Photo by Rob van Hees)*

accepted. Two major mechanisms are assumed to be responsible for salt damage: Hydration pressure and crystallization pressure. Hydration pressure may result from expansion of salt crystals during hydration. Recent experiments of Rodriguez-Navarro and Doehne [Rod99a], however, raise a certain doubt whether or not this mechanism actually occurs.

The purpose of this paper is to experimentally evaluate the mechanism of crystallization pressure. In section 6.2 the relevant theory is reviewed very briefly. In section 6.3 the experimental materials and methods are described. In section 6.4 the results of the experiments are presented whereas in section 6.5 the results are discussed and the damage mechanism is evaluated.

6.2 Theory

Crystallization pressure arises from the surface energy of a crystal when it is formed in a confined space, such as a pore in a porous building material. The situation is schematically depicted in figure 6.3. The pressure, which is exerted on the pore wall, is given by [chapter 2]:

$$p = (\sigma^{cl} \cos \theta - \sigma^{lv} \cos \phi) \frac{2}{r}, \quad (6.1)$$

in which σ^{cl} is the surface tension of the crystal-liquid interface, σ^{lv} is the surface tension of the liquid-vapor interface, and ϕ and θ are the contact angles between the various phases (see figure 6.3). The surface tension shifts the solubility concentration



Figure 6.2: An example of tafoni in Arches National Park, Utah, USA.

C from the bulk solubility C_0 according to [chapter 2]

$$\frac{2}{r} = \frac{-nRT/\nu_s^c}{F} \left[\ln \left(\frac{F + \sigma^{lv} \cos \phi \tilde{v}_s^l C \nu_w^l / \nu_w^c}{F + \sigma^{lv} \cos \phi \tilde{v}_s^l C_0 \nu_w^l / \nu_w^c} \right) - \ln \left(\frac{C}{C_0} \right) \right] - \frac{nRT}{\tilde{v}_s^l \sigma^{lv} \cos \phi} \ln \left(\frac{F + \sigma^{lv} \cos \phi \tilde{v}_s^l C \nu_w^l / \nu_w^c}{F + \sigma^{lv} \cos \phi \tilde{v}_s^l C_0 \nu_w^l / \nu_w^c} \right)$$

with r the pore radius. In this equation $F \equiv -\sigma^{cl} \cos \theta - \sigma^{lv} \cos \phi (1 - \nu_w^l / \nu_w^c - \tilde{v}_s^l / \nu_s^c)$, n is the number of ions per unit salt (2 for NaCl and 3 for Na₂SO₄), R the gas constant, T the absolute temperature, ν_s^c the molar volume of the salt in the crystal, ν_w^l the molar volume of the water in the liquid, ν_w^c the molar volume of the water in the crystal, and \tilde{v}_s^l the partial volume of the salt in the solution. If the crystals that are formed are anhydrous and the porous medium is saturated, this equation transforms into the commonly known equation [Cor49][Sch99]:

$$\frac{nRT}{\nu_s^c} \ln \left(\frac{C}{C_0} \right) = \frac{-2\sigma^{cl} \cos \theta}{r}. \quad (6.2)$$

Equation 6.2 shows that the solubility of a salt inside pores can be different from the solubility in a bulk solution. If the stress caused by the surface tension is a compressive stress on the crystal, the solubility increases. The solubility inside porous material thus allows us to study the crystallization pressure mechanism. A method to study the crystallization pressure mechanism is therefore to *experimentally* determine the solubility inside the porous material.

Supersaturation refers to a situation when the concentration in a salt solution is larger than the solubility. Usually it is caused by a lack of nucleation sites. In studies on salt damage, however, the term supersaturation is used when referring

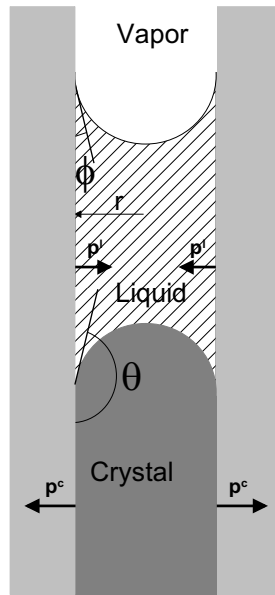


Figure 6.3: *A crystal in a pore in an unsaturated porous material. Because of the surface tension of the crystal it is under pressure. This pressure can be exerted on the pore wall and is depicted by P .*

to an increase of the solubility inside the porous material. An essential difference between these two effects is that the first is a non-equilibrium effect, i.e., there is no thermodynamic equilibrium and the system is – in principle – instable, whereas the latter is an equilibrium effect and hence the system is stable. In this thesis we will use supersaturation for the equilibrium increase in solubility, unless explicitly stated otherwise. In doing experiments one has to make sure that thermodynamic equilibrium indeed exists, otherwise an interpretation in terms of pressures caused by the salts is incorrect. If no crystal is present, a (non-equilibrium) supersaturation can exist without causing damage.

It is common that salts have different crystal phases at different temperatures. As an example we consider Na_2SO_4 which has two stable phases, mirabilite and thenardite. Mirabilite is a hydrated phase whereas thenardite is an anhydrous phase. Sodium sulfate is not chosen just as an example, but it is one of the most damaging salts in built structures. The solubility for both phases is given in figure 6.4. As can be seen mirabilite has a strong temperature dependence whereas thenardite has only a weak temperature dependence. The solubility for this salt is given by the lowest possible curve, in figure 6.4 the thick curve. The change between the two crystal phases is the point at which the two phases have the same solubility (in the figure A). Next a pressure is applied and for both phases the solubility at this pressure is calculated using equation 6.2. The change in solubility is given by the arrows. The solubility of the salt again is the lowest possible curve. In figure 6.4 also a ΔT is given, this is the temperature shift that can be determined by the experiment,

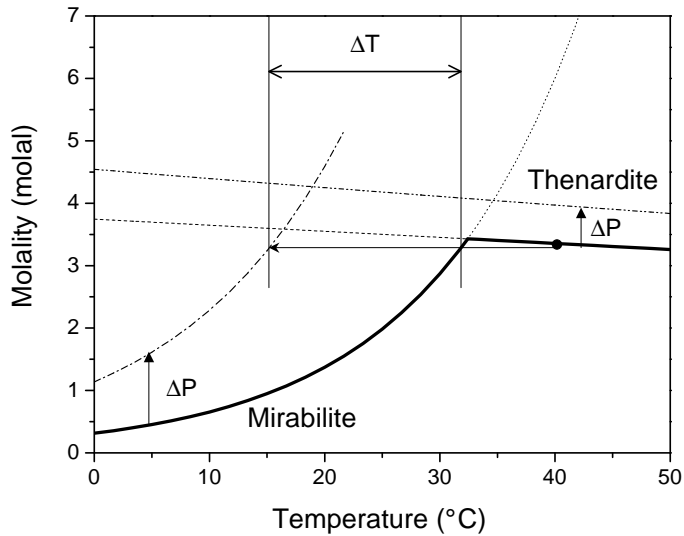


Figure 6.4: *Plot of the solubility of Na_2SO_4 as an illustration of the temperature shift (ΔT) of the phase transformation if a pressure is applied. The thick line represents the bulk solubility. The experiment is started at $40\text{ }^\circ\text{C}$, the concentration cannot exceed this value throughout the experiment.*

which will be further explained in the next section.

6.3 Materials and Methods

Considering the fact that the supersaturation will show up in the solubility, one actually wants to measure the solubility inside the pores without disturbing it. Measuring the solubility of a salt solution inside a porous material is not an easy issue when it exceeds the bulk solubility. If, for instance, a porous material would be immersed in a bulk solution and the solution above it would be probed, this solution would limit the concentration to the bulk solubility. We have used Nuclear Magnetic Resonance (NMR) to measure the salt concentration inside the pores.

NMR is a commonly used technique for chemical analysis (MR spectroscopy) [Sli90] or medical diagnosis (MR Imaging) [Vla96]. If a material is placed in a magnetic field, its magnetic moments, called spins, will align to this magnetic field, forming a magnetization. This magnetization can be manipulated by use of radio frequency pulses. Nuclei can be probed selectively because their resonance frequency f depends on the type of nucleus and is given by the condition $f = \gamma B$, B is the applied magnetic field and γ the gyromagnetic ratio (42.5 MHz/T and 11.25 MHz/T for hydrogen and sodium, respectively). After manipulation of the magnetization it

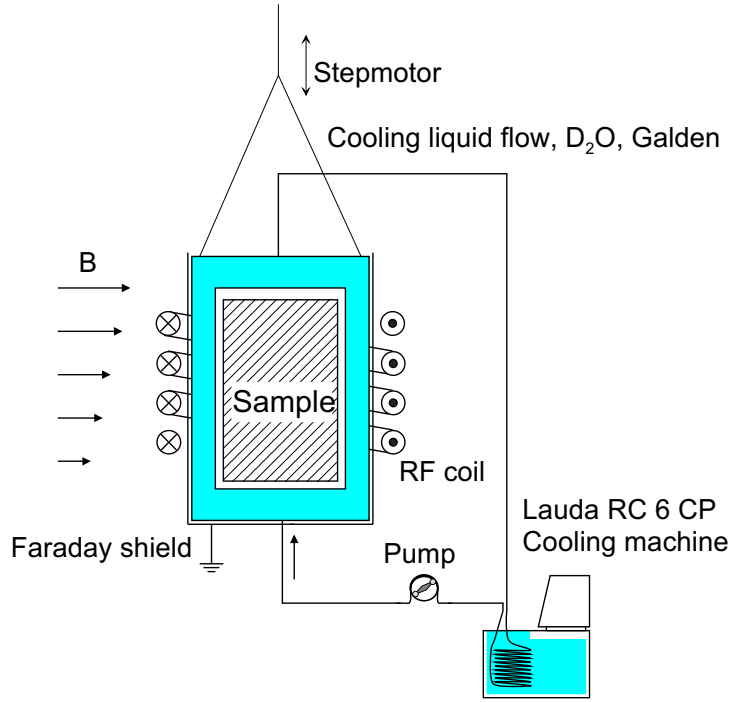


Figure 6.5: *Schematic overview of the central part of the NMR scanner. For a detailed explanation see the text.*

will restore towards its original state. This process is called relaxation, characterized by two relaxation times, T_1 and T_2 . The intensity of the NMR signal is given by:

$$S_{echo} \propto \rho \left[1 - e^{-\frac{TR}{T_1}} \right] e^{-\frac{TE}{T_2}} \quad (6.3)$$

in which TR is the repetition time of the measurement, TE the so-called echo time, and ρ the density of the nuclear spins. Usually the relaxation times depend on the local environment of a nucleus. This enables us to discriminate between liquid and crystal phases in our measurements. Because the relaxation of sodium nuclei in a crystal is fast compared to the relaxation of sodium in solution, we can only measure the ions in solution. The same applies to water in solution and water in the crystal. Apart from this, the relaxation of water is a good measure for the size of the pore in which the water resides [Bro79].

The NMR experiments were performed using a home built 0.78 T scanner. A schematic overview of the central part of the scanner is given in figure 6.5. The magnetic field B_0 is generated by an iron-core electromagnet. The scanner is equipped with a Faraday shield [Kop94] inside a solenoid radio frequency (RF) coil. Because of the Faraday shield the induction and parasitic capacity of the coil hardly change when the sample is changed or, more important, when the properties of the sample itself change. Because of this the signal intensity is to a large extent proportional to

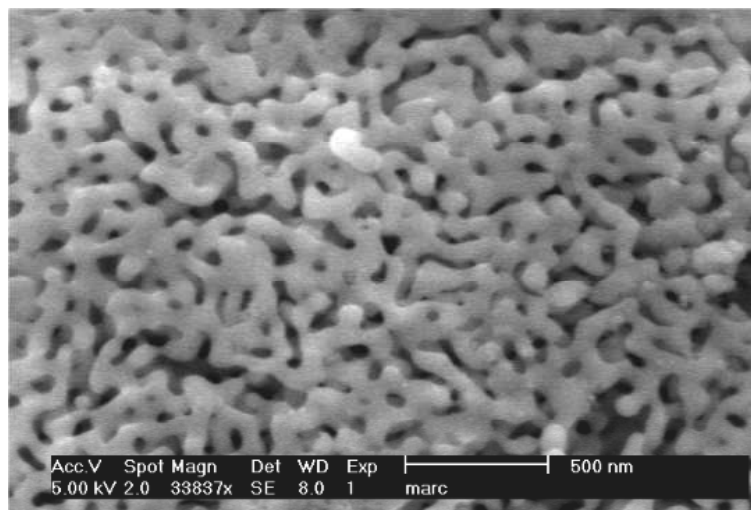


Figure 6.6: A Scanning Electron Microscopy image of Nucleosil with a nominal pore size of 100 nm. The bar indicates a length scale of 500 nm.

the amount of nuclei according to equation 6.3. Hence quantitative measurements can be performed with this NMR scanner.

The NMR scanner has a RF circuit of which the frequency can be tuned to H or Na. The tuning can be changed easily by adding or removing a capacitor by means of a switch. This can be done during an experiment, which results in quasi-simultaneous measurements of both species.

The temperature of the sample holder can be accurately controlled. This is achieved by flowing a cooling liquid through a heat exchanger in the wall of the sample holder. Because quantitative NMR measurements have to be performed the cooling liquid has to meet various requirements. First of all, it should not be visible by NMR in our experiments, which means that it cannot contain H or Na. Second, it should have a low electric conductivity, since otherwise it would shield the alternating RF magnetic fields. And, finally, it should not chemically react with the PVC sample holder or the tubes used. One cooling liquid has been found suitable: Galden¹, which can be used above -30 °C. Galden is a fluorinated fluid containing carbon, oxygen, and fluor. It is especially designed as a cooling liquid, and therefore very suitable for this application. Because this cooling liquid is rather expensive and easily evaporates, a separate closed cooling circuit is used for the sample cooling. The cooling liquid is pumped by a peristaltic pump to prevent pollution of the coolant. A Lauda RL6CP temperature bath is used to control the temperature of a copper spiral through which the coolant flows.

To determine the relation between supersaturation and pore size, a model material with a single dominant pore size is used as compared to a wide pore size

¹Galden PFPE is a registered trademark of Solvay Solexis, <http://www.solvaysolexis.com>

distribution of most building materials. This model material (Nucleosil) is a dried silica gel. Nucleosil can be obtained in various nominal pore sizes and various grain sizes. In our experiments all grain sizes were $10\ \mu\text{m}$. Each grain contains pores in the nm scale. A Scanning Electron Microscopy image of Nucleosil with a nominal pore size of 100 nm is given in figure 6.6. Earlier work on these Nucleosils [Rij04][Val02] showed that the nominal 5 nm Nucleosil actually has a pore size of about 7 nm, whereas the 10 and 12 nm are indistinguishable in many experiments, including BET (low-temperature gas adsorption-desorption). Therefore we will refer to the 5 nm Nucleosil as 7 nm Nucleosil. Here we need to remark that each method to determine the pore size of a material is based on a certain model. Different methods may yield different pore sizes, because of different assumptions in the underlying models. Some of these are related to the (necessary) simplification of the actual pore geometry. The ratio between pore sizes derived using the same model is usually more accurate than the absolute value. We have interpreted both our NMR and sorption (chapter 7) experiments in terms of basically the same model. Since the sorption experiments indicate that the pore size of our materials should be associated with the pore radius of the cylindrical pores used in our model, we have adapted this choice throughout the thesis.

Nucleosil powder samples were prepared in a PMMA (perspex) cylinder of 18 mm inner diameter and 3 mm height. The powder was wetted with a solution of either Na_2SO_4 or Na_2CO_3 , saturated at $40\ ^\circ\text{C}$. For both salts the solubility is highly temperature dependent. Care was taken not to wet the powder too much, since in that case also solution outside the pores will show up in the measurement. Because of capillary action the solution penetrates into the pores of the grains. After wetting the samples the PMMA holder was sealed using Chloroform. At $40\ ^\circ\text{C}$ the concentration of the solution is known and can be used later on as a reference. Next the sample was placed in the NMR scanner and cooled to $2\ ^\circ\text{C}$, inducing a supersaturation. After nucleation had occurred the samples were heated slowly, such that thermodynamic equilibrium was always guaranteed. During this heating, NMR measurements were performed. Both Na and H intensity profiles and NMR relaxation times were measured: from the intensity profiles the solution concentration can be determined, whereas the relaxation measurements give information on the pore size. NMR relaxation measurements can be used to see whether or not damage is created. To calibrate the NMR signal, a 3 molal NaCl reference sample is measured during every experiment. The solubility of NaCl does not depend on temperature in the range $0\text{--}40\ ^\circ\text{C}$. The concentration in the sample can be determined by dividing the Na NMR intensity by the H NMR intensity. The experiment starts at $2\ ^\circ\text{C}$ at which the concentration in the solution is given by the solubility (see figure 6.4). As the temperature increases, the solubility also increases and hence the measured concentration. This continues as long as there is enough salt present. Because the amount of salt is limited by the initial salt concentration at $40\ ^\circ\text{C}$ this is the maximum value that can be found for the concentration. From this value on the concentration is stable and deviates from the solubility. The point at which the solubility starts to deviate from the measured concentration is shown by a kink in

the measurement and is a measure for the amount of supersaturation. Hence by the difference between this point in bulk and in porous material, supersaturation can be determined. This difference is called ΔT , and is shown in figure 6.4.

6.4 Results

First, the calibration method of the NMR signal was tested. We compared the signal intensities of 3 Molal NaCl solutions to those of saturated solutions of Na₂SO₄ and Na₂CO₃. The concentration of these saturated solutions was also determined by ion chromatography. This experiment revealed that for bulk solutions our concentration measurements are accurate and reproducible within 5 %. The relaxation time T_2 of Na ions in NaCl is about 40 ms whereas T_2 is of the order of 15 ms and 20 ms for Na₂CO₃ and Na₂SO₄ solutions, respectively. For Na the echo time is 800 μ s, which results in a signal loss because of relaxation of $\exp(-0.8[\text{ms}]/T_2[\text{ms}])$. For the NaCl calibration sample 98 % of the sodium is measured, whereas for Na₂CO₃ and Na₂SO₄ samples this is 94 % and 96 %, respectively. Therefore the *measured* Na₂CO₃ concentration is expected to be 4 % lower than it actually is. This is 2 % for Na₂SO₄. All measurements presented here have been corrected for this effect.

6.4.1 Sodium carbonate

Experiments were done for bulk Na₂CO₃, and samples with nominal pore sizes of 30, 12, 10, and 5 nm (actual pore sizes 30, 10, 10 and 7 nm) as given in figure 6.7. The measured concentration for the bulk coincides with the available solubility data [Lid98]. At 32 °C a phase transition occurs between a deca-hydrated phase at lower temperatures and a hepta-hydrated phase at higher temperatures. At 34 °C this hepta-hydrated phase transforms into a monohydrated phase which is stable above that temperature. In some of the bulk measurements, it appears that the transition of this hepta-hydrated phase towards the deca-hydrated phase does not occur during nucleation. In these measurements the bulk coincides with the solubility curve of the hepta-hydrated phase [Ull03]. Since in the porous materials this was not observed we further neglect this phase. The measurements for the solution inside the pores show a temperature shift, as explained in section 6.2. This temperature shift very strongly suggests that a supersaturation must be the case.

However, the measured concentration inside the pores is far below the expected value: at 40°C the concentration in the bulk and the pores must be the same, which is not observed in the NMR measurements. This can be explained as follows: for Na NMR it is known that the signal can be influenced by the quadrupolar character of the nucleus [Por01]. Basically two regimes exist: a slow and a fast modulation regime. In the first regime quadrupolar effects are significant, whereas in the second regime these can be neglected because they are averaged out by the movement of the ions. In earlier NMR experiments on NaCl solutions, both bulk and in Nucleosil samples showed that this system is within the fast modulation regime [Rij04]. If Na₂CO₃ in Nucleosil is not within this regime this must show up in the relaxation

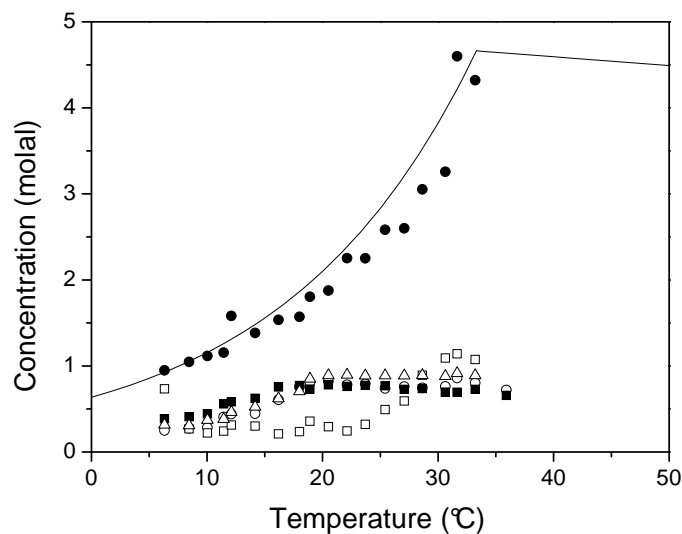


Figure 6.7: The raw NMR measured concentrations of Na_2CO_3 solution in bulk (●) and inside Nucleosil 7 nm (■), 10 nm (○), 12 nm (△), and 30 nm (□), before corrections were applied. The measured values for the concentration at temperatures close to 40°C do not match. The temperature shift ΔT_{exp} , as explained in figure 6.4 is clearly visible.

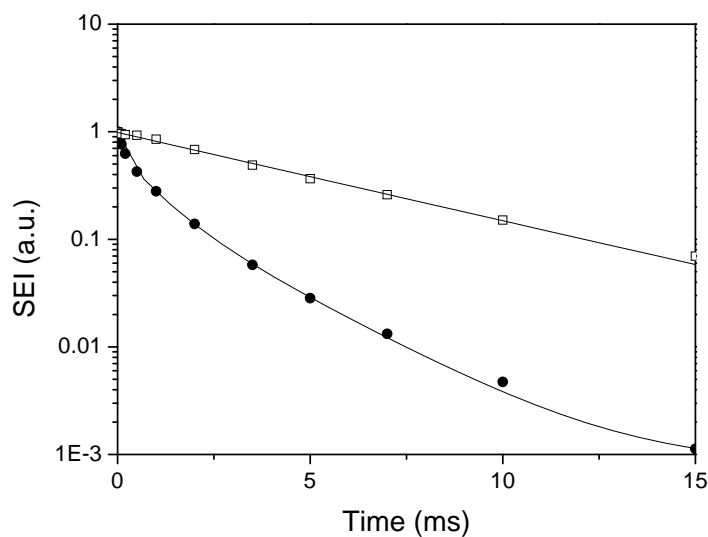


Figure 6.8: NMR T_2 relaxation curves for NaCl (□) and Na_2CO_3 (●) in Nucleosil with 7 nm pores. For NaCl the relaxation can be described by a single exponential fit, whereas for Na_2CO_3 the signal decay needs to be described by a multi exponential fit.

behavior; in that case multiple values for T_2 are observed [Por01]. This usually results in loss of Na signal because a significant amount of this signal has relaxed before observation. To verify this hypothesis we analyzed several samples containing Na_2CO_3 and NaCl solutions in a 11.7 T Bruker spectrometer. Figure 6.8 shows a typical measured T_2 curve for NaCl and Na_2CO_3 in 7 nm Nucleosil. As can be seen the NaCl signal decays mono-exponentially, but the Na_2CO_3 signal decay is governed by various time constants. It is therefore clear that the Na_2CO_3 solution inside the porous material is in the slow modulation regime and this is causing a significant signal loss.

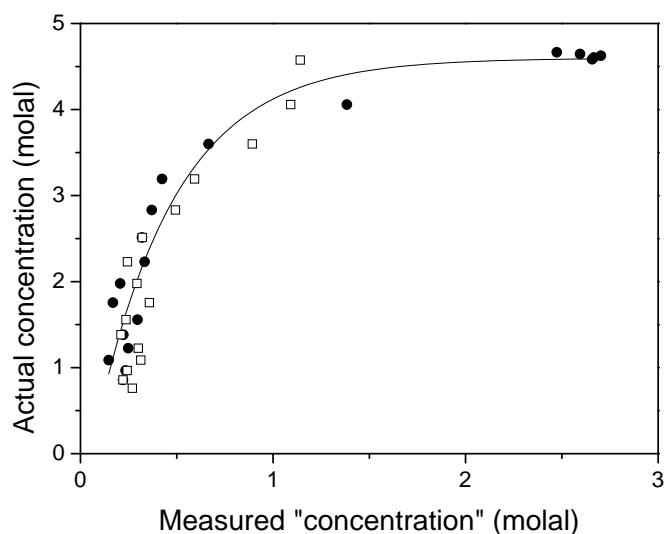


Figure 6.9: *Calibration curve between measured concentration and actual concentration based on a 100 nm Nucleosil measurement (●). The concentration in 100 nm Nucleosil equals the bulk solubility, since no temperature change in the phase transition is observed. The calibration curve, used to correct the measurements, was determined by a least squares fit. For comparison also the data of the 30 nm are plotted (□).*

We do not fully understand why the Na_2CO_3 solution is in the slow modulation regime. We hypothesize that because a Na_2CO_3 solution is a base ($\text{pH} = 12$), protons are dissociated from the silica surface introducing a surface charge. Such surface charges are reported to give rise to the slow modulation regime [Por01]. In crystallization experiments, at an echo time of $800 \mu\text{s}$, already a significant amount of Na signal has vanished for the Na_2CO_3 solution. As a result the measured Na concentration is much too low. To correct for this effect a calibration was performed using a 100 nm Nucleosil sample. The calibration curve is given in figure 6.9. This sample did not show a temperature shift of the phase transition and therefore its concentration in the entire temperature region is assumed to be equal to the bulk solubility. In this figure also the 30 nm data points have been plotted. Since these

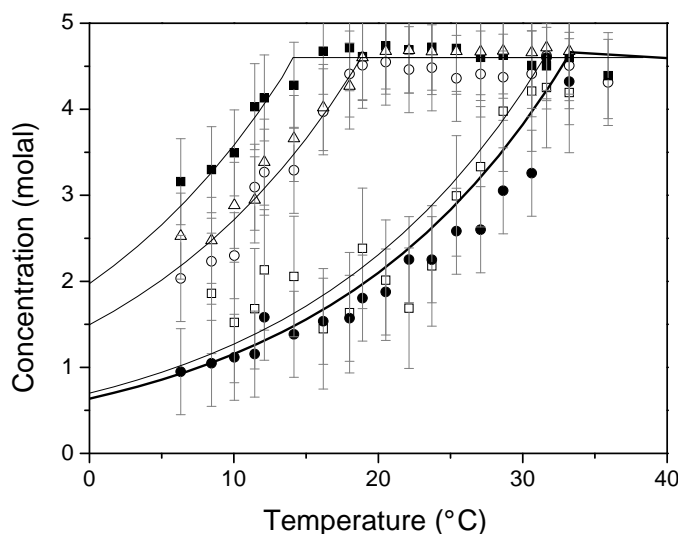


Figure 6.10: Na_2CO_3 solubility in bulk (\bullet) and inside the pores of Nucleosil 7 nm (\blacksquare), 10 nm (\circ), 12 nm (\triangle), and 30 nm (\square). The thick curve represents the literature values for the solubility. The other curves are fits to the data obtained by multiplying the solubility by a factor. Because in the experiments the concentration cannot exceed the initial bulk 40 °C concentration, the lines are horizontal once this concentration is reached, and the measured concentration deviates from the solubility here. The solution in the 7 nm pores has an increase in the solubility by a factor 3.1, whereas this is 2.3 in the 10 and 12 nm pores and 1.1 in the 30 nm pores.

have almost no temperature shift compared to bulk it is expected that these data coincide with the calibration curve which these do.

After applying this calibration, it appeared that for pore sizes below 100 nm, the observed concentration at 40 °C, which is above the phase transition, was still somewhat lower than expected. This can be explained by the fact that the contribution of the individual relaxation modes to the NMR signal depends on the pore size. Because the actual pore-size dependence of these modes is not known, the results for all other samples were scaled to the 100 nm sample at 40 °C, at which temperature all samples have the same Na_2CO_3 concentration.

The resulting solubility measurements are given in figure 6.10. It can be seen that the solubility inside the 30 nm pores hardly differs from the bulk solubility. However, the solubility inside the 7, and 10 nm pores is significantly higher. Note that two different 10 nm Nucleosils are used, being those of 10 and 12 nm *nominal* pore size. It is therefore not surprising that results for the 10 and 12 nm Nucleosil coincide in this experiment. The supersaturation ratio for the nominal 7 nm pore is 3.1 whereas this ratio is 2.3 for the nominal 10 and 12 nm pores. The supersaturation ratio as a function of $1/r$ is plotted in figure 6.11.

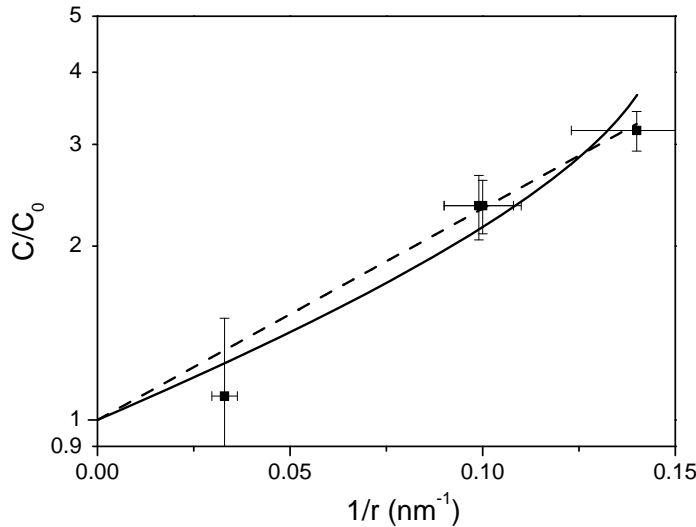


Figure 6.11: *Supersaturation ratio as determined by NMR for Na_2CO_3 as a function of $1/r$. The solid curve is a fit using equation 6.2 (resulting in $\sigma^{cl} = (0.09 \pm 0.02)$ N/m, with mean square sum $\chi^2 = 0.47$) and the dashed line is a fit using equation 6.2 (resulting in $\sigma^{cl} = (0.15 \pm 0.03)$ N/m, and $\chi^2 = 0.09$).*

In literature Eq. 6.2 is often discussed while speaking about hydrous crystals (for instance [Igl97]). Doing so, and using bulk water value $\sigma^{lv} = 0.072$ N/m [Lid98], and assuming the contact angles to be 180° and 0° for the crystal-liquid and liquid-vapor interface, respectively, a fit to the data is made, which is shown as the dashed curve in figure 6.11. From this fit an estimate for the surface tension of the salt in solution can be made, which is (0.15 ± 0.03) N/m. As we have seen in chapter 2 equation 6.2 is valid for an anhydrous crystal in a saturated porous material. In fact the experimental situation is an unsaturated porous material containing a hydrous crystal. The accurate equation to use then is eq. 6.2 which results in the solid curve in figure 6.11 and a surface tension of $\sigma^{cl} = (0.09 \pm 0.02)$ N/m. Although the experimental data agree well to both equations, we prefer the latter analysis.

6.4.2 Sodium sulfate

In contrast to the Na_2CO_3 measurements, the Na_2SO_4 measurements do not reveal any loss of Na signal. Na_2SO_4 has three possible crystal phases: an anhydrous phase (thenardite), a decahydrated phase (mirabilite), and a hepta-hydrated phase which is meta-stable [Bra71]. The measured solubilities of Na_2SO_4 of bulk solution and solutions in Nucleosil with pore sizes of 7, 10, and 30 nm are plotted in figure 6.12. The concentration at 40°C is somewhat low because the initial solution was prepared at approximately 60°C . All curves coincide with the solubility of the

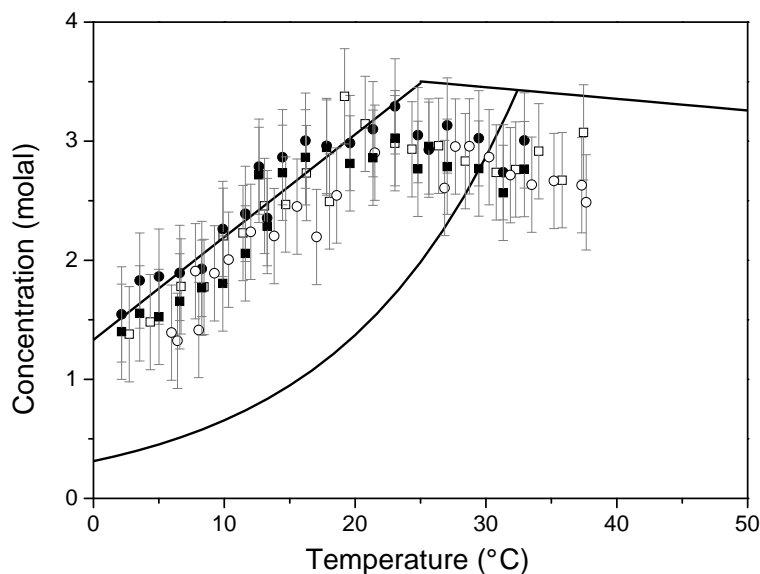


Figure 6.12: *The measured solubility of Na_2SO_4 in bulk (\bullet) and inside a series of Nucleosil model porous materials with pore sizes 7 nm (\blacksquare), 10 nm (\circ), and 30 nm (\square). The concentration at 40 °C is somewhat low because the initial solution was prepared at approximately 60 °C.*

$\text{Na}_2\text{SO}_4 \cdot 7\text{H}_2\text{O}$ crystal known from literature. For the bulk this has been observed before [Mey28]. Because this phase is meta-stable it is expected to transform into mirabilite ($\text{Na}_2\text{SO}_4 \cdot 10\text{H}_2\text{O}$) later on. However, this transformation was not observed on a time scale of 2 weeks. It is remarkable that the solubility is independent of the pore size. This independence is either caused by a very low surface energy or by a contact angle of 90 °. In both cases the crystal is not under pressure. It implies that no significant increase in solubility occurs, and therefore no damage is caused. This conclusion was supported by an experiment in which four temperature cycles were made. An analysis of the relaxation time distributions revealed no changes in the pore-size distributions and consequently no damage.

Because it is known that the hepta-hydrated phase is a meta-stable one we performed various actions to try to create mirabilite, including shaking the sample during the experiment, rapid temperature changes and a sinusoidal temperature change. Figure 6.13 shows the measured solubility of the latter experiment. The inset in this figure shows the temperature set points. As can be seen no transformation took place. Also none of the other efforts resulted in a phase transformation.

To verify that the crystal formed indeed was the hepta-hydrated phase a PMMA sample holder was made which had a bottom of 12 μm Mylar. The sample can then be placed upside down in an X-ray diffractometer to determine the crystal morphology. Both a bulk and 7 nm Nucleosil sample were made. First the samples were placed in the NMR setup and the measurements again showed the hepta-hydrated

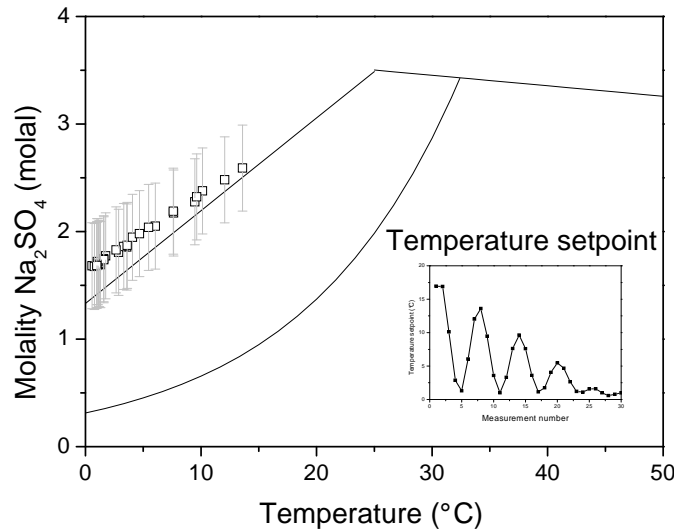


Figure 6.13: Measured solubility of Na_2SO_4 . During the experiment sinusoidal temperature set-points are applied to push the crystal over the meta-stability border. The effort is not successful, the crystal stays in the meta-stable $\text{Na}_2\text{SO}_4 \cdot 7\text{H}_2\text{O}$ phase.

phase. Next the samples were taken out, and placed in an X-ray diffractometer. Determining the crystal morphology was unsuccessful. During this procedure, the samples experienced various temperatures and movements. After the experiment, the crystal had changed into mirabilite as observed by the solubility measured by NMR. In figure 6.14 the solubility measured of these samples is plotted. The data points coinciding with the solubility of the hepta-hydrated phase are taken before the X-ray experiment (indicated by 1 in the figure). After the X-ray experiment, indicated by X in figure 6.14, the supersaturation ratio $C/C_0 = 2$ at temperatures below 10 °C. The supersaturation decreases as the temperature rises above 10 °C, indicated by the trajectory 2 in figure 6.14. A possible explanation for this is that salt crystals grow outside the Nucleosil and consume the supersaturation. When the sample temperature has been above 32 °C, and it is lowered again, the hepta-hydrated phase is again formed, shown by the trajectory 3 in the figure. The results suggest that a mirabilite crystal is not formed easily. Note that in the all our experiments we started with a solution just below saturation, and therefore no mirabilite nuclei exist before starting the experiment.

Using the obtained supersaturation ratio, the value $\sigma^{lv} = 0.072 \text{ N/m}$, and assuming the contact angles to be 180° and 0° for the crystal-liquid and liquid-vapor interface, respectively, it is possible to estimate the surface tension of the crystal-liquid interface: $\sigma^{cl} = (0.10 \pm 0.04) \text{ N/m}$.

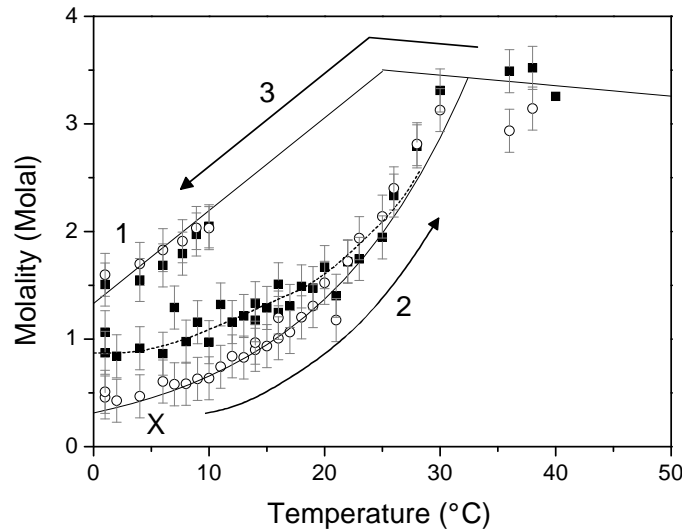


Figure 6.14: Concentration data obtained by NMR for bulk solution (\circ) and solution inside 7 nm pores (\blacksquare). At first (1) the hepta-hydrated crystal is formed. After extensive manipulation of the sample during X-ray analysis a phase transition into mirabilite has taken place (X). Subsequent heating (2) results in a transition from mirabilite to thenardite at $T \approx 32^\circ\text{C}$. When the temperature decreased again (3), the hepta-hydrated crystal was formed again.

6.4.3 Salt in Building materials

The same type of measurements, as were presented for model materials, were done on several typical building materials. A difference between the measurements presented above and the results presented here is that the latter experiments were performed at 1.5 T instead of 0.78 T.

In figure 6.15A the measured Na_2CO_3 concentration inside Savoniere stone is plotted. Savoniere stone is a natural stone that is used in many monumental buildings. It is not a very hard stone, and can be crumbled easily, which is very useful to shape it. Savoniere stone has a broad pore size distribution with pores ranging from $0.1\ \mu\text{m}$ to $100\ \mu\text{m}$ [Roe03]. It can be seen that no supersaturation is observed in this particular stone.

During the experiment the T_2 distribution of the water has also been measured. This distribution, which is a measure for the pore size distribution, is plotted in figure 6.15B. At a temperature of 40°C a broad relaxation time distribution is visible over four orders of magnitude. Below 30°C the water signal of the largest pores vanishes. This shows that the crystallization of the salt has taken place in the largest pores. In these pores the pressure on the crystal can be neglected, which means that no supersaturation can be observed. As a consequence no damage is caused in this experiment.

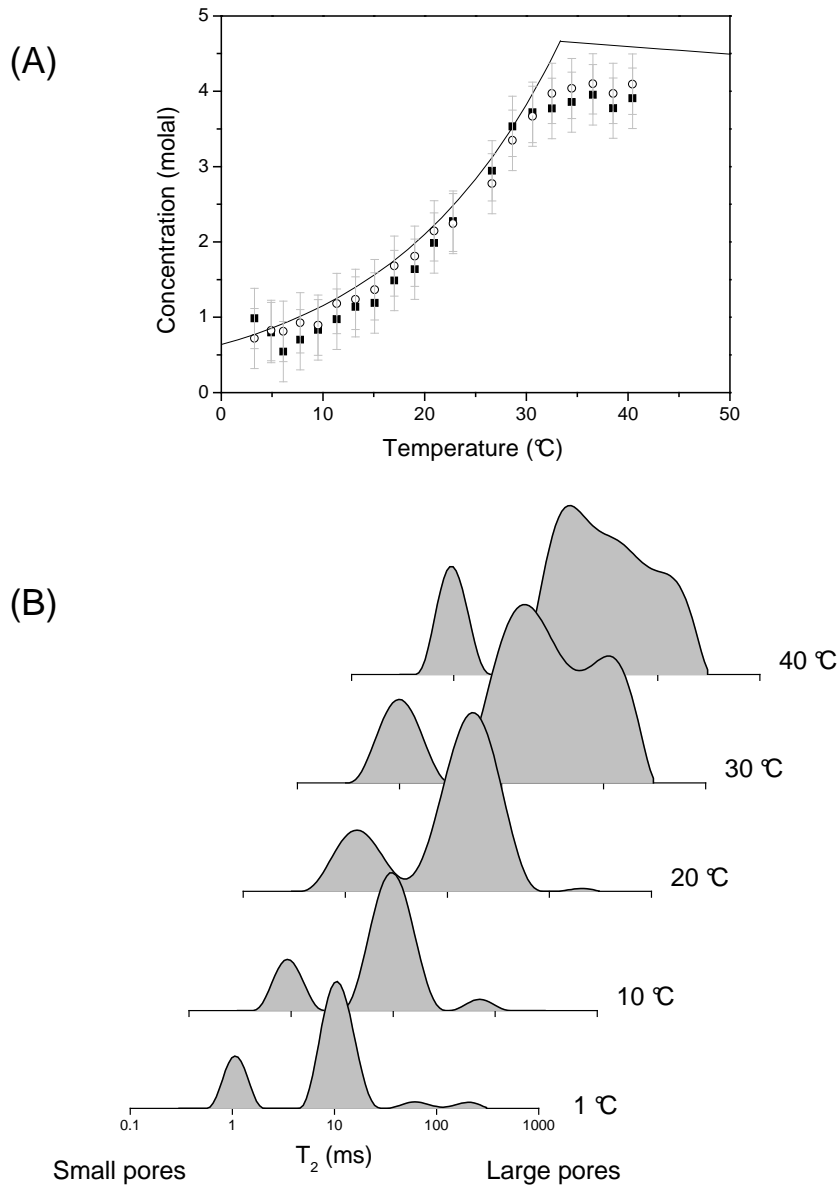


Figure 6.15: **(A)** Solubility of Na_2CO_3 in bulk solution (\circ) and Savoniere stone (\blacksquare). The solid line represents the literature value [Lid98]. The solution inside the Savoniere stone does not reveal supersaturation. **(B)** Water relaxation time distribution, as a function of temperature in Savoniere stone. Salt crystals are formed in the largest pores, Because the formed crystal is $\text{Na}_2\text{CO}_3 \cdot 10\text{H}_2\text{O}$ also the water signal disappears from the larger pores as crystals are formed.

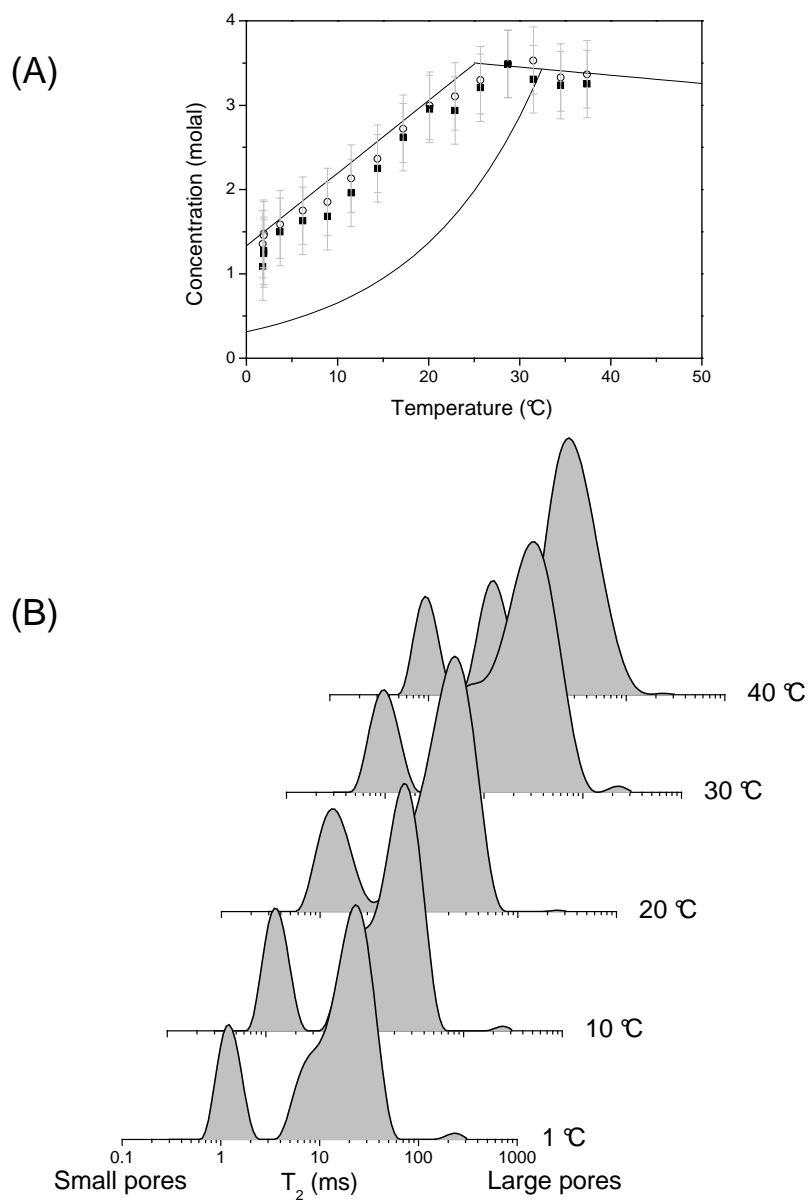


Figure 6.16: (A) Solubility of Na_2SO_4 in bulk solution (\circ) and Savoniere stone (\blacksquare). The solid line represents the literature value [Lid98],[Bra71]. (B) Water relaxation time distribution, as a function of temperature in Savoniere stone containing Na_2SO_4 solution. As temperature decreases the shape of the curves stays the same which shows that crystallization is not taking place in a specific pore size.

Measurements were performed on a Na_2SO_4 solution inside Savoniere stone, fired clay brick, mortar and calcium silicate brick. Mortar has typical pore-sizes from 10 nm to 100 μm , calcium silicate brick has pore-sizes from 1 nm to 100 μm and fired clay brick has typical pore sizes of 0.1 μm to 100 μm [Pel95]. The Na signal in the calcium silicate brick showed a significant decrease compared to the bulk. This was attributed to quadrupolar slow modulation, which was discussed in chapter 3. A scaling of the concentration at 40°C was performed. The other three materials do not show Na signal loss.

Figure 6.16A shows the measured concentration inside Savoniere stone and bulk. In Savoniere stone the meta-stable $\text{Na}_2\text{SO}_4 \cdot 7\text{H}_2\text{O}$ was formed. Figure 6.16B shows the water relaxation time distribution in Savoniere stone. The shape of the curves hardly changes as temperature decreases. Given the influence of noise on the shape of the pore size distribution, as described in chapter 3, we conclude that crystals are formed in all pores with a slight preference for the large pores.

In figure 6.17A the measured concentration in mortar is presented. The concentration measured is clearly below the value of the meta-stable $\text{Na}_2\text{SO}_4 \cdot 7\text{H}_2\text{O}$, however the data are too noisy to determine an accurate supersaturation ratio. The low signal to noise ratio can be attributed to the fact that mortar is very dense and does not contain as much solution as the Savoniere stone. Also, during the measurement, the RF pulses damaged the tuning of the Na RF circuit. Figure 6.17B shows the water relaxation time distribution of the mortar sample. In contrast to figure 6.16B, this figure shows clearly that crystallization takes place in the largest pores. This difference can be understood from the measurements on Nucleosils presented above. If the $\text{Na}_2\text{SO}_4 \cdot 7\text{H}_2\text{O}$ phase is formed no dependence of the concentration on the pore size is observed. Therefore in a system having a broad pore size distribution the crystal does not have a preferred pore size in which it crystallizes. On the other hand if mirabilite is formed, it does reveal supersaturation, and it will tend to crystallize in the largest available pore. From the data presented we therefore conclude that mirabilite is formed inside the mortar sample.

The fired-clay brick and calcium silicate brick measurements showed similar results as the Savoniere stone measurements. None of the building material samples revealed supersaturation, which can be understood from the fact that for mirabilite the crystals inside the large pores do not correspond to a significant pressure and $\text{Na}_2\text{SO}_4 \cdot 7\text{H}_2\text{O}$ does not supersaturate at all. Indeed, in these materials no damage was induced during these experiments.

6.5 Discussion

By means of NMR the solubility of various salts inside porous materials has been observed directly. These experiments reveal that supersaturation exists inside porous materials, as was predicted by models based on the crystallization pressure.

For Na_2CO_3 , an increase in solubility is observed for pores of 7 and 10 nm. Based on the measurements a surface tension $\sigma^{cl} = (0.09 \pm 0.02)$ N/m is estimated. Using

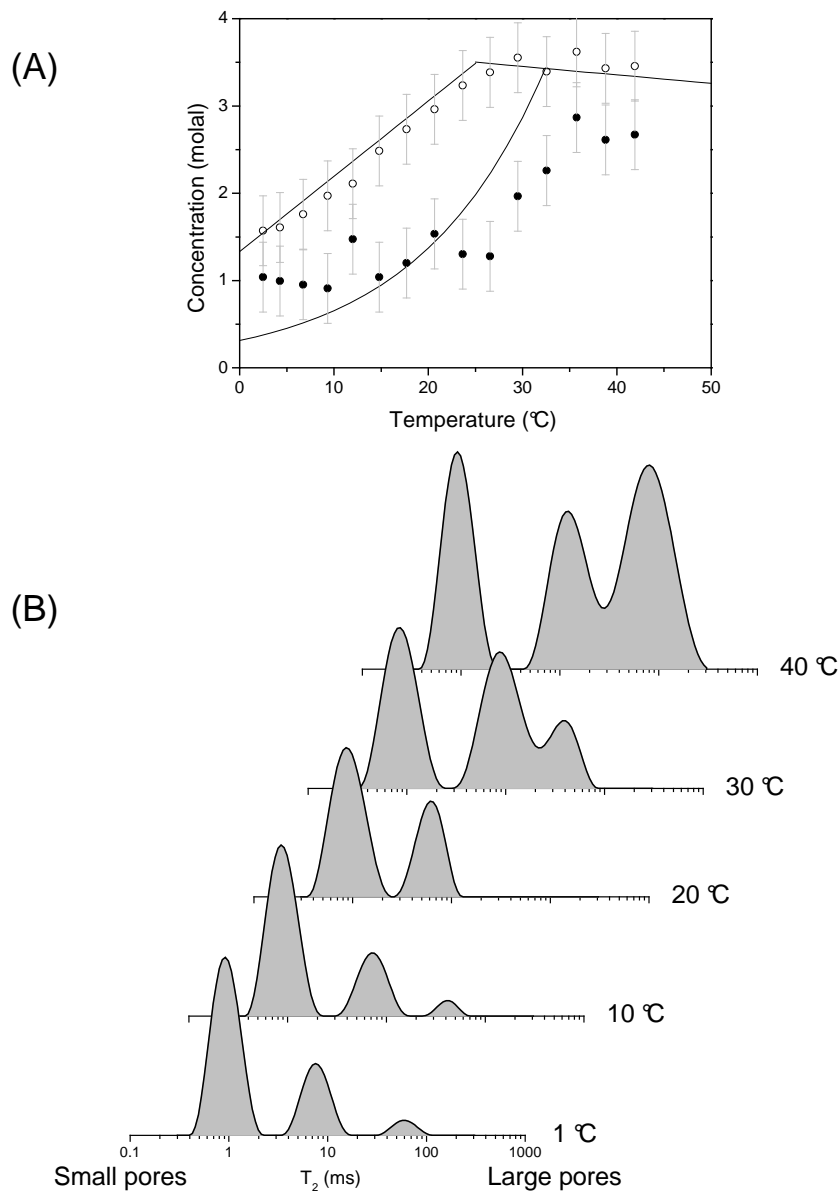


Figure 6.17: (A) Solubility of Na_2SO_4 in bulk solution (\circ) and mortar (\bullet). The solid line represents the literature solubility [Lid98],[Bra71]. (B) Water relaxation time distribution, as a function of temperature in mortar containing Na_2SO_4 solution. It can be seen that as temperature decreases crystallization has taken place in the largest pores (the largest relaxation times).

this value one can calculate the actual damaging pressure caused by Na_2CO_3 :

$$P = 0.04[\text{Pa m}]/r. \quad (6.4)$$

Assuming a typical tensile strength of 3 MPa [Ver97a][Ver97b] this corresponds to a pore radius of about 12 nm, below which the crystallization pressure exceeds the tensile strength of the material.

It is remarkable that for Na_2SO_4 a meta-stable phase is observed. We have tried to create mirabilite but an exact procedure to initiate the transformation is not clear. The only experiment in which mirabilite was formed is an effort to use X-ray diffraction (XRD) to determine the crystal shape. Although the XRD was unsuccessful, the crystal changed during the sample handling procedure. The exact mechanism causing the phase transition is still unclear.

Based on the experiment on Na_2SO_4 in pores of 7 nm, a surface tension of $\sigma^{cl} = (0.10 \pm 0.04)$ N/m can be calculated. Using this value we can calculate the pressure caused by a mirabilite crystal inside a porous material with radius r :

$$P = 0.06[\text{Pa m}]/r, \quad (6.5)$$

which implies that for a tensile strength of 3 MPa damage may be caused in pores having a radius below about 20 nm.

In none of the building materials damage was caused during our experiments. Since one of the issues of this thesis is to investigate the damage potential of crystallization pressure, we will now address this point in more detail. The experiments performed on both building materials and model materials show that the crystallization pressure theory, presented in chapter 2, describes the phenomena observed in these systems. For the model materials the presence of crystallization pressure was shown in a straightforward way by an actual increase in solubility, whereas for the building materials it was deduced from the size of the pores in which crystallization is observed. One should note our experiments only involve a change of temperature, whereas in most building materials in practical situations also transport and drying processes are important. We will now discuss some aspects that might be essential for damage to be caused in these more complex situations.

Let us consider a material having both small and large pores which starts to dry. We assume that at the beginning of the drying process the entire pore volume is saturated with solution and no crystals exist. When salts are present, no receding drying front is observed over a large range of drying speeds [Pel02]. The large pores dry first, after which the small pores dry. The drying speed appears to be a very important parameter. If the drying is very fast, salt is transported, by advection, to the position where the evaporation takes place. This position is usually the material-air interface. At that position salts will be precipitated. Because of capillary action the large pores dry first. At a certain time during this process all large pores have dried and vapor transport starts to dominate the drying process, because no continuous liquid phase exists anymore. From this point on salts crystallize inside the small pores and can result in damage to the material.

The other extreme is slow drying, in which the diffusion of dissolved ions dominates the process. During drying the pore surface of most materials is covered with a liquid film, which applies even to the large pores that are macroscopically empty. Because of this film salts can be transported from the small pores towards large pores where crystallization can take place. In this case no damage is expected.

These two situations are extremes, the actual situation is probably in between. It has, for instance, been observed in fired clay brick that after an initial fast drying, during which salts were transported, the drying rate decreased and salt diffusion equalizes the salt concentration over the sample [Pel04].

The systems considered above consisted of a single material. In practice, however, the systems may consist of different materials, leading to an interaction between different pore systems. As an example, consider a masonry wall which is built from mortar and fired clay brick. As the system dries, the smallest pores are those of the mortar and the largest pores those of the brick. As a consequence the pores of the brick will dry first, and salts are transported into the mortar by diffusion. Once the drying inside the small pores of the mortar starts, the salt content of these pores has been increased compared to the initial salt content, which actually can result in damage. Another example in which similar processes may occur is a substrate covered by a plaster layer with a different pore size distribution [Pet04]. The results presented in this chapter provide a solid framework for studies on these more complicated situations.

7. Sorption measurements on salt contaminated porous media

Abstract

Crystallization of salts in pores is considered as an important cause of weathering of building materials and natural rock. Crystallization pressure, which is an excess pressure in the crystal caused by its surface tension, is one of the proposed mechanisms to explain this weathering. A model is presented to interpret sorption isotherms for porous materials containing salts. Sorption measurements have been performed on Na_2SO_4 and NaCl from which, the surface tension of these salts has been determined as (0.08 ± 0.02) N/m for NaCl and (0.24 ± 0.05) N/m for Na_2SO_4 . The pore size below which these salts reach a damaging pressure is 5 nm for NaCl and 0.1 μm for Na_2SO_4 .

7.1 Introduction

Salts are widely recognized as an important cause of damage of building materials, both modern built structures and cultural heritage. Little is known about the physical mechanisms behind this damage. Various mechanisms have been proposed but none of these has been generally accepted [Cor49][Mor33].

One of the proposed damage mechanisms is based on crystallization pressure [Sch99] [Fla02a]. Crystallization pressure, the excess pressure in a crystal caused by its surface tension is accompanied by an increase of the solubility of the salt inside the porous material. Measurements of the solubility inside porous building materials would yield direct information on crystallization pressure, but are far from trivial. We have successfully applied NMR to measure solubility inside porous materials [Chapter 6]. In practice, the crystallization and dissolution of salt is strongly influenced by the humidity of the environment. Because the environmental humidity has a cyclic nature the crystallization and dissolution process will have this as well. During periods of low humidity, water evaporates and salts crystallize. When the humidity is high water condenses and crystals dissolve. To obtain more information on these processes we have studied the water vapor adsorption in porous media contaminated with salts. In this chapter we focus on the question how the water

vapor uptake is influenced by the pore size r and the kind of salt. We describe the thermodynamic background of these sorption experiments and present experimental results on NaCl , Na_2SO_4 , and Na_2CO_3 in well defined porous media.

In section 7.2 the thermodynamic background of the experiments is described. In section 7.3 we discuss the materials and the methods used in the experiments. In section 7.4 and 7.5 the results of measurements on bulk salts and salts in porous materials are presented. Finally, in section 7.6 we study implications of the results for the weathering processes.

7.2 Theory

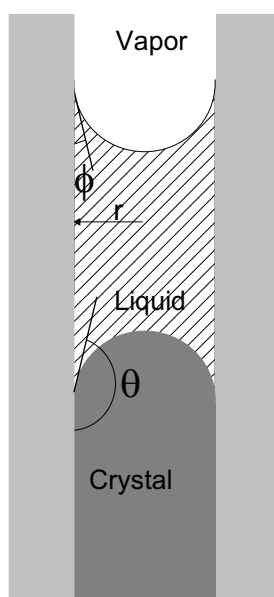


Figure 7.1: *A schematic overview of the system under study: vapor in equilibrium with a salt solution inside a porous material. In the solution crystals can be present.*

In this chapter we study the sorption of water vapor in a porous material in which salts are present. A schematic overview of the system is given in figure 7.1. A pore is shown in which a solution and possibly a crystal reside. The pore is assumed to be cylindrical with a radius r . For the theoretical analysis the presence of the crystal is not essential. The water in the solution in the pore is in equilibrium with the water in the vapor. Our aim is to describe the relation between the relative humidity RH , the salt concentration C in the solution, and the pore radius r . The relative humidity is defined as

$$RH \equiv \frac{\tilde{p}^v}{\tilde{p}_0^v} \times 100\%, \quad (7.1)$$

where \tilde{p}^v and \tilde{p}_0^v are the water vapor pressure and the saturation vapor pressure of bulk water, respectively¹.

7.2.1 Thermodynamic approach

For our purpose we only have to consider the liquid (*l*) (or solution) and vapor (*v*) phase. These phases are in thermodynamic equilibrium and the temperature is constant ($dT = 0$). For each phase the Gibbs-Duhem equation holds; for the vapor phase it is given by:

$$-N_w^v d\mu_w^v + V^v dp^v = 0, \quad (7.2)$$

and for the liquid phase it reads:

$$-N_w^l d\mu_w^l - N_s^l d\mu_s^l + V^l dp^l = 0. \quad (7.3)$$

In these equations N_i^j (moles) is the number of particles of species *i* (*w* = water, *s* = salt) in phase *j*, μ (J/mol) is the chemical potential, V (m³) the volume, and p (Pa) the pressure.

In the absence of salt, bulk liquid water is assumed to be in equilibrium with a water vapor with partial vapor pressure \tilde{p}_0^v . In equilibrium, liquid water does not have the tendency to evaporate nor does the vapor have the tendency to condense, hence \tilde{p}_0^v is the vapor pressure corresponding to a *RH* of 100 %. Both the presence of salt ($C > 0$) and the pore-size alter the *RH* value at which water condenses.

Influence of the salt concentration

First, we discuss the influence of the salt concentration. By combining the equations 7.2 and 7.3 and using the fact that in equilibrium the chemical potentials of water in the vapor and liquid phase are equal, we arrive at the following relation:

$$\frac{V^v}{N_w^v} dp^v = \frac{V^l}{N_w^l} dp^l - \frac{N_s^l}{N_w^l} d\mu_s. \quad (7.4)$$

Next we substitute $\nu_w^l \equiv V^l/N_w^l$, $\nu_w^v \equiv V^v/N_w^v$ and $\chi C = N_s^l/V^l$, in which ν_w^l is the molar volume of water in the liquid phase², ν_w^v the molar volume of water in the vapor phase, C the concentration of the salt in the solution and $\chi \equiv 10^3$ [l/m³]. This factor χ is a consequence of using [M \equiv mol/l] as unit for the concentration instead of [moles/m³]. Further we use the following expression [Kat65]

$$d\mu_s = \tilde{v}_s^l dp^l + nRT d \ln(a), \quad (7.5)$$

¹In order not to generate more complex symbols than strictly necessary we write \tilde{p}^v instead of \tilde{p}_w^v , because the water vapor is the only changing vapor pressure.

²Here it is implicit assumed that ν_w^l is constant. In practice this value might slightly depend upon the salt concentration, but this dependence is neglected in the present analysis.

in which \tilde{v}_s^l (m³/mole) is the partial molar volume of the salt in the solution, a (M) the activity of the salt in the solution, and n the number of ions per unit of salt (for instance 2 for NaCl and 3 for Na₂SO₄). The mechanical pressure on the liquid does not change by adding the salt, therefore $dp^l = 0$. Now Eq. 7.4 can be rewritten as:

$$\nu_w^v dp^v = -\chi C \nu_w^l n RT d \ln a. \quad (7.6)$$

The activity can be written as $a \equiv \gamma^\pm C$, in which γ^\pm is the mean activity of the salt, which is a function of C at high salt concentrations where the solution can not be considered ideal. Equation 7.6 can be rewritten as:

$$\nu_w^v dp^v = -\chi \nu_w^l n RT \left(1 + \frac{C}{\gamma^\pm(C)} \frac{d\gamma^\pm(C)}{dC} \right) dC. \quad (7.7)$$

We use the ideal gas law to write the molar volume of the vapor ν_w^v as RT/\tilde{p}^v , in which \tilde{p}^v is the vapor pressure of the water. Note that the pressure in the vapor phase only changes due to variations of the water vapor density and thus $dp^v = d\tilde{p}^v$. Now we can integrate Eq. 7.7 as follows:

$$\int_{\tilde{p}_0^v}^{\tilde{p}_s^v} \frac{RT}{\tilde{p}^v} d\tilde{p}^v = - \int_0^C \chi \nu_w^l n RT \left(1 + \frac{C'}{\gamma^\pm(C')} \frac{d\gamma^\pm(C')}{dC'} \right) dC'. \quad (7.8)$$

We define a correction X (Molar), which accounts for the non-ideality of the solution:

$$X \equiv \int_0^C \frac{C'}{\gamma^\pm(C')} \frac{d\gamma^\pm(C')}{dC'} dC'. \quad (7.9)$$

For salts which mean activities γ^\pm are known, the correction term $\chi n RT X$ can be calculated numerically. The results of such a calculation for NaCl, Na₂CO₃, and Na₂SO₄ are presented in figure 7.2. After integration of Eq. 7.8 we obtain the following expression:

$$RT \ln \left(\frac{\tilde{p}_s^v}{\tilde{p}_0^v} \right) = -\chi n RT \nu_w^l (C + X). \quad (7.10)$$

Note that the right hand side of this expression is the osmotic pressure of the solution and the $\chi n RT X$ accounts for the non ideality of the solution. Equation 7.10 shows that, the equilibrium partial vapor pressure of the system is lowered by adding salt, i.e., salts promote vapor condensation at lower RH values. Generally, when a salt is involved, the word condensation is replaced by deliquescence.

Influence of the pore size

Next a solution, with a salt concentration C is placed inside a porous material, which is assumed to contain cylindrical pores with radius r . In mathematical terms this means that the pore radius is changed from infinity to r . We start the calculation with equation 7.4. When the solution-vapor interface is located inside a pore, it

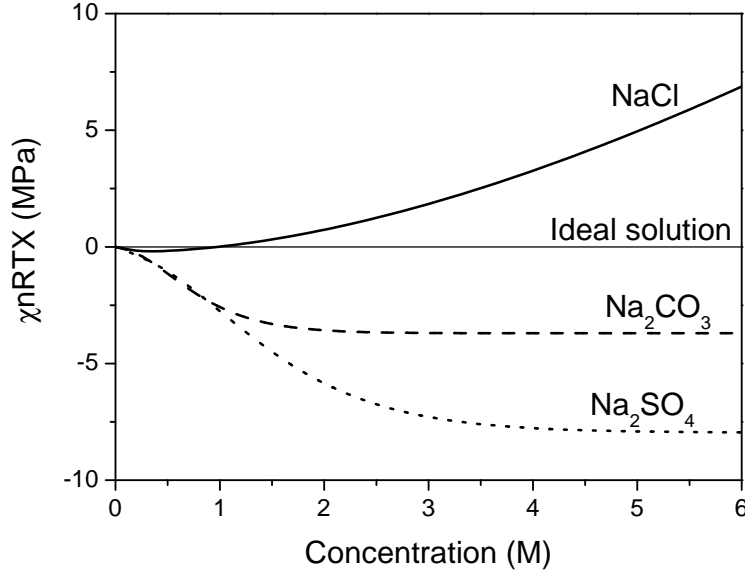


Figure 7.2: The correction term for the osmotic pressure $\chi nRTX$ (MPa), for NaCl , Na_2CO_3 , and Na_2SO_4 . Activity data are taken from [Lid98], [Rod01]

becomes curved due to the fact that water preferentially wets the surface. This curvature modifies the expression for mechanical equilibrium:

$$p^v - p^l = \frac{2\sigma^{lv} \cos \phi}{r}, \quad (7.11)$$

where σ^{lv} is the surface tension of the liquid-vapor interface, and ϕ the contact angle between the pore surface and the liquid phase. To simplify the notation, we define $B \equiv \sigma^{lv} \cos \phi$, which is a constant. Further we replace $2/r$ by J . Now equation. 7.11 can be written as

$$dp^l = dp^v - BdJ. \quad (7.12)$$

We can use this equation to substitute dp^l in Eq. 7.4 and use eq. 7.5 to substitute $d\mu_s$, yielding the result:

$$[\nu_w^v - \nu_w^l(1 - \chi C \tilde{v}_s^l)] dp^v = -\nu_w^l(1 - \chi C \tilde{v}_s^l) BdJ. \quad (7.13)$$

Generally $\chi C \tilde{v}_s^l$ is smaller than unity. Compared to the molar volume of the vapor phase, the molar volume of the liquid phase can be neglected. A typical value for water is $1.8 \times 10^{-5} \text{ m}^3$ for the molar volume of the liquid phase, whereas for the vapor phase (assuming it behaves as an ideal gas) this is $22.6 \times 10^{-3} \text{ m}^3$. As a consequence $\nu_w^l(1 - \chi C \tilde{v}_s^l)$ can be neglected compared to ν_w^v at the left hand side of Eq. 7.13. We use the ideal gas law to write the molar volume of the vapor as $\nu_w^v = RT/\tilde{p}^v$. Again the only vapor pressure that changes is the water vapor

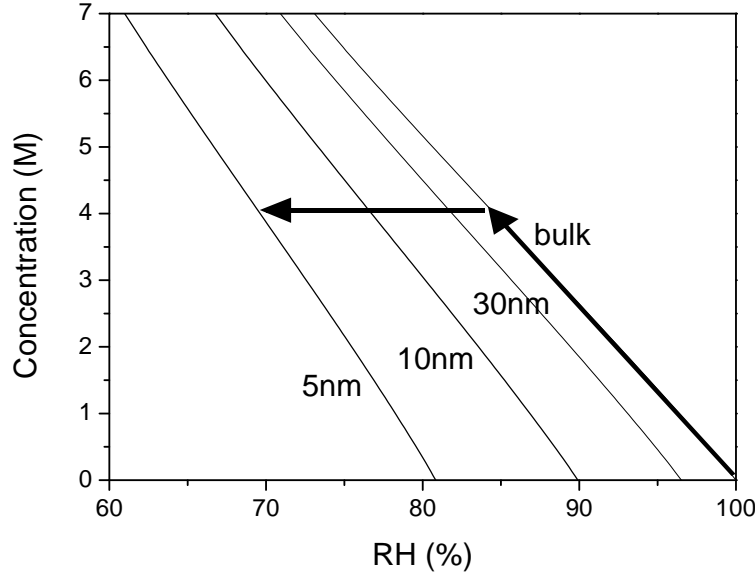


Figure 7.3: *Equilibrium between a salt solution with concentration C inside cylindrical pores with radius r and the relative humidity RH . The arrows indicate the path along which the integration in the section 7.2.1 is performed.*

pressure, hence $dp^v = d\tilde{p}^v$. The integral describing the effect of reducing the pore radius from infinity (bulk) to r is now written as

$$\int_{\tilde{p}_s^v}^{\tilde{p}^v} \frac{RT}{p^v} dp^v = - \int_0^{2/r} \nu_w^l (1 - \chi C \tilde{v}_s^l) B dJ. \quad (7.14)$$

Integration of Eq. 7.14 leads to:

$$RT \ln \left(\frac{\tilde{p}^v}{\tilde{p}_s^v} \right) = -\nu_w^l (1 - \chi C \tilde{v}_s^l) B \frac{2}{r}. \quad (7.15)$$

At the right hand side two terms can be identified: $2\nu_w^l B/r$, which shows the influence of the pressure on the water, and $-2\nu_w^l C \tilde{v}_s^l B/r$, which corrects for the change of ν_w^l caused by the salt.

7.2.2 Salt and porous material

Next, we consider the actual system of interest: a salt solution in a pore. We can simply sum the equations 7.10 and 7.15, because the integrations over C (Eq. 7.8) and r (Eq. 7.14) can be done separately. This results in:

$$RT \ln \left(\frac{\tilde{p}^v}{\tilde{p}_0^v} \right) = -\chi n RT \nu_w^l (C + X) - \nu_w^l (1 - \chi C \tilde{v}_s^l) \sigma^{lv} \frac{2}{r} \cos \phi. \quad (7.16)$$

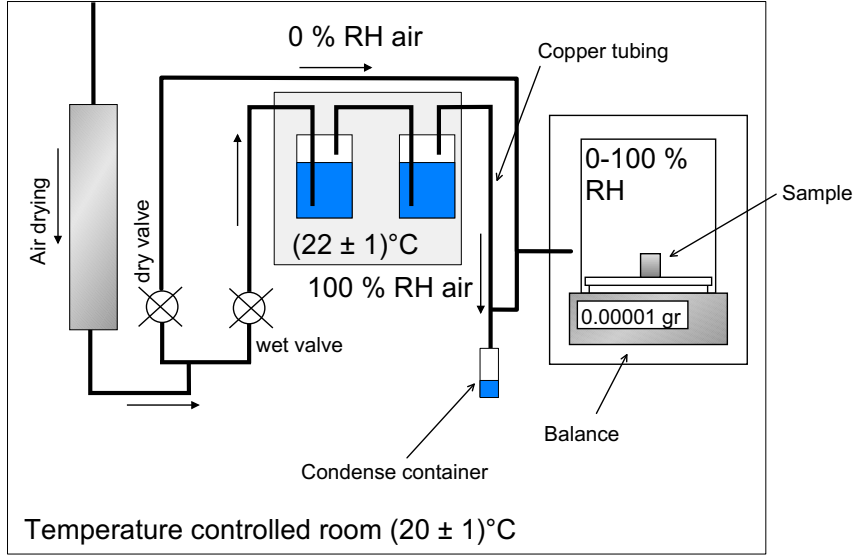


Figure 7.4: Schematic view of the experimental setup. A balance is placed in a temperature controlled room, and the relative humidity inside the weighing room is controlled.

This equation gives the value of the relative humidity ($\tilde{p}^v/\tilde{p}_0^v$) which is in equilibrium with a solution of concentration C inside pores with radius r . The integration procedure is illustrated in figure 7.3 for NaCl. The arrows indicate the integration path used to obtain equation 7.16. As can be seen a solution of 4 M NaCl inside pores with a radius of 5 nm will be in equilibrium with a relative humidity of 70%. When the relative humidity exceeds this value, water vapor will condense and the solution will be diluted. The concentration will drop to a lower value, which corresponds to a higher RH value.

Two different condensation regimes can be distinguished. First, at low salt concentrations capillary forces dominate the condensation behavior of the liquid. It follows from Eq. 7.16 that capillary condensation dominates the behavior as long as the following criterion is satisfied:

$$\frac{\chi n R T \nu_w^l (C + X)}{(1 - \chi C \tilde{v}_s^l)} \ll \nu_w^l \sigma^{lv} \frac{2}{r} \cos \phi. \quad (7.17)$$

In this regime equation 7.16 reads

$$R T \ln (\tilde{p}^v / \tilde{p}_0^v) = -\nu_w^l \sigma^{lv} \frac{2}{r} \cos \phi, \quad (7.18)$$

At higher salt concentrations the osmotic forces might dominate the condensation behavior. In that particular case equation 7.16 reads

$$-\ln \left(\frac{\tilde{p}^v}{\tilde{p}_0^v} \right) = n \chi \nu_w^l (C + X). \quad (7.19)$$

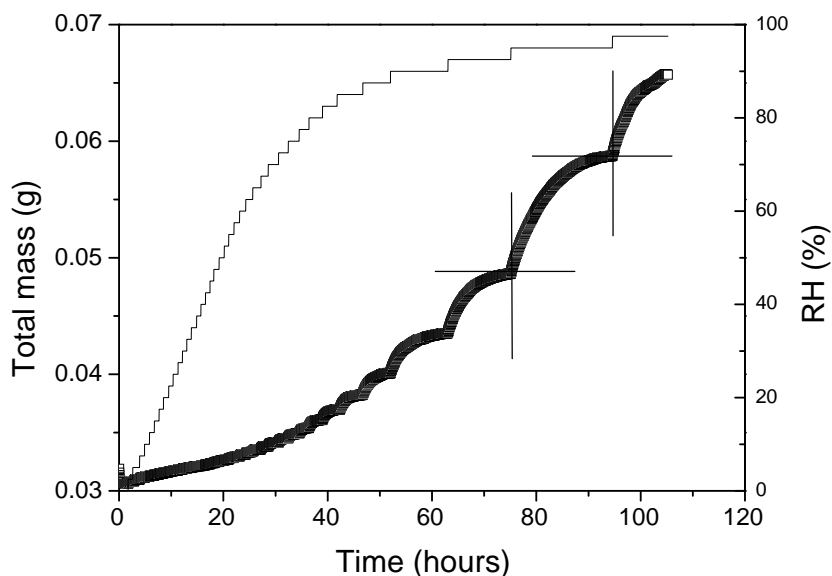


Figure 7.5: *Typical sorption measurement for a 0.03 g sample of 10 nm Nucleosil (\square). The solid line segments represent the RH set-points (right axis). An RH value is set and the control program waits until equilibrium is reached, as illustrated by the crosses in the figure. Next, the set point is changed to a new value. This procedure is repeated automatically until the last RH set point has been processed. The final data points for each RH value are used for the isotherm.*

7.3 Materials and Methods

A schematic overview of the setup used to measure the sorption isotherms is given in figure 7.4. A balance is placed inside a room which is temperature controlled at $(20 \pm 1)^\circ\text{C}$. The use of small samples is preferred because in that case only a small amount of water needs to be absorbed. As a result equilibrium is established much faster. The balance in our setup has a sensitivity of 0.01 mg, which enables us to measure a sorption isotherm in about 4 to 10 days. The air inside the weighing chamber is kept at a constant RH as follows. Air is first dried in a membrane air dryer. To ensure that the air is fully dry it passes through a cylinder containing silica drying grains. The air is at 0 % RH after that treatment. Next the air flow is divided in two fractions by two valves. The setting of these valves determines the final RH . One of these fractions stays dry whereas the other flows through several wash bottles to be fully wetted. The last three wash bottles are kept 2°C above the temperature of the room, and hence some excess water will evaporate into the air. The air then flows through a copper tube, in which its temperature is lowered to $(20 \pm 1)^\circ\text{C}$ again. As a result some water condenses in this tube. This water flows towards a condense container. This air flow is now at 100 % RH . Next the wet

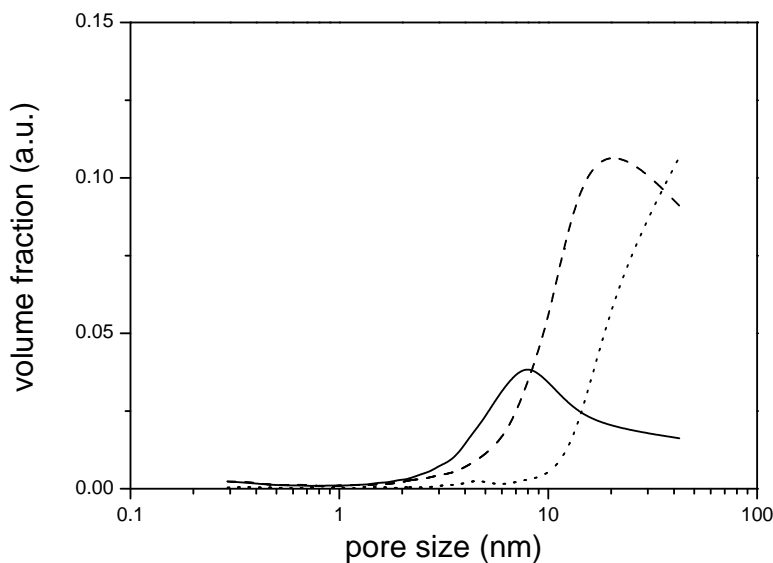


Figure 7.6: *Volumetric pore size distributions of Nucleosil samples with pores of 7 nm (solid line), 10 nm (dashed line), and 30 nm (dotted line), determined by capillary condensation experiments. The cut off at 42 nm corresponds to a relative humidity of 97.5 % and hence is the maximum pore size that can be determined by this technique.*

and dry air fractions are mixed. The final RH values were checked by means of a psychrometer and were found to correspond to the desired value set by the valves within 1 %. This air flows into the balance room where the sample is positioned. To avoid capillary condensation in the pores of the weighing table, we have constructed a platinum table. Tests indicated that platinum, in contrast to other materials tested, does not adsorb water. Due to vapor condensation problems in the tubes and the balance, the maximum RH value that can be used in experiments is limited to 98 % RH . The valves are controlled by a computer, which also reads the weight given by the balance.

An isotherm consists of mass data at various relative humidities. Each of these data points must reflect an equilibrium situation. Usually it takes some time before equilibrium is reached. During this time measurements are performed to monitor the stabilization process. Once the mass does not change anymore for a preset number of measurements, it is assumed that equilibrium is reached. An example of this monitor function is given in figure 7.5. The actual sorption isotherm consists of the final data points for each RH value. Each data point is obtained by flowing air for 60 s through the weighing room and then waiting 30 s for the balance to stabilize, without flow. Next the mass is read. The measurement of an isotherm is fully controlled by the computer, it sets the relative humidity, the flow, and measures

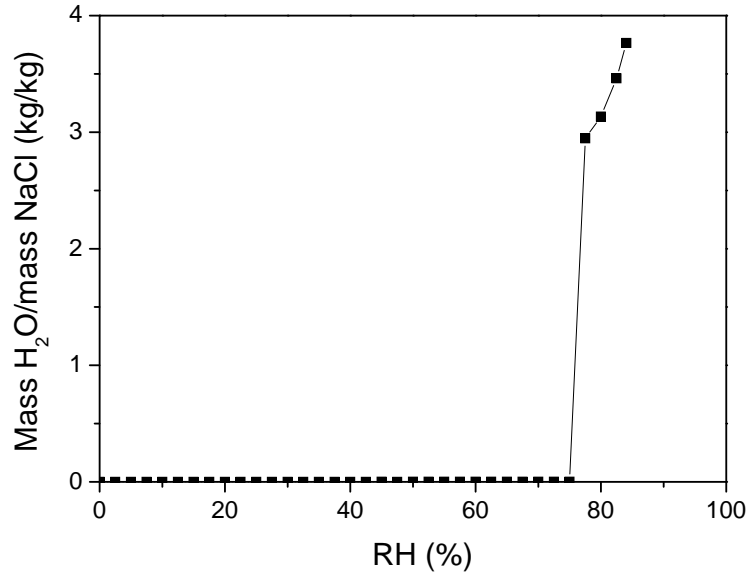


Figure 7.7: Measured sorption isotherm of NaCl at 20 °C. At RH = 75 % the salt transforms into a salt solution. Above this point the solution is diluted when the RH increases.

the mass. When equilibrium is established, it switches to a new RH value. In this way the measurements are performed very efficiently. In all experiments presented in this chapter the RH was varied from 0 % to 97.5 % in 39 steps.

We have performed our experiments with a model porous material called *Nucleosil*. This is a dried silica gel that is produced with a well defined pore size. Both clean and salt-contaminated samples were measured. The sorption isotherm can be used to obtain the pore size distribution of a clean material using equation 7.18. Figure 7.6 shows the pore size distributions obtained this way for the 3 Nucleosils (7, 10, and 30 nm) used in our study ($\sigma^{lv} = 0.072$ N/m, and $\phi = 0^\circ$). The distribution stops at 42 nm. This corresponds to a relative humidity of 97.5 %, which is typically the maximum set point used in the experiments.

7.4 Bulk salts

In this section we will discuss the behavior of bulk salts. The salts used in this study, are NaCl, Na₂SO₄ and Na₂CO₃. These were also used in chapter 6 of this thesis. In the following section, measurements of salt inside a porous material will be presented.

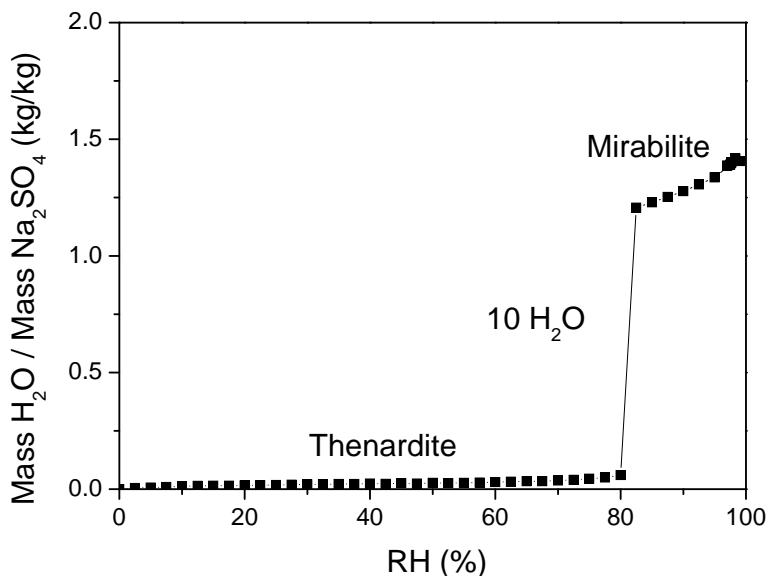


Figure 7.8: Sorption isotherm of Na_2SO_4 at 20°C . The step is the hydration transition from an anhydrous crystal (thenardite) to a decahydrated crystal (mirabilite). Deliquescence is not observed.

NaCl

The sorption isotherm of NaCl is plotted in figure 7.7. It can be seen that the isotherm has no distinct feature for $RH < (75 \pm 2.5)\%$. The model explained in section 7.2 describes the equilibrium situation between a salt solution, with concentration C and the RH . In our experiments the RH is set, therefore the concentration of the solution will move to the value determined from Eq. 7.10. Before $RH = 75\%$ this concentration is above the solubility of the salt, therefore the salt remains in the crystal form. At $RH = 75\%$ the concentration, in equilibrium with the RH is lower than the solubility and hence the salt dissolves by water uptake. This is called the point of deliquescence, which is in agreement with values reported in literature, [Rod99a][Bla01]. This RH value corresponds to a concentration of (6.3 ± 1.0) M using Eq. 7.16. Within experimental error, this concentration agrees with the literature value for the solubility, i.e. 5.5 M [Lid98]. The salt concentration can also be determined by the masses of the salt and the water, doing so a concentration of 5.5 molal is found. This agrees within experimental error as well. Above the point of deliquescence the concentration of the salt solution decreases as the RH increases, as described in Eq. 7.10. Because the diluting process is very slow, the measurement was stopped at an RH of 85 % instead of the usual 97.5 %.

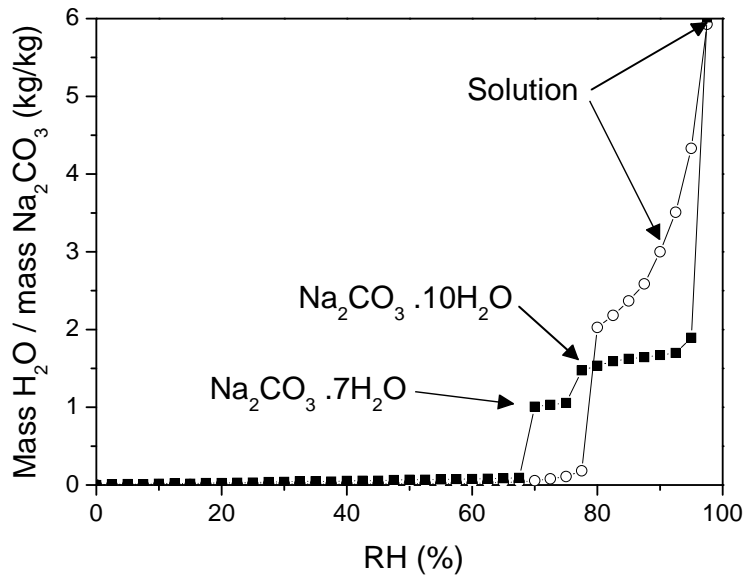


Figure 7.9: Sorption isotherm of Na_2CO_3 (\circ) and dried $\text{Na}_2\text{CO}_3 \cdot 10\text{H}_2\text{O}$ (\blacksquare) at 20°C . The dry Na_2CO_3 transforms in solution at $\text{RH} = 80\%$, whereas the original $\text{Na}_2\text{CO}_3 \cdot 10\text{H}_2\text{O}$ transforms in various hydration states and dissolves at higher RH .

Na_2SO_4

Until now we have discussed the sorption measurement for NaCl , which has one crystal structure (Halite) at 293 K . Other salts, for instance Na_2SO_4 , can adopt various crystal structures, which differ in their degree of hydration. In figure 7.8 the measured sorption isotherm of Na_2SO_4 is plotted. A hydration transition can be seen at $\text{RH} = 80\%$. Per mole of salt about 9.6 moles of water are absorbed, hence we conclude that the crystal transforms from Na_2SO_4 into $\text{Na}_2\text{SO}_4 \cdot 10\text{H}_2\text{O}$. This sorption isotherm does not show deliquescence at all. Our model predicts this should happen at an RH of 95.7% . After the experiment did not show deliquescence at 97.5% the salt was exposed to an RH of 98% but still did not dissolve.

The transition from thenardite (Na_2SO_4) to mirabilite ($\text{Na}_2\text{SO}_4 \cdot 10\text{H}_2\text{O}$), i.e., the hydration of the crystal, is recently studied by Rodriguez-Navarro and Doehne [Rod00a]. They claim that in an ESEM experiment they have observed that the salt first dissolves, after which precipitation of mirabilite takes place. In principle this can be explained by Eq. 7.10. The solubility of thenardite and mirabilite is 3.5 molal and 1.3 molal [Lid98], respectively, which corresponds to an RH of 87.3% and 95.7% . If their claim is correct the hydration transition should take place at 87.3% . Our experiment, however, shows the hydration transition at $\text{RH} = 80\%$ which is significantly lower. This might suggest that the proposed mechanism, dissolution followed directly by precipitation, does not apply to our experiments.

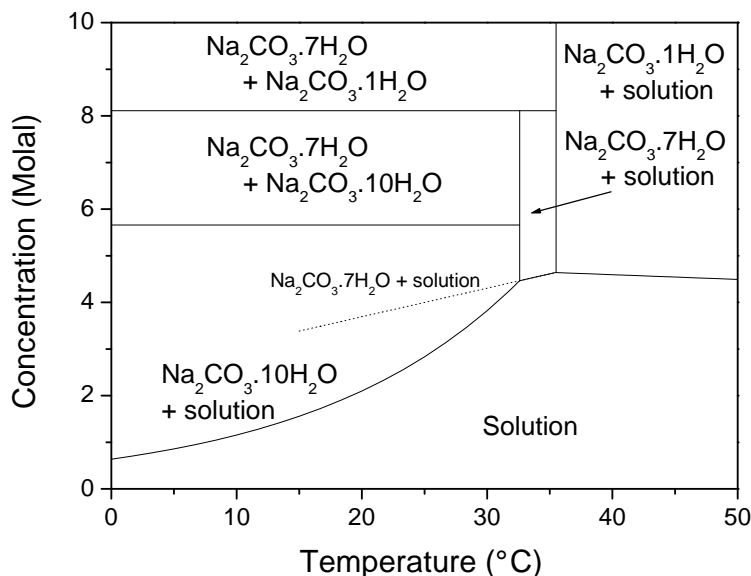


Figure 7.10: Phase diagram of Na_2CO_3 [Lid98] [Ull03]. Our experiments have been performed at 20°C .

Na_2CO_3

Two sorption isotherms for Na_2CO_3 are plotted in figure 7.9. One isotherm is measured on Na_2CO_3 which was manufactured as Na_2CO_3 crystals. The other isotherm is measured on $\text{Na}_2\text{CO}_3 \cdot 10\text{H}_2\text{O}$ crystals which were dried during the sorption experiment at $RH = 0\%$. For the Na_2CO_3 crystals deliquescence is observed at an RH between 77.5% and 80% . The other salt ($\text{Na}_2\text{CO}_3 \cdot 10\text{H}_2\text{O}$), which was dried for approximately 2 hours at the beginning of the experiment behaves quite differently. It shows two hydration transitions at 70% and 77.5% , respectively and deliquescence at $RH = 97.5\%$.

The original Na_2CO_3 crystals do not reveal hydration transitions, whereas the salt which was hydrated before the drying step of the experiment does hydrate again later on. A possible explanation of this behavior is that the drying of the hydrous crystal leaves behind a "porous" crystal, which can be easily penetrated by water vapor later in the experiment. For the Na_2CO_3 crystals, this is not the case and perhaps an outer layer hydrates, but not the entire crystal. Hydration of the outer layer cannot be observed in our measurement, because the amount of water adsorbed to the outer surface is very small. The fact that a solution is formed which is supersaturated with respect to the hydrous salt indicates that nucleation of the hydrous crystal is difficult.

From the measurement on the Na_2CO_3 crystals the concentration at the point of deliquescence is found to be 4.7 molal, determined from the salt mass and water

mass. According to our model, this corresponds to $RH = 80\%$, the value that is actually observed. This concentration is above the solubility of $\text{Na}_2\text{CO}_3 \cdot 7\text{H}_2\text{O}$ and $\text{Na}_2\text{CO}_3 \cdot 10\text{H}_2\text{O}$. Both phases are not observed in this experiment which suggests that these are hard to form.

In the other experiment, deliquescence of $\text{Na}_2\text{CO}_3 \cdot 10\text{H}_2\text{O}$ occurs at $RH = 95\%$. Based on the phase diagram our model predicts a value of 92% . We hypothesize that the deviation of the deliquescence point is caused by an interfacial layer of air around the sample which is less humid than the environment. The effect that the actual deliquescence does not take place at exactly the expected RH value is also observed by for instance Doehne [Doe04], who needs a fan inside his environmental SEM to obtain deliquescence at the right RH . In our experiment, however, a fan would disturb the measurement of the mass of the samples accurately. This might also explain why the deliquescence of Na_2SO_4 was not observed in our experiments.

7.5 Salt in a porous material

In this section, measurements are presented on model porous materials contaminated with salts. The salt was brought into the porous material by placing the material in a droplet of salt solution. Because of capillary action the pores fill with fluid. Then the water evaporates and the salt is precipitated. Because the mass of the material is known, and the mass of the material with the salt is known, the total amount of salt is known for each experiment.

NaCl

The sorption isotherms of Nucleosil with a pore size of 7 nm, both with and without NaCl, are shown in figure 7.11. As can be seen, capillary condensation of the water occurs at RH values below the point of deliquescence of the bulk salt. The sharp transition at $RH \approx 80\%$ observed in the measurement is due to salts outside the porous material. The sorption isotherm predicted by our model is calculated by using equation 7.16. We have used a constant concentration equal to the bulk solubility (6.3 M). Although the result of this calculation (dashed curve) describes the data fairly well, it is systematically lower. A better calculation can be obtained as follows. An essential parameter in Eq. 7.16 is the solubility. In chapter 2 we have derived that for an anhydrous crystal inside an unsaturated porous material the solubility is given by:

$$C = C_0 \exp \left(\frac{\nu_s^c}{nRT} \left[\sigma^{cl} \cos \theta - \left(1 - \frac{\tilde{\nu}_s^l}{\nu_s^c} \right) \sigma^{lv} \cos(\phi) \right] \frac{2}{r} \right). \quad (7.20)$$

Here C_0 is the bulk solubility, and σ^{cl} and θ are the surface tension and contact angle of the crystal liquid interface, respectively. So the point at which the concentration C in equilibrium with the imposed RH becomes smaller than the solubility now depends on the pore size. The pore size distribution is known (figure 7.6), hence we

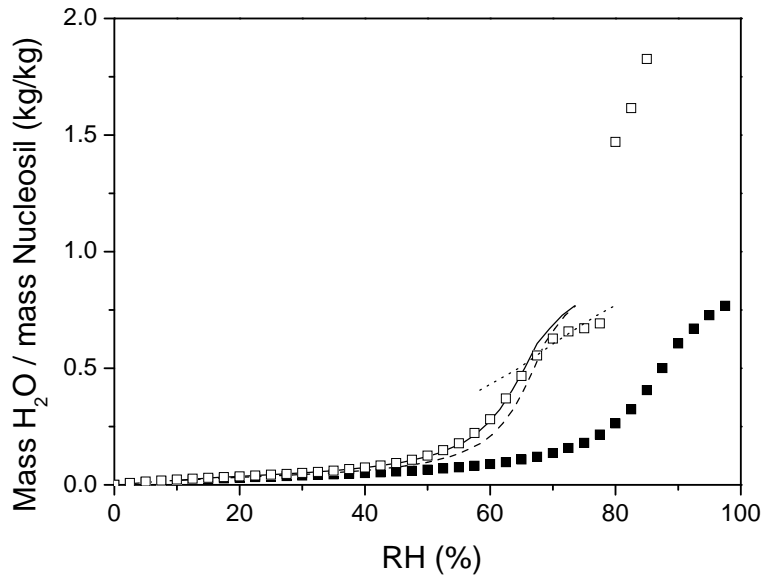


Figure 7.11: *Sorption isotherm of 7 nm Nucleosil, both without (■) and with a NaCl contamination (□). The dashed curve is the predicted sorption isotherm using the bulk solubility. The solid curve is a prediction using a pore size dependent solubility, see Eq. 7.20 ($\sigma^{cl} = (0.08 \pm 0.02) \text{ N/m}$). The dotted curve represents the sorption isotherm for a pore system which does not contain crystals. In this case sorption implies dilution of the solution. The jump in the data at $RH \approx 80\%$ can be attributed to bulk NaCl outside the pores. The size of the symbols reflects the error of the experimental data.*

can, if we know σ^{cl} , determine a solubility distribution. With this, and equation 7.16 a sorption isotherm can be calculated (solid curve). Because σ^{cl} is not known, we use this as a fitting parameter. The solid curve in figure 7.11 was calculated using $\sigma^{cl} = (0.08 \pm 0.02) \text{ N/m}$, which value yielded the best description of the experimental data. This results in a solubility increase compared to the bulk of a factor 1.2 and hence a pressure of about 2.3 MPa is exerted on the porous material. This pressure is lower than the typical tensile strength of 3 MPa [Ver97a][Ver97b] of most building materials.

It can be seen that the curve starts to deviate from the experimental data at a relative humidity of approximately 67.5 %. This can be explained by the fact that above this value all crystals are dissolved. Therefore further sorption leads to a dilution of the solution. We know the total amount of salt in the system and we can estimate the amount of salt outside the Nucleosil from the sharp deliquescence jump. We have used the difference of these amounts to calculate the sorption isotherm of the solution in the pores in the absence of crystals (dotted curve). Above $RH = 67\%$ this prediction is in good agreement with the data.

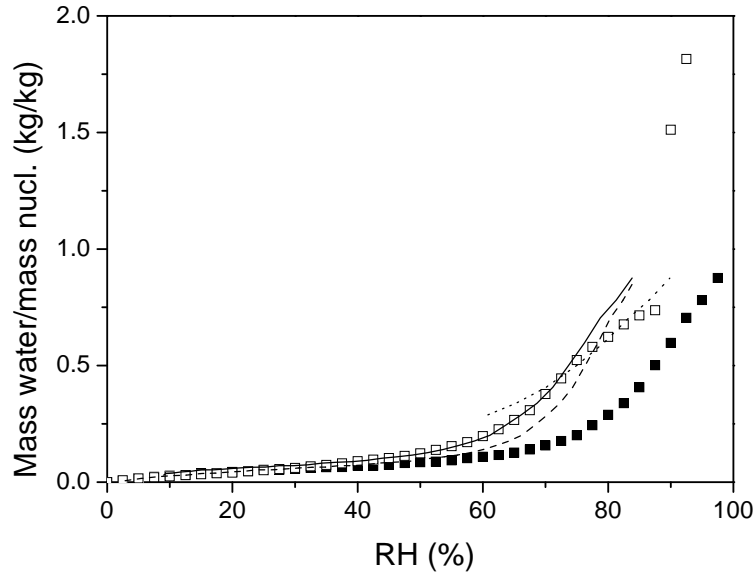


Figure 7.12: Sorption isotherm of clean 7 nm Nucleosil (■) and 7 nm Na_2SO_4 contaminated Nucleosil (□). The dashed curve is the sorption isotherm predicted using the bulk solubility concentration. The solid curve is a prediction using a pore size dependent solubility, see Eq. 7.20 ($\sigma^{cl} = (0.24 \pm 0.05) \text{ N/m}$). The dotted curve represents the sorption isotherm for a pore system which does not contain crystals. In this case sorption implies dilution of the solution. As can be seen, for $RH < 75\%$ the measured isotherm is governed by the pore size dependent solubility, whereas at a higher RH the isotherm indicates that all salt has dissolved. The jump in the data at $RH \approx 87\%$ can be attributed to salt outside the pores.

Na_2SO_4

The sorption isotherms of Nucleosil with pore size 7 nm, both with and without Na_2SO_4 , are plotted in figure 7.12. The transition at an RH of 87.5 % corresponds to the dissolution of thenardite (anhydrous Na_2SO_4) present outside the pores. With Eq. 7.16 a RH of 87 % is predicted, which is equal to the observed value within the experimental accuracy. The solution is supersaturated with respect to mirabilite, which suggests that no mirabilite is formed. The presence of thenardite reveals that in the drying stage of the sorption experiment this phase is formed directly from the solution. If first mirabilite would be precipitated, and this was dehydrated, similar to the bulk hydrous Na_2CO_3 experiment discussed in section 7.4, a "porous" crystal would have formed, which would hydrate during the sorption experiment.

A calculation was performed using the bulk solubility for thenardite (dashed curve) which describes the data fairly well, although it is systematically lower. This indicates that the solubility of the thenardite is increased significantly within the

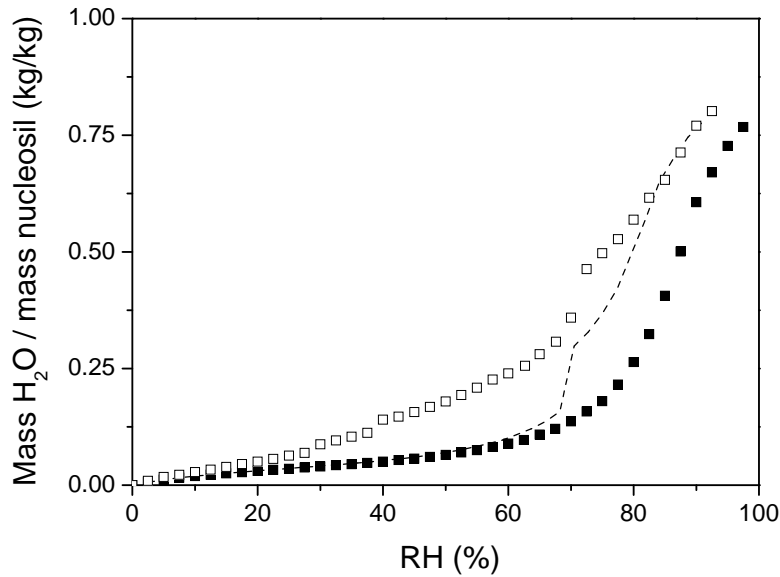


Figure 7.13: *Sorption isotherm of clean 7 nm Nucleosil (■) and 7 nm Na₂CO₃ contaminated Nucleosil (□). The dashed curve is a simulated sorption isotherm which contains the hydration transitions but assumes no supersaturation.*

pores. Therefore a calculation was performed using a pore size dependent solubility for thenardite (using Eq. 7.20). The results are represented by the solid curve. It can be seen that the latter describes the measured data very good up to approximately 75 %. The resulting value for the surface tension σ^{cl} equals (0.24 ± 0.05) N/m. In order to determine the pressure also the liquid-vapor interface is taken into account. The resulting pressure on the pore wall is of the order of 48 MPa. This pressure is an order of magnitude larger than the typical tensile strength of building material (3 MPa, [Ver97a],[Ver97b]), which shows that crystallization of thenardite could be very damaging. Above 75 % the calculated isotherm deviates from the experimental data data. Following the same procedure as for NaCl we have calculated the sorption isotherm of the solution in the pores in the absence of crystals (dotted curve). Above 75 % this calculation matches the data fairly well.

Na₂CO₃

The sorption isotherms of Nucleosil with pore size 7 nm, both with and without Na₂CO₃ are plotted in figure 7.13. The dashed curve represents a simulation incorporating the bulk solubility and hydration as determined from the bulk experiments, described in section 7.4. Hence the effect of the pores on both the concentration and the hydration is neglected. It is clear that this does not give a satisfactory description of the data, partly because no supersaturation has been taken into account.

Because the isotherm contains a hydration transition (at $RH = 70\%$) and hydration transitions are not incorporated in our model, the amount of supersaturation has not been established from the present data.

7.6 Discussion

A thermodynamic model was derived which describes sorption isotherms for porous materials containing salt. By interpreting the experimental sorption isotherms in terms of this model the crystal phase that is formed can be identified.

Assuming that hydration transitions occur via a dissolution/precipitation process, our model predicts certain values for the relative humidity at which these transitions should occur. The actual hydration transitions, however, are observed at lower RH values than predicted. This raises some doubt whether the dissolution/precipitation process is actually taking place.

For NaCl and Na₂SO₄ within pores an increase in the solubility compared to the bulk is observed. For Na₂CO₃ the data also suggest such an increase, but it can not be quantified. An analysis of the data for NaCl and Na₂SO₄ results in values for the crystal-liquid surface tension of these salts being (0.08 ± 0.02) N/m for halite and (0.24 ± 0.05) N/m for thenardite.

It is interesting to notice that during the drying of the 7 nm pore sample contaminated with Na₂SO₄, thenardite is precipitated directly from the solution. This can be concluded from the fact that deliquescence takes place at an RH value corresponding to the solubility of thenardite. Hence no hydration has taken place. Apparently, formation of the hydrous crystal phase inside the porous material is difficult. This was also observed in the NMR experiments on Na₂SO₄ discussed in chapter 6.

The values found for the surface tension of halite (NaCl) and thenardite (Na₂SO₄) indicate that, if these salts crystallize in small pores, they can cause damage to the porous material, and hence can be responsible for salt weathering. The pore size below which these salts reach a typical pressure of 3 MPa is 5.2 nm for halite and 100 nm for thenardite. So for building materials having pores of the order of 100 nm and smaller (like concrete, calcium silicate brick, mortar) precipitation of thenardite can be damaging. The damage potential of the crystallization pressure of NaCl is much smaller, because very small pores are needed for this mechanism to cause damage.

8. Concluding remarks

One of the main topics in this thesis is salt crystallization in porous materials. In small pores salt crystals are under pressure because of their surface tension. This pressure can cause damage to the material, and is accompanied by an increase in the solubility of the salt. In literature discussing salt damage this increase is often referred to as supersaturation. Figure 8.1 shows a schematic diagram of the work on this topic presented in this thesis. Two phenomena play a role: supersaturation of salt inside pores and capillary condensation. In this thesis the combined action of both phenomena is described with a thermodynamical model. This model describes the situation in actual building materials more accurately than the existing models, which only describe one aspect of the actual situation. Measurements on a series of model porous materials were performed by two independent techniques: Nuclear Magnetic Resonance (NMR) and sorption. For the first time, the increase in solubility within the pores of a material was measured. Interpretation of these results in terms of our theoretical model confirms the existence of a potentially damaging pressure inside porous materials.

Nuclear Magnetic Resonance (NMR) proved to be a powerful tool to determine the concentration of a salt solution inside a porous material. By quantitative measurements of the amount of both Na and H in the solution inside a material, the salt concentration can be determined. A supersaturation, if present, shows up directly in the measurements. Both the H and Na NMR signal decay give additional information about the pore sizes in which the solution resides. However, the use of the Na signal decay is limited by the fast bulk relaxation rate of Na. When performing Na NMR, care has to be taken that the ions in the solution are in the fast modulation regime. If this is not the case, loss of Na signal may occur and a calibration is needed for quantitative measurements.

The NMR experiments reveal that an increase in solubility indeed exists inside porous materials. For Na_2CO_3 , a significant increase in solubility is observed for pores of 7 and 10 nm. Based on the measurements a crystal-liquid surface tension $\sigma^{cl} = (0.09 \pm 0.02)$ N/m is estimated for $\text{Na}_2\text{CO}_3 \cdot 10\text{H}_2\text{O}$. Assuming a typical tensile strength of 3 MPa [Ver97a], our model predicts that in pores with a radius smaller than about 12 nm the crystallization pressure exceeds the tensile strength of the material. For Na_2SO_4 the meta-stable $\text{Na}_2\text{SO}_4 \cdot 7\text{H}_2\text{O}$ phase is observed. The solubility of this phase does not show any dependence on the pore size. This suggests that this meta-stable phase has no surface tension, $\sigma^{cl} = 0$, and hence this

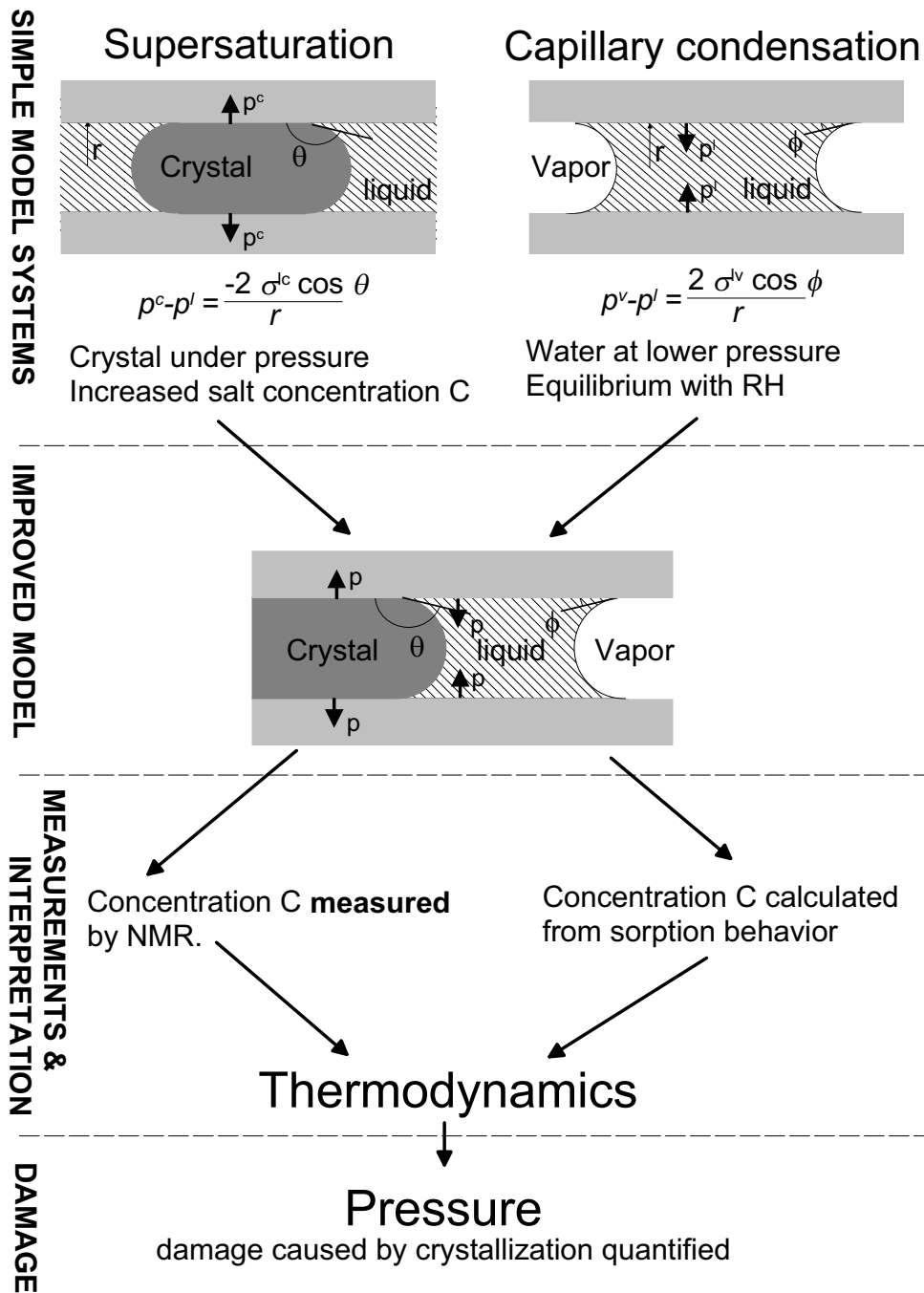


Figure 8.1: Overview of the work on salt crystallization presented in this thesis. From two theoretic models a new, more realistic, model was constructed. Two different types of measurements were performed onto this model system. Interpretation of these measurements gives an estimate of the damage caused by salts inside porous materials.

crystal cannot cause damage. In one experiment the stable $\text{Na}_2\text{SO}_4 \cdot 10\text{H}_2\text{O}$ phase was formed. In pores of 7 nm this phase reveals a significant increase in solubility. Our estimate for the surface tension is $\sigma^{cl} = (0.10 \pm 0.04)$ N/m. Damage can be caused in pores with a radius smaller than ~ 20 nm.

Besides the model porous materials, experiments were done with building materials and Na_2SO_4 , showing the meta-stable $\text{Na}_2\text{SO}_4 \cdot 7\text{H}_2\text{O}$ phase in Savoniere stone, calcium silicate brick, and fired clay brick. In these materials the salt does not reveal an increase in solubility, and hence does not have a preferred pore size to crystallize in. This supports the idea that $\text{Na}_2\text{SO}_4 \cdot 7\text{H}_2\text{O}$ has a very low surface tension and cannot cause damage. In mortar $\text{Na}_2\text{SO}_4 \cdot 10\text{H}_2\text{O}$ was found, and the salt crystallizes in the largest pores. This can be a consequence of the surface tension of the crystal, which promotes crystal growth in the bigger pores.

In addition to the NMR experiments also sorption measurements were performed. Compared to NMR the sorption measurement is somewhat indirect. Supersaturation could be observed for small pores (order 7 nm), but for large pores the technique is rather insensitive, in contrast to NMR. The experiments show an increased solubility for NaCl ($\sigma^{cl} = (0.08 \pm 0.02)$ N/m, damage in pores with $r < 5$ nm) and thenardite (anhydrous Na_2SO_4 , $\sigma^{cl} = (0.24 \pm 0.05)$ N/m, damage in pores with $r < 100$ nm).

The behavior of Na_2SO_4 shows some peculiar characteristics. We observed that nucleation of $\text{Na}_2\text{SO}_4 \cdot 10\text{H}_2\text{O}$ is difficult in the temperature induced supersaturation experiments. The sorption experiments reveal that the solution inside the pores is governed by the solubility of anhydrous Na_2SO_4 , and supersaturated with respect to $\text{Na}_2\text{SO}_4 \cdot 10\text{H}_2\text{O}$. Nevertheless the latter phase does not precipitate. Hence nucleation of $\text{Na}_2\text{SO}_4 \cdot 10\text{H}_2\text{O}$ is difficult. Compared to $\text{Na}_2\text{SO}_4 \cdot 10\text{H}_2\text{O}$ the nucleation of $\text{Na}_2\text{SO}_4 \cdot 7\text{H}_2\text{O}$ is easy.

Outlook

For future research a number of issues are still open. First of all, for materials that do not have such small pores as the model materials discussed in this thesis the crystallization pressure can not explain the damages that are actually observed. It is known that fired clay brick, for instance, experiences structural damages because of salt crystallization, but the pores are too large to explain these damages by crystallization pressure.

The NMR crystallization experiments presented in this thesis prove that crystallization pressure exists, but in these temperature induced crystallization experiments the damage potential is low. In practice, however, also transport of salt occurs, for instance, during wetting and drying. Drying experiments during which it is monitored in which pores crystallization takes place, might be essential to describe the full damage potential of crystallization pressure.

Besides drying, it would also be interesting to investigate the dynamics of the crystallization process itself. The experiments presented in this thesis always involve equilibrium. Little is known, both theoretically as well as experimentally, about the dynamics of crystallization and the evolution of forces exerted by the crystal on the

pore wall during this process. Research on the dynamics of the crystallization process also might include verification of the existence of a non equilibrium crystallization pressure, which vanishes when equilibrium is reached (theoretically described by [Ste04]).

NMR seems to be the best technique to study these processes. With NMR also spatial information inside the material can be obtained, revealing possible gradients in moisture and ion content. In addition, a pore size distribution of the material as a function of position can be obtained and transport phenomena can be observed.

Appendix A: Phase Diagrams & Salt Data

NaCl

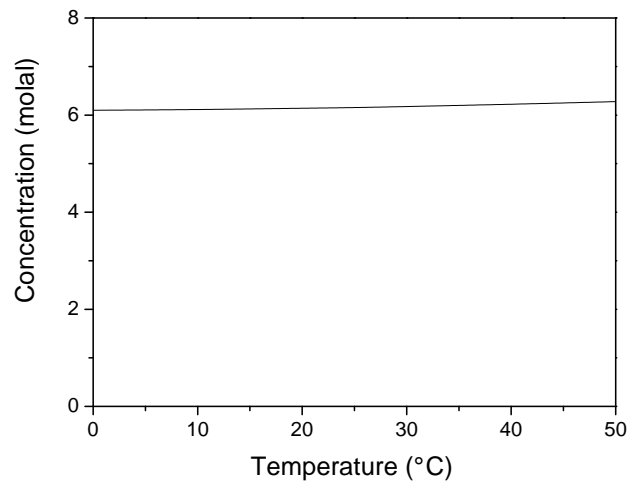


Figure 8.2: *Phase diagram of NaCl*

Table 8.1: *Data of NaCl*

\tilde{v}_s^l	$21.3 \cdot 10^{-6} \text{ m}^3/\text{mol}$
ν_s^c	$24.5 \cdot 10^{-6} \text{ m}^3/\text{mol}$

Na₂CO₃

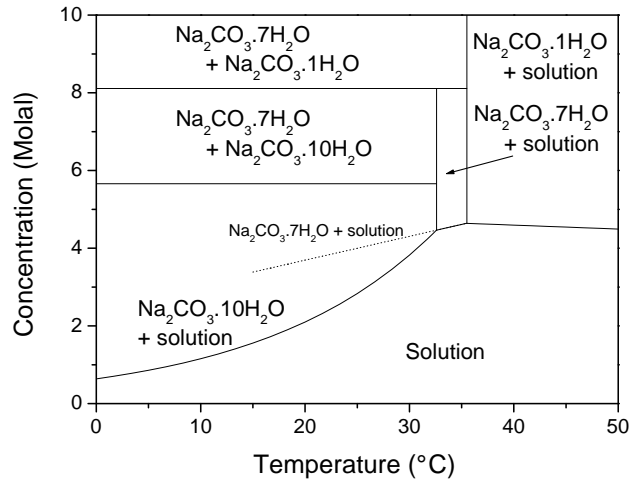


Figure 8.3: *Phase diagram of Na₂CO₃*

Table 8.2: *Data of Na₂CO₃*

ν_s^c (Na ₂ CO ₃)	$41.7 \cdot 10^{-6} \text{ m}^3/\text{mol}$
ν_s^c (Na ₂ CO ₃ ·10H ₂ O)	$195 \cdot 10^{-6} \text{ m}^3/\text{mol}$
ν_w^c (Na ₂ CO ₃ ·10H ₂ O)	$19.5 \cdot 10^{-6} \text{ m}^3/\text{mol}$
ν_s^c (Na ₂ CO ₃ ·1H ₂ O)	$55.1 \cdot 10^{-6} \text{ m}^3/\text{mol}$
ν_w^c (Na ₂ CO ₃ ·1H ₂ O)	$5.5 \cdot 10^{-6} \text{ m}^3/\text{mol}$
\tilde{v}_s^l	$23.3 \cdot 10^{-6} \text{ m}^3/\text{mol}$

Na₂SO₄

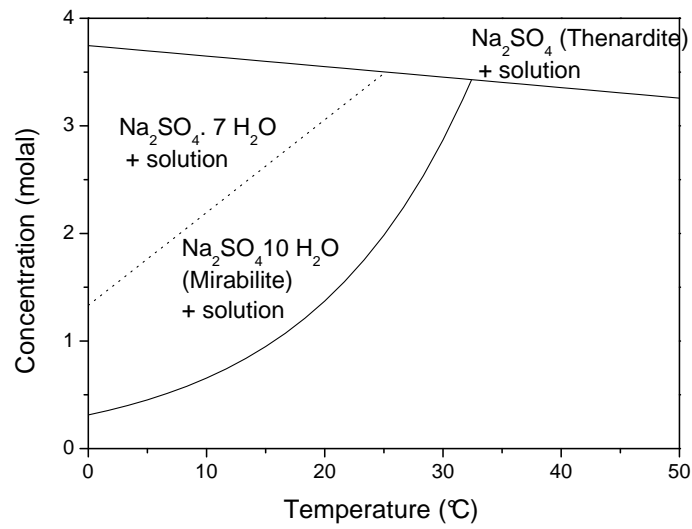


Figure 8.4: *Phase diagram of Na₂SO₄*

Table 8.3: *Data of Na₂SO₄*

ν_s^c (Na ₂ SO ₄)	$52 \cdot 10^{-6} \text{ m}^3/\text{mol}$
ν_s^c (Na ₂ SO ₄ ·10H ₂ O)	$220 \cdot 10^{-6} \text{ m}^3/\text{mol}$
ν_w^c (Na ₂ SO ₄ ·10H ₂ O)	$22 \cdot 10^{-6} \text{ m}^3/\text{mol}$
$\tilde{\nu}_s^t$	$34.8 \cdot 10^{-6} \text{ m}^3/\text{mol}$

Appendix B: List of symbols

σ^{ij}	surface tension of the ij interface [N/m]
ν_j^i	molar volume of specie j in phase i [m ³ /mol]
γ^\pm	Mean activity coefficient
$a = \gamma^\pm C$	Activity [molar]
\tilde{v}_s^l	Partial molar volume of salt in solution [m ³] [Kat65]
χ	1000 l/m ³ , factor as a consequence of using molar=mol/l for the concentration instead of mol/m ³
C	Concentration [molar]
C_0	Bulk saturation concentration [molar]
V^i	Volume of phase i [m ³]
θ	Contact angle between crystal and pore wall, as defined in figure 2.1
ϕ	Contact angle between liquid and pore wall, as defined in figure 2.6
$J = 2/r$	Two divided by the pore radius r [m ⁻¹]
r	Pore radius [m]
μ_j	Chemical potential of species j [J/mole].
A	$-\sigma^{cl} \cos \theta$
B	$\sigma^{lv} \cos \phi$
F	$A - B(1 - \nu_w^l/\nu_w^c - \tilde{v}_s^l/\nu_s^c)$
TE	Echo time [s]
TR	Repetition time [s]
T_1	Longitudinal relaxation time [s]
T_2	Transverse relaxation time [s]
D	Diffusion coefficient [m ² /s]
f	Frequency [Hz]

Bibliography

- [Abr61] A. Abragam: *The principles of nuclear magnetism*, Clarendon, London (1961).
- [Ada60] A.W. Adamson: *Physical chemistry of surfaces*, 2nd edition, Wiley Interscience, Chichester (1960).
- [Ada94] O.C.G. Adan: *On the fungal defacement of interior finishes*, Ph.D. Thesis, Eindhoven University of Technology, Eindhoven, 1994.
- [Atk02] P. Atkins, J. de Paula: *Physical chemistry*, seventh Edition, Oxford University Press, Oxford (2002).
- [And61] W.A. Anderson: *Electric current shims for correcting magnetic field*, Rev. Sci. Instrum. **32**, 241-250 (1961).
- [Bar03] F. Barberon, J.P. Korb, D. Petit, V. Morin, E. Bermejo: *Probing the surface area of a cement-based material by nuclear magnetic resonance relaxation dispersion*, Phys. Rev. Lett. **90**, 116103 (2003).
- [Bec16] G.F. Becker, A.L. Day: *Note on the linear force of growing crystals*, Journal of geology **4**, 313-333 (1916).
- [Bla01] C. Bläuer Böhm, A. Kung, K. Zehnder: *Salt crystal intergrowth in efflorescence on historic buildings*, Chimia **55**, 996-1001 (2001).
- [Bra71] O. Braitsch: *Salt Deposits: their origin and composition*, Springer, New York, 1971.
- [Bro79] K.R. Brownstein, C.E. Tarr: *Importance of classical diffusion in NMR studies of water in biological cells*, Phys. Rev. A. **19**, 2446-2453 (1979).
- [Bru13] W. Bruhms, W. Meckelenburg: *Über die sogenannte "kristallisationskraft"*, 6. jahresbericht d. Niedersächischen geologischen vereins, 92-115, (1913).
- [Blo48] N. Bloembergen, E.M. Purcell, R.V. Pound: *Relaxation effects in Nuclear Magnetic Resonance Absorption*, Phys. rev. **73** 7, 679-712 (1948).
- [Cor49] C.W. Correns: *Growth and dissolution of crystals under linear pressure*, Disc. Faraday. Soc. **5**, 267-271 (1949).
- [Doe04] E. Doehne: Private communication.

-
- [Doe02] E. Doehne: *Salt weathering, a selective review*, In *Natural Stone, Weathering phenomena, Conservation Strategies and Case Studies* by S. Siegesmund, T. Weis, A. Vollbrecht, The Geological Society London: London, 2002, p 51-64.
- [Diu93] W. Duttlinger and D. Knöfel: *Salzkristallisation und Salzschadensmechanismen* in Jahresberichte Steinzerfall - Steinconservierung, Verlag Ernst & Sohn, Berlin (1993).
- [Eis66] M. Eisenstadt, H.L. Friedman: *Nuclear magnetic resonance in ionic solution. I. Relaxation of ^{23}Na in Aqueous solutions of NaCl and NaClO₄*, J. Chem. Phys. **44**, 1407-1415 (1966).
- [Eva86] R. Evans, U. Marini Bettoli Marconi, P. Tarazone: *Fluids in narrow pores: Adsorption, capillary condensation and critical points*, J. Chem. Phys. **84**, 2376-2399, (1986).
- [Eva69] I. S. Evans: *Salt crystallization and rock weathering*, Rev. Géomorphol. Dyn. XIX **4**, 153-177 (1969-70).
- [Fla02a] R.J. Flatt: *Salt damage in porous materials: how high supersaturations are generated*, Journ. of Crystal growth **242**, 435-454 (2002).
- [Fla02b] R.J. Flatt: *Hydration pressure: a bad case of crystallization pressure*, SALTeXPERT Workshop, prague (2002).
- [God01] S. Godefroy, J.-P. Korb, M. Fleury, R.G. Bryant: *Surface nuclear magnetic relaxation and dynamics of water and oil in macroporous media*, Phys. Rev. E **64**, 20606 (2001).
- [Goo03] E.L.J. Goosens: *Moisture transfer properties of coated gypsum*, Ph.D. Thesis, Eindhoven University of Technology, Eindhoven, 2003.
- [Gou97] A. Goudie, H. Viles: *Salt weathering hazards*, John Wiley and sons, New York (1997).
- [Hah50] E.L. Hahn: *Spin echoes*, Phys. Rev., **80**, 580-594 (1950)
- [Hal89] W.P. Halperin, F. D’Orazio, S. Bhattacharja, T.C. Tarczon, *Magnetic resonance relaxation analysis of porous media*, in "Molecular dynamics in restricted geometries" (J. Klafter and J.M. Drake), pp 311-350, John Wiley and sons, New York (1989).
- [Her96] Herodotus: *Histories*, Wordsworth Editions Limited, Herfordshire (1996).
- [Hur01] M. D. Hürlimann: *Diffusion and relaxation effects in general stray field NMR experiments*, Journal of Magnetic Resonance **148**, 367-378, (2001).

-
- [Igl97] A. La Iglesia, V. González, V. López-Acevedo, C. Viedma: *Salt crystallization in porous construction materials I Estimation of crystallization pressure*, Journ. of Crystal Growth **177** (1997) 111-118.
- [Kat65] A. Katchalsky, P.F. Curran: *Nonequilibrium thermodynamics in biophysics*, Harvard University Press, Cambridge, Massachusetts (1965).
- [Kop55] H. Kopp: *Über die bildung von krystallen mit kernen*, Ann. Chem. Pharm. **44** 124 (1855).
- [Kop94] K. Kopinga, L. Pel: *One-dimensional scanning of moisture in porous materials with NMR*, Rev. Sci. Instrum. **65**, 3673-3681 (1994).
- [Ken97] A.P.M. Kentgens: *A practical guide to solid-state NMR of half integer quadrupolar nuclei with some applications to disordered systems*, Geoderma **80**, 271-306 (1997).
- [Lav53] M. Lavallo: *Recherches sur la formation de cristaux á la température ordinaire*, Compt. Rend. Acad. Sci. **34**, 493-495 (1853).
- [Lid98] D.R. Lide, *CRC Handbook of chemistry and physics*, CRC Press LLC, Boca Raton, Florida (1998).
- [Lob89] V.M.M. Lobo, J.L. Quaresma: *Handbook of electrolyte solutions part B*, Elsevier, Amsterdam (1989).
- [Mei63] L. Meites (editor): *Handbook of analytical chemistry*, 1st edition, McGraw-Hill book company inc. London (1963).
- [Mey28] R.J. Meyer (editor): *Gmelins Handbuch der anorganische Chemie*, Verlag Chemie GMBH Weinheim/Bergstr. 1928.
- [Mor33] H. Mortensen: *Die "Salzsprengrung" und ihre bedeutung für die regional-klimatische gliederung der wüsten*, Petermanns Geographische Mittheilungen **5-6**, 130-135 (1933)
- [Pel95] L. Pel: *Moisture transport in porous buidling materials*, PhD Thesis, Eindhoven University of Technology, Eindhoven (1995).
- [Pel02] L. Pel, H. Huinink, K. Kopinga: *Ion transport and crystallization in historical objects as studied by NMR*, Appl. Phys. letters **81**, 2893-2895 (2002).
- [Pel04] L. Pel, H.P. Huinink, K. Kopinga, R.P.J. van Hees, F. Zezza :*Ion transport and crystallization in fired-clay brick: A NMR study*, Proceedings of the 13th Internatinal Brick and Block Masonry Conference, Amsterdam, July 2004
- [Pet04] J. Petkovic, L. Pel, H.P. Huinink, K. Kopinga, R.P.J. van Hees: *Salt transport in plaster/substrate layers: A nuclear magnetic resonance study* Proceedings of the 13th Internatinal Brick and Block Masonry Conference, Amsterdam, July 2004

-
- [Por01] P. Porion, M. Al Mukhtar, S. Meyer, A.M. Faugere, J.R.C. van der Maarel, A. Delville: *Nematic Ordering of suspensions of charged anisotropic colloids detected by ^{23}Na Nuclear Magnetic resonance*, J. Phys. Chem. B **105**, 10505-10514 (2001).
- [Pro82] S.W. Provencher: *A constrained regularization method for inverting data represented by linear algebraic or integral equations*, Comput. Phys. Comm. **27**, 213-229 (1982).
- [Put01] A. Putnis, G. Mauthe: *The effect of pore size on cementation in porous rocks*, Geofluids **1**, 37-41 (2001).
- [Rij04] L.A. Rijniers, P.C.M.M. Magusin, H.P. Huinink, L. Pel, K. Kopinga: *Sodium NMR relaxation in porous materials* J. magn. res. **167**, 25-30, (2004).
- [Rod98] C. Rodriguez-Navarro: *Evidence of honeycomb weathering on Mars*, Geophys. Res. Lett. **25**, 3249-3252 (1998).
- [Rod99a] C. Rodriguez-Navarro, E. Doehne: *Salt weathering: influence of the evaporation rate, supersaturation and crystallization pattern*, Earth Surface Processes and Landforms **24**, 191-209 (1999).
- [Rod99b] C. Rodriguez-Navarro, E. Doehne: *Time-lapse video and esem: integrated tool for understanding processes in situ*, American laboratory **31**, 28 - 35 (1999).
- [Rod00a] C. Rodriguez-Navarro, E. Doehne, E. Sebastian: *How does sodium sulfate crystallize? Implications for the decay and testing of building materials*, Cement and Concrete research **30**, 1527-1534 (2000).
- [Rod01] E. Rodil, J.H. Vera: *Measurement and correlation of the activity coefficients of individual ions in aqueous electrolyte solutions of Na_2SO_4 and K_2SO_4* , Canadian Journ. of Chem. Engineering **79**, 771-776 (2001).
- [Roe03] S. Roels, J. Carmeliet, H. Hens: *Modelling unsaturated moisture transport in heterogeneous limestone*, Transport in porous media **52**, 333-350 (2003).
- [Ste04] M. Steiger: *Crystal growth in porous materials: I. The crystallization pressure of large crystals* Submitted to Journal of Crystal Growth
- [Sch99] G.W. Scherer: *Crystallization in pores*, Cement and Concrete research **29**, 1347-1358 (1999).
- [Sch01] G.W. Scherer, R. Flatt, G. Wheeler: *Materials science research for the conservation of sculpture and monuments*, MRS Bulletin, Januari 44-50 (2001).
- [Sli90] C.P. Slichter, "Principles of magnetic resonance", Springer, New York (1990).
- [Tab16] S. Taber: *The growth of crystals under external pressure*, American Journal of Science **41**, 532-556 (1916).

-
- [Tho62] Thomson: *Phil. Mag.* 1862, 24, p 395
- [Tsu03] N. Tsui, R.J. Flatt, G.W. Scherer: *Crystallization damage by sodium sulfate*, *Journ. of Cultural Heritage* **4**, 109-115 (2003).
- [Ull03] M. Bohnet et al. (editors): *Ullmann's Encyclopedia of Industrial Chemistry*, 7th edition, John Wiley & Sons, New York (2003).
- [Val01b] R.M.E. Valckenborg: *NMR on technological porous materials*, Ph.D. Thesis, Eindhoven University of Technology, Eindhoven (2001).
- [Val01c] R. Valckenborg, L. Pel, K. Hazrati, K. Kopinga and J. Marchand: *Pore water distribution in mortar during drying as determined by NMR*, *Materials and Structures* **34**, 599-604 (2001).
- [Val02] R.M.E. Valckenborg, L. Pel, K. Kopinga: *Combined NMR cryoporometry and relaxometry*, *J. Phys. D. Appl. Phys.* **35**, 249-256 (2002).
- [Val02a] R.M.E. Valckenborg, H.P. Huinink, J.J.v.d. Sande, K. Kopinga: *Random-walk simulations of NMR dephasing effects due to uniform magnetic-field gradients in a pore*, *Phys. Rev. E* **65**, 021306 (2002).
- [Ver97a] A.T. Vermeltoort: *Properties of Some Clay Bricks Under Varying Loading Conditions*, *Masonry International* **10**, No 3, 85-91 (1997).
- [Ver97b] A. Vervuurt: *Face fracture in concrete*, Ph.D. Thesis, TU Delft, Delft (1997).
- [Vla96] M.T. Vlaardingerbroek, J.A. den Boer: *Magnetic resonance imaging*, second edition, Springer, New York (1999).
- [Web85] H. Weber: *Steinconservierung: der leitfaden zur konservierung und restaurierung von natursteinen* Expert Verlag (1985).
- [Woe01] D.E. Woessner: *NMR relaxation of spin 3/2 nuclei: Effects of structure, order, and dynamics in aqueous heterogeneous systems*, *Concepts magn. reson.* **13**(5), 294-325 (2001).
- [Yeh95] J.Y. Yehng: *Microstructure of wet cement pastes: a nuclear magnetic resonance study*, Ph.D. Thesis, North-western University, Chicago (1995).
- [Zeh89] K. Zehnder, A. Arnold: *Crystal growth in salt efflorescence*, *Journ. of Crystal growth* **97**, 513-521 (1989).

Curriculum Vitae



Lourens Albert Rijniers
Charlevillehof 16
5627 DH, Eindhoven
The Netherlands

Tel.: (+31)-(0)40 2375665
E-Mail: lourens@rijniers.nl

Date of birth: 02-11-1975, Hengelo(o)
The Netherlands

- 1988-1994 VWO (Atheneum diploma), Jeroen-Boschcollege te 's-Hertogenbosch
- 1994-2000 Applied physics at Eindhoven University of Technology
Graduation project entitled *NMR Relaxation Measurements on H and Na in porous Media*, supervisors: dr.ir. L.Pel and prof.dr.ir. K.Kopinga.
- 2000-2004 Ph.D. research at Eindhoven University of Technology
Department of applied physics, group *Transport in permeable media* of prof.dr.ir. K.Kopinga

Dankwoord

Tijdens mijn promotie onderzoek heb ik veel hulp van anderen ontvangen waarvoor ik dankbaar ben. Zonder iemand tekort te willen doen wil ik een aantal mensen met naam bedanken voor hun hulp:

Pieter Magusin voor de hulp bij het begrijpen van quadrupolen en het mogen meten in zijn lab, De bedrijfsgroep laboratorium automatisering voor de support van de PhyDAS hardware, Peter Mutsaers voor de VxWorks steun (ook al gebruiken we het niet meer), Nick Lousberg voor zijn hulp bij het doen van microporbe analyses, Marc van Maris voor de FEGSEM opnames van Nucleosil, Coen Smits voor zijn hulp bij de XRD experimenten, Peter Nouwens voor het leveren van Ultra Pure water, Jan Millenaar voor zijn daadkracht op diverse terreinen en Gerrie Baselmans voor de diverse adviezen.

Bijzonder was de samenwerking met de faculteits werkplaats waar niet alleen dingen voor mij werden gemaakt, maar ik ook zelf kon leren omgaan met draaibanken en freesmachines, Frank, Henk, Han, Ginny, Jan en Marius bedankt hiervoor.

Mijn STW gebruikerscommissie wil ik bedanken voor de leerzame vergaderingen en de goede suggesties. In het bijzonder wil ik Rob van Hees bedanken voor zijn belangstelling en ideeën voor mijn onderzoek ook buiten de gebruikerscommissie. Het Center for Building and Systems (KCBS) wil ik bedanken voor onder andere het bowlen, de borrels en etentjes.

Graag wil ik alle collega's uit de capaciteits groep transport in permeabele media en de groep biomedische NMR van de faculteit BMT bedanken voor de samenwerking. De samenwerking tussen twee groepen van verschillende faculteiten blijft toch een dynamisch geheel. In het bijzonder wil ik Roland Valckenborg (wederom collega), Bart Erich (De onbesuisdheid tot kunst verheven), Jelena Petkovic (Het uitdelen van eten zoals watermeloen), Hein Castelijns (Iedere keer weer boeken voor me halen in Delft), Jaap Feijen (Op nieuwjaarsdag samen op een verlaten TU metingen doen), Marcel Lamers (Het beste computernetwerk van het gebouw) en Geralda van Tilborg (koken op Idols night) en Ria Groenendijk (De eindeloze hoeveelheid snoepjes) bedanken. Mijn stagiaires en afstudeerders wil ik ook bedanken voor hun bijdrage: Bart Erich, Roland Meerman, Rodolf Herfst, Bart Beulen and Han Lambriks. Jef Noijen wil ik bedanken voor al zijn inspanningen door de jaren heen en bemoedigende woorden op die momenten dat alles anders ging dan geplanned. Een bijzonder woord van dank past voor Hans Dalderop, die wanneer dat nodig was zijn vakantie verzette om werk voor mij te doen, en altijd zeer nauwkeurig te werk ging in de diverse experimenten die wij op prettige wijze samen hebben gedaan. Mijn kamergenoten wil ik bedanken voor de gezellige sfeer op de kamer: Anneriet Heemskerk (mij 's-avonds in beton gegoten dingen uit de NMR laten halen), Carola van Pul (Samen afwassen = samen zingen), Henk de Feyter (en Vitamina), en Ward Jennekens (de man zonder bijnaam) dank jullie wel.

I also wish to thank Andrew Putnis for acting as my second promotor and the useful discussions we had about my thesis. Ook wil ik de andere leden van mijn lezerscommissie, Rini van Dongen en Herman Beijerinck, bedanken voor de discussie en interessante opmerkingen over mijn proefschrift.

Henk Huinink, bedankt voor je constructieve commentaren en suggesties bij mijn werk. Vooral alle Jiskefet types die langs kwamen bij het bespreken van mijn werk zullen me zeker bijblijven. Leo Pel, bedankt voor je begeleiding, ideeën en opbouwende kritiek. Ik hoop je snel te zien op de house-warming party in je nieuwe huis. Klaas Kopinga, bedankt voor alle lol die we samen hebben gehad (phenomena), en de begeleiding door de jaren heen, dat de lucht boven mijn huis maar rustig mag blijven.

En voor alle steun door de jaren heen wil ik mijn familie bedanken, in het bijzonder Chris voor onder andere het vertalen van het artikel van Lavalley, Bert voor de leuke computer klusjes die als goede afleiding dienden, Andy en Ben voor de eeuwige steun en het brengen van genoeg cola om te overleven, Lies voor alle keren dat je me aan het lachen maakt om jouw acties en het idee om de idols-dvd te kopen. En als laatste Veronique, die het dag en nacht met mij heeft uitgehouden, en steeds een steun en toeverlaat was en is.